Deployment Dynamics of Thin-Shell Space Structures

Thesis by
Antonio Pedivellano

In Partial Fulfillment of the Requirements for the
Degree of
Doctor of Philosophy

CALIFORNIA INSTITUTE OF TECHNOLOGY
Pasadena, California

2021
Defended May 28, 2021

Antonio Pedivellano
ORCID: 0000-0003-2321-7301

ACKNOWLEDGEMENTS

These years at Caltech have been an incredible journey, intense, challenging, but also dense of good memories. If I am here now, it is only thanks to many people who have supported me throughout these years.

First and foremost, I would like to thank my advisor, Prof. Sergio Pellegrino, for believing in me in the first place, and offering me the opportunity to prove myself through this Ph.D. program. He has guided me along the tortuous path of my research and supported me through countless challenges and failures. When I look back at the first year after joining his research group, I remember him trying to contain my eagerness to quickly solve problems and move to the next one. A few years later, he was instead trying to save me from the perfectionist fallacy, as my work was never good enough to me. His example and teachings have contributed to shaping the way I am now, and made me a better researcher and a better person.

I would also like to thank Prof. Ivano Benedetti, my former advisor at University of Palermo. His enthusiasm and passion for research inspired me and encouraged my innate desire to always learn more. I would not have applied for a Ph.D. if it were not for him.

I would like to thank my candidacy and defense committee: Prof. Guruswami Ravichandran, Prof. Chiara Daraio, Prof. Nadia Lapusta, and Prof. Daniel Meiron, for their useful feedback on my research.

I am thankful for the financial support from the Space Solar Power Project at Caltech, which has made my research possible. I would like to thank the entire GALCIT community for making me feel at home during these years, in particular Christine Ramirez, Kate Jackson, Peggy Blue, Jamie Meighen-Sei, Petros Arakelian, and Ali Kiani. My gratitude goes to Prof. Meiron for helping me navigate through the requirements of the Ph.D. program, and Prof. McKeon and Prof. Chung for offering me the opportunity to defend my thesis during the GALCIT Colloquium.

I am also grateful to the International Student Program, in particular Laura Flower Kim and Daniel Yoder, for making it so simple to navigate the intricate US immigration system.

I would like to thank the present and past members of the Space Structure Lab, who have been like a second family to me during these years and from whom I have

learned a lot: Brayden Aller, Dr. Manan Arya, Dr. Miguel Bessa, Dr. Federico Bosi, Gianfranco Canales, Dr. Luke Chen, Sahangi Dassanayake, Dr. Melanie Delapierre, Charles Dorn, Dr. Serena Ferraro, Dr. Terry Gdoutos, Daniele Ghedalia, Dr. Armanj Hasanyan, Dr. Wilfried Jahn, Wolfgang Klimm, Dr. Christophe Leclerc, Dr. Andrew Lee, Dr. Wen Luo, Michael Marshall, Harsha Reddy, John Pederson, Dr. Fabien Royer, Dr. Maria Sakovsky, Charles Sommer, Dr. Thibaud Talon, Alan Truong, Dr. Daniel Türk, Kanthasamy Ubamanyu, Dr. Yuchen Wei, Alexander Wen, and Dr. Lee Wilson. Special thanks go to the DOLCE team, with whom I have shared successes and failures in the development of the most ambitious project I have ever been part of. They developed the deployable structures described in this thesis, and gave me the unique opportunity to do research on a system whose complexity requires so much expertise, time, and resources to make it out of reach for any individual researcher.

I also want to thank my colleagues during the first year in Galcit, and the friends I made during my time in California, with whom I have shared many good times.

I will always be grateful to my family, who has always believed in me and has sacrificed a lot to give me the opportunity to chase my dreams. To my mother, Antonella, who has always encouraged me to strive for the best; to my father, Rosario, who has taught me the value of hard work; and to my brother, Emanuele, who has always been close to me, despite the distance. I also want to thank my acquired family, Enzo, Angela, Erika, and Benny, for supporting me through my choices, despite the emotional toll they took on them.

Last, but not least, I want to thank my better half, Noemi, for having always been by my side in this incredible journey. She would have never guessed that "following me to the ends of the Earth" would have had such a literal meaning to her. I know how difficult it was for her to change her life and follow me to the US, and I can only imagine how difficult it is to be married to a Ph.D. student. Nevertheless, she has always supported me, sharing my accomplishments and my disappointments (which were far more frequent). She is the muse who inspires me and gives meaning to my world, and I am very lucky to share my life with her.

ABSTRACT

Thin-shell structures provide a lightweight solution for deployable structure applications. Despite being only few tens of microns thick, these structures provide excellent bending stiffness, thanks to their curved cross-section. Their thinness also allows them to be elastically packaged into small volumes to fit into a launch vehicle; once in space, they can be self-deployed by releasing their stored elastic energy.

Most space applications use thin-shell structures to deploy and tension thin membranes, such as solar sails, drag sails, and solar arrays. Recently, a novel space solar power architecture has been developed at Caltech, and it relies on distributed thin-shell components, connected in a space frame, to create large-area deployable structures. Thanks to the unique properties of thin shells, these structure provide superior stiffness-to-mass ratio and self-deployment capabilities. However, to demonstrate their reliability and enable their use on space missions, their deployment dynamics must be understood and predicted.

Ground testing is the established approach to verify a structure throughout its design and qualification process. However, replicating the space environment in a laboratory setting is generally not possible, especially for lightweight structures, which are very sensitive to the effects of gravity and air. Numerical models are therefore the only tool to predict the behavior of a structure in space. However, validation with ground experiments is necessary to build confidence in the models, which must be able to capture the complexity of the interaction with air, gravity, and the suspension system that supports the weight of the structure.

The goal of this thesis is to develop high-fidelity models for large space structures, where multiple thin-shell components are folded together and deploy by releasing their strain energy. This overall objective is achieved in 3 steps. First, a ladder-type rectangular strip is introduced, as a building block for more complex architectures. The strip is composed by two thin-shell longerons, symmetrically folded at two locations. The deployment dynamics of this structure is investigated through experiments on 1 m-scale prototypes, both in air and in vacuum. A detailed analysis of its elastic folds is performed using full-field displacement measurements from Digital Image Correlation. A finite element model of this strip is presented, and it is shown to accurately capture the dynamics of the strip for all tested conditions. Then, the implementation of the packaging and deployment scheme of a space solar

power spacecraft, composed of multiple strips, is discussed. A kinematic model of the structure is proposed as a design tool to achieve systematic folding. A novel concept of a deployment mechanism to coil the structure in a robust and reliable way is proposed. Also, a staged deployment scheme is demonstrated, to reduce the uncertainty of strain-energy deployment for large space structures. Finally, the deployment dynamics of a 2 m-scale space structural prototype, based on the space solar power architecture, is investigated. A full-scale finite element model of the structure is implemented to replicate its complex folding scheme and capture the deployment process, including the interaction with the deployment mechanism and the suspension system. The simulations predict well the behavior of the structure observed in experiments through motion capture techniques.

The work presented in this thesis advances previous studies on the deployment dynamics of simple thin-shell components, and demonstrates that even complex thin-shell architectures can be packaged and deployed in a controlled and predictable way. The solutions proposed in this thesis have guided the packaging process and the design of the deployment mechanism for DOLCE, an upcoming flight demonstration of the space solar power architecture described in this work. However, this research has much broader implications, as the experimental and numerical framework presented herein can be generalized to different shell-based architectures, and contributes to enabling a new generation of lightweight deployable structures for future space applications.

PUBLISHED CONTENT AND CONTRIBUTIONS

[1] Antonio Pedivellano and Sergio Pellegrino (Manuscript submitted for publication). "Deployment Dynamics of Thin Shell Space Structures". In: *Journal of Spacecraft and Rockets*.

A.P. designed the experimental setup, characterized the strip geometry and stiffness, performed the deployment experiments, implemented the finite element model, and wrote the manuscript.

[2] Antonio Pedivellano and Sergio Pellegrino (2021). "Deployment Dynamics of Foldable Thin Shell Space Structures". In: *AIAA Scitech 2021 Forum*. 2021-0299. DOI: 10.2514/6.2021-0299.

A.P. designed the experimental setup, characterized the strip geometry and stiffness, performed the deployment experiments, implemented the finite element model, and wrote the manuscript.

[3] Eleftherios Gdoutos, Alan Truong, Antonio Pedivellano, Fabien Royer, and Sergio Pellegrino (2020). "Ultralight deployable space structure prototype". In: *AIAA Scitech 2020 Forum*. 2020-0692. DOI: 10.2514/6.2020-0692.

A.P. designed and built the deployment mechanism prototype, designed the deployment sequence of the structure, participated in the deployment experiments and in the writing of the manuscript.

[4] Antonio Pedivellano, Eleftherios Gdoutos, and Sergio Pellegrino (2020). "Sequentially controlled dynamic deployment of ultra-thin shell structures". In: *AIAA Scitech 2020 Forum*. 2020-0690. DOI: 10.2514/6.2020-0690.

A.P. implemented the kinematic model of deployment, designed the deployment sequence of the structure, implemented the finite element model, participated in the deployment experiments, and wrote the manuscript.

[5] Sergio Pellegrino, Eleftherios E Gdoutos, and Antonio Pedivellano (Apr. 2020). *Actively Controlled Spacecraft Deployment Mechanism*. US Patent App. 16/670,941.

A.P. contributed to the idea of pressure stabilization, proposed the force-control scheme, designed and built the first deployment mechanism prototype.

TABLE OF CONTENTS

LIST OF ILLUSTRATIONS

LIST OF TABLES

Chapter 1

INTRODUCTION

1.1 Motivation

In recent years, the space industry has experienced a rapid growth, driven by the reduced cost of launches and by the development of small satellites, e.g. CubeSats, which have offered low-cost access to space. While economic factors push towards smaller and lighter spacecraft, system performances often scale with the operational size of the system.

Deployable structures address these conflicting requirements, as they can be packaged into tight volumes before launch, and expanded into their large operational shape once in space. These features make them ideal for solar arrays, antennas, and space telescopes. In more recent applications, deployable structures have also been used for solar propulsion, deorbiting systems, and deployable booms.

The majority of deployable structures flown to space and commercially available today consists of mechanical articulations of rigid components, supporting lightweight surfaces. Notable examples include space antennas, most of which are based on a mesh reflector architecture, where a rigid truss structure pretensions a network of thin cables, supporting a reflective metallic mesh. Fig. 1.1a shows an AstroMesh antenna, supported by a perimeter truss structure; Fig. 1.1b is an example of a radial rib antenna, where the mesh is supported by an umbrella-like rigid mechanism. In the case of solar arrays, the solar cells are typically supported by rigid panels connected by hinges, packaged either by folding them in an accordion style (see Fig. 1.1d) or using a fan-folding scheme (see Fig. 1.1c).

However, in the last decade, thin-shell structures have become increasingly popular, as they provide higher stiffness-to-mass ratios, higher packaging efficiency, and simpler actuation, compared to more conventional deployable structure architectures. Thin-shell structures owe their superior performances to their curved cross-sections, which provide high moments of inertia (hence high bending stiffness), despite their walls often being only few tens of microns thick. The shape of their cross-section allows them to be elastically collapsed, so that they can be stowed in a compact volume either by folding them multiple times [67], or by rolling them in a cylindrical configuration [10]. Additionally, thin-shell structures can self-deploy by releasing

their strain energy once in space, greatly simplifying the deployment mechanisms that support them during launch.

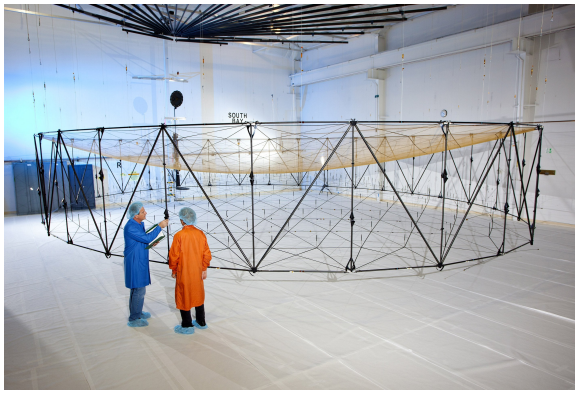

(a) AstroMesh (Credit: Northrop Grumman)

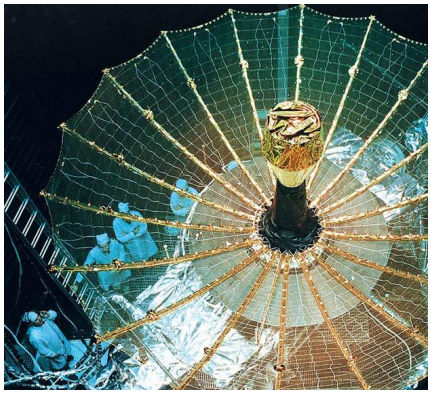

(b) Folded Rib Reflector [2] (Credit: L3Harris)

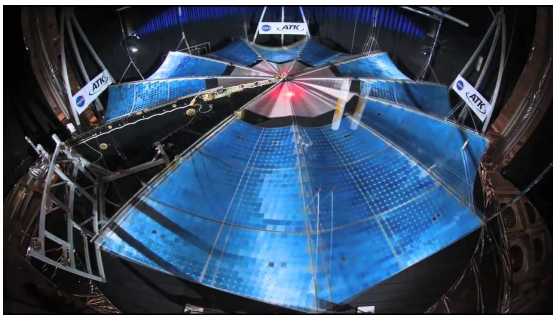

(c) MegaFlex solar array [77]

(d) Solar array of the Juno spacecraft (Credit: NASA)

Figure 1.1: Examples of deployable antennas and solar arrays based on mechanical articulations of rigid structural elements.

Despite their evident advantages, widespread application of these structures has been limited so far by their nonlinear mechanical behavior, characterized by structural instabilities [43][39][57] and localized deformations [90], as well as by their complex deployment dynamics [107]. For these reasons, thin-shell structures have been mostly used in space as deployable booms [42], monopole antennas [67], and support structures to pretension thin films in solar sails [45][8], drag sails [96], and solar arrays [38]. Fig. 1.2a shows a foldable antenna design, used aboard the Mars Express and Mars Reconnaissance Orbiter spacecrafts, and passively deployed under its own strain energy. Fig. 1.2b is an example of a deployable boom consisting of 2 Ω-shaped half-shells, coiled around a cylindrical hub [10].

Coilable booms are particularly suited for tensioned architectures, in which the tip of the boom is attached to the ends of a thin membrane, which is deployed and

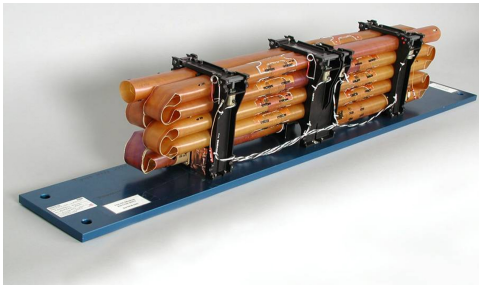

(a) SHARAD foldable antenna for the Mars Reconnaissance Orbiter spacecraft (Credit: Northrop Grumman)

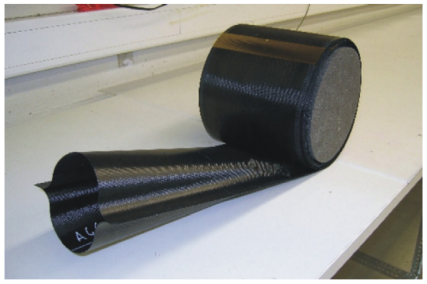

(b) Coilable boom for solar sail applications (DLR) [10]

Figure 1.2: Examples of deployable booms.

tensioned by the boom. Fig. 1.3a is an example of a solar sail based on this concept, in which 4 deployable booms connect to the ends of a square membrane. Another remarkable example is the Roll-Out Solar Array (ROSA) [38], shown in Fig. 1.3b, consisting of two deployable booms supporting a flexible blanket, which contains solar cells. The structure is packaged by rolling it in a cylindrical shape, and can be passively deployed in space under its own strain energy. After its successful demonstration in 2018, this roll-out architecture is going to be used in 2021 for the new solar arrays that will be integrated on the International Space Station [26].

While these concepts use deployable booms as compression elements, novel architectures have been proposed to exploit their bending stiffness to create large-area structures that maintain their deployed shape without external preloading. This can be achieved by distributing many thin-shell longerons over the structure, interconnected in a space frame and acting as a bending-stiff skeleton to support flexible membranes. This concept was first proposed for the space solar power architecture [4] developed at Caltech (see Fig. 1.4). It envisions a constellation of large planar spacecraft (up to 60 m $\times$ 60 m in size) consisting of an assembly of strips, each composed by two thin-shell longerons to provide bending stiffness, and a thin membrane supporting multiple functional units, called "tiles" [50][28], which combine photovoltaics and antennas.

In general, space frames require a combination of coiling and folding techniques to achieve efficient packaging. While the problem of co-coiling multiple shells has received much attention and is better understood, folding and deploying a thin-shell space frame remains an open problem.

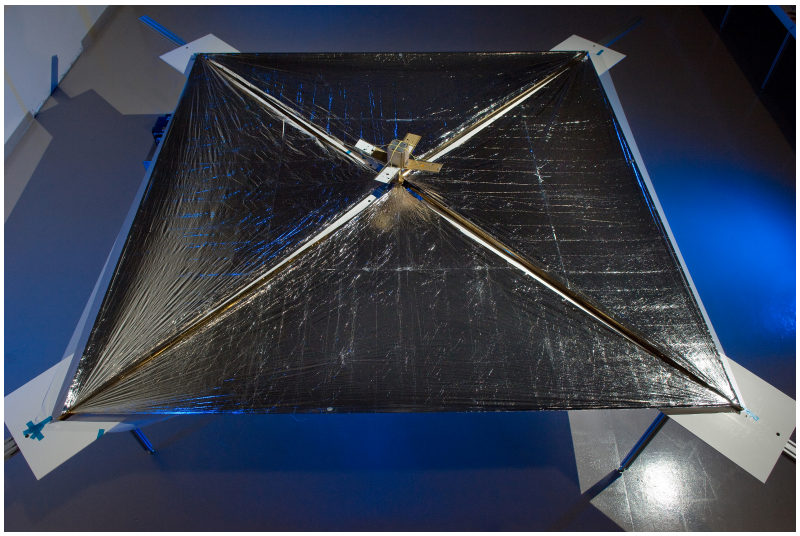

(a) NanoSail-D solar sail demonstrator (Credit: NASA)

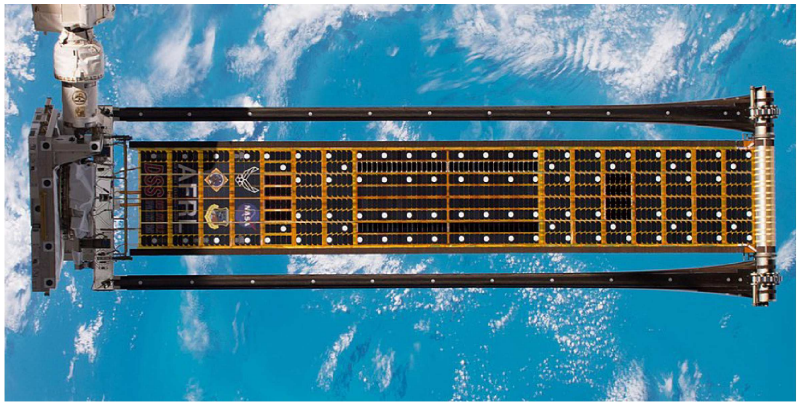

(b) Roll-Out Solar Array (ROSA) demonstrator (Credit: NASA)

Figure 1.3: Applications of deployable booms to tension a thin membrane.

1.2 Challenges of Self-Deployable Thin-Shell Structures

One of the main challenges is to predict the evolution of the structure during deployment in space. In these regards, ground testing is an invaluable tool to understand the behavior of the structure from its early stages of development. However, the behavior observed in a laboratory setting can be quite different from what it would be in space [22][111], due to spurious effects, such as gravity and air. These effects are particularly significant for structures with large area-to-mass ratios deploying dynamically, and need to be carefully quantified.

In terms of experimental techniques, optical methods are the state-of-the-art for rigid deployable structures. In the simplest case, a single camera with its sensor plane oriented parallel to the deployment plane can be used to record the deployment and

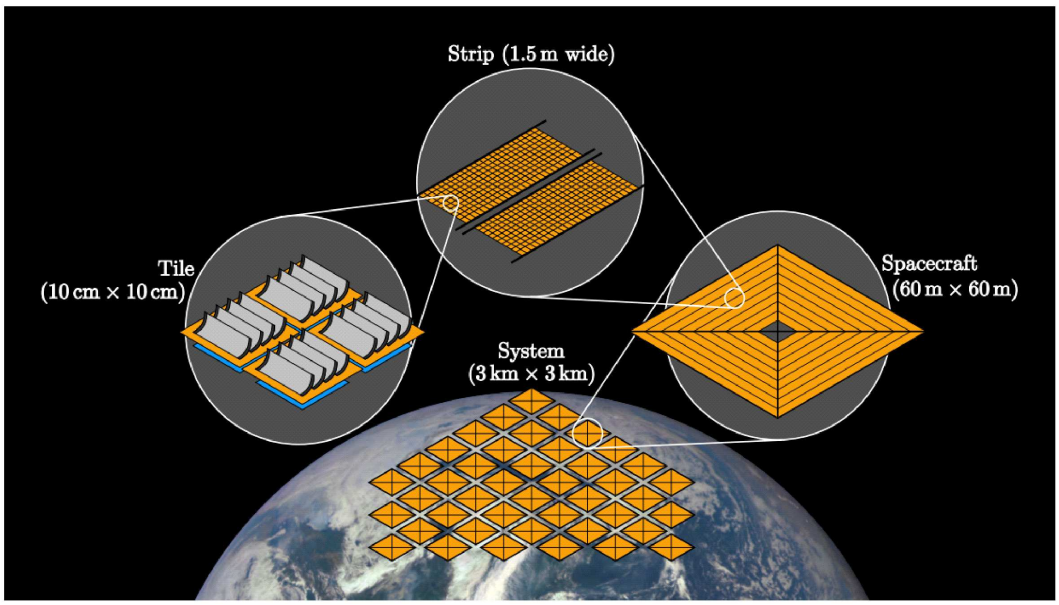

Figure 1.4: Concept of a space solar power system developed at Caltech.

track the 2D coordinates of discrete points [66], or to measure the angle between rigid portions of the structure [63]. For 3D motion, photogrammetry is one of the most common techniques: it uses two or more cameras oriented at different angles to take synchronized images of the same subject, identify the location of discrete markers on each camera sensor, and triangulate them to find the 3D coordinates of the points [48][78]. Similarly, motion capture systems use infrared scanners to swipe their field of view, estimate the distance from retroflective markers by measuring the time for light to be reflected back at the camera sensor, and triangulate the distance from multiple cameras to obtain the 3D coordinates of the markers [15]. However, reconstructing the shape of a structure from a few discrete points is possible only if the geometry of the structure is known in advance (e.g. the distance of the markers from the hinge axis). For a folded thin-shell structure, the axes of its elastic folds are not fixed, and their locations needs to be measured during deployment. Therefore, more detailed measurements are required, either by tracking a large number of points, or by switching to full-field measurement techniques, such as Digital Image Correlation.

In addition to experimental tests, numerical models are often developed to assist the design of a structure and predict its performances in space. This is particularly important for large structures, for which full-scale ground tests might not be possible, as in the case of the 20-m-long MARSIS antennas [73]. For rigid structures, multi-body dynamics approaches often provide accurate solutions with reasonable

computational cost [111][55]. On the other hand, thin-shell structures generally require higher fidelity models, mostly based on the finite element method, to capture their nonlinear mechanical behavior [63]. In some cases, combinations of both approaches have been used, where a high fidelity model of a subset of a structure informed a lower fidelity simulation of the full structure. This method is particularly useful when rigid parts are connected by elastic joints [24]. However, developing a thin-shell space frame requires a high fidelity model of the entire structure, capable of capturing the complex interactions and contacts between multiple thin-shell components, which has never been attempted yet.

Another challenge associated with foldable thin-shell space frames is achieving reliable deployment. During strain energy deployment, a structure spontaneously follows its minimum energy path, eliminating the need for external actuation and dramatically simplifying its deployment mechanism. However, as the size and complexity of the deployable structure increase, multiple energetically-similar deployment paths can exist, resulting in a non-unique deployment process. Even worse, it is possible that some of these alternative deployment paths possess local energy minima, where the structure could achieve static equilibrium without ever reaching its fully deployed configuration.

1.3 Research Objectives

The main objective of this thesis is to extend the use of thin-shell deployable structures to large area applications, by enabling a new generation of self-deployable shell-based space frames. In particular, this study focuses on the deployment dynamics of initially folded structures, targeting the following goals:

1. **Investigate the dynamics of space frames composed of multiple thin-shell components, folded at multiple locations.**

   Current experimental techniques assume that the geometry of the structure is known in advance, specifically in regards to the location of the hinges for rigid structures. As elastic folds in thin-shell components can potentially propagate, their location needs to be identified and tracked during deployment. Established experimental methods can be used to develop a framework to gather data with high spatial and time resolution, and to extract the full evolution of the elastic folds. Using this tool, the behavior of foldable space frames can be investigated, shedding light on the effects of various design parameters, such as boundary conditions and the presence of a thin functional

layer on the structure, as well as external disturbances, in particular regarding air.

2. **Predict the dynamics of deployment using finite element models.**

   Deployment simulations of thin-shell space frames pose unique challenges, as structural instabilities, complex contact conditions, and constraints between multiple shells need to be accurately captured. Achieving the correct packaged shape before initiating the deployment simulation is essential. For complex structures, the packaging scheme intended for physical prototypes might not be practical to replicate in simulations. Therefore, identifying compatible kinematic paths for the structure is required in order to devise *ad hoc* packaging sequences for the numerical model, resulting in the correct packaged state. Furthermore, to build trust in the model, it needs to be validated against ground experiments, which requires correct accounting of the effects of gravity and air on the deployment of the structure.

3. **Design solutions to stow space frames in a predictable and controlled way.**

   Packaging a large space frame requires bi-axial compaction, using folding and coiling techniques. The kinematics of this process is often not trivial, and the elastic nature of the thin-shell components oppose the applied deformations. This can result in unstable or uncontrolled behavior of the structure, with consequent risk of structural damage. For foldable shells, imposing elastic folds at chosen locations can lead to a more deterministic behavior. Kinematic models can guide this process, as they can identify internal mechanisms of the structure that require minimal elastic deformations. To prevent instabilities in coiled shells, a deployment mechanism is generally needed. Its role is to apply external constraints to the structure, making it conform to the geometry of the hub. While mechanisms exist for standalone deployable booms, thin-shell space frames introduce additional complexity, as their various parts must be simultaneously coiled about different hubs. Synchronization becomes essential, and robust control schemes for the mechanism are required.

4. **Improve the deployment reliability of large space frames.**

   During strain energy deployment, a structure follows its lowest energy path. However, large structures made of numerous thin-shell components might have multiple energetically-equivalent deployment paths, resulting in a non-unique deployment process. Some of these paths might present local minima,

where the structure could achieve static equilibrium without ever reaching its fully deployed state. To mitigate the risk of incomplete deployment, a staged deployment scheme can be implemented, potentially increasing the reliability of the deployment, by introducing a small number of additional actuators.

1.4 Layout of the Thesis

The research presented in this thesis focuses on a specific structural architecture, i.e. the space solar power satellite described in Sec. 1. A rectangular strip is studied first, as a building block for the larger structure and a benchmark problem to validate the numerical model. Then, a 2-m-scale implementation of the space solar power architecture is presented, and its packaging and deployment are studied in detail.

The thesis is organized as follows. Chapter II discusses the deployment dynamics of a rectangular strip composed of 2 thin-shell longerons. The design and characterization of an experimental setup to compensate gravity effects are discussed. High-speed imaging and Digital Image Correlation are used to follow the structure during its deployment, and an algorithm to reconstruct the shape of the strip and track the evolution of the elastic folds is presented. The interaction of the structure with air is documented by comparing experiments performed in air and in vacuum. Then, a finite element model of the structure is presented, and an approach to accurately model the suspension system and the interaction with air is proposed. The model is validated by comparison with experiments.

Chapter III focuses on the implementation of a kirigami-inspired packaging scheme for a thin-shell space structure composed of multiple thin-shell strips. Three main topics are covered in the chapter, corresponding to the three phases of stowage and deployment: folding, coiling/uncoiling, and unfolding. First, a method to fold the structure in a predictable and controlled way is proposed, based on the idea of imposing elastic folds at opportune locations to create fixed elastic hinges, resulting in a more deterministic kinematics. A kinematic model of the structure is implemented to identify compatible kinematic paths and design the folding procedure. Then, a novel deployment mechanism concept to achieve robust coiling and uncoiling of the structure is presented, and its implementation is discussed. Finally, a staged deployment scheme is proposed as a way to mitigate the uncertainty of strain-energy deployment of interconnected thin-shell components. The concepts in this chapter are demonstrated on a 2-m-scale structural prototype, and scalability to larger structures is discussed.

Chapter IV studies the deployment dynamics of a square space frame, composed of 12 deployable strips. In this case, a single-stage deployment is performed, although the techniques used here could be readily applied to multi-stage deployment schemes. A motion capture system is used to track the location of multiple retroflective targets on the structure, and the envelope of the structure, as well as its deployed size over time, are presented. The angle of the elastic folds on the outermost strips is also reconstructed by a dedicated algorithm. An approach to folding and deployment simulations with finite elements is also presented, and the results are compared with experiments. Simulations are then used to investigate the evolution of the elastic folds during dynamic deployment.

Chapter V concludes the thesis and discusses directions for future research.

Chapter 2

DEPLOYMENT DYNAMICS OF THIN-SHELL STRIPS WITH ELASTIC FOLDS

Parts of this chapter were modified from the following publications:

[1] Antonio Pedivellano and Sergio Pellegrino (2021). "Deployment Dynamics of Foldable Thin Shell Space Structures". In: *AIAA Scitech 2021 Forum*. 2021-0299.

[2] Antonio Pedivellano and Sergio Pellegrino (Manuscript submitted for publication). "Deployment Dynamics of Thin-Shell Space Structures". In: *Journal of Spacecraft and Rockets*.

2.1 Introduction

Many deployable structures for space applications forming large planar surfaces consist of rigid panels connected by hinges. Packaging involves folding the panels around hinges, and deployment can be driven either by external mechanisms [101, 47] or by releasing the strain energy stored in elastic hinges [55, 44, 88]. Two folding concepts are shown in Fig. 2.1. Z-folding consists of alternating mountain and valley folds in an accordion-like fashion, and has been used in many structures, including the 34 m $\times$ 12 m solar arrays of the International Space Station [107]. Tri-folding consists of folding the panels in the same direction; typically, there is a central panel on top of which two side panels are folded, hence the name. This folding method has been used in CubeSats, e.g. MarCO [51] and OMERA [88], where the solar panels are initially folded parallel to the faces of the bus, or in combination with z-folding, such as in the Folded Integrated Thin Film Stiffener (FITS) array, for the TacSat-2 mission [36].

Recent advances in solar cells, e.g. perovskite cells [109], and flexible electronics [35] offer the opportunity to develop new structures for solar arrays and antennas with reduced mechanical complexity, mass, packaged volume and, ultimately, cost. A well-established approach uses thin-shell deployable booms to deploy solar array blankets or multifunctional membranes. The Roll-Out Solar Array (ROSA) flight test [93] has demonstrated a flexible blanket containing solar cells and supported by two thin-shell composite slit tubes. This 5.4 m $\times$ 1.7 m array was initially coiled on a cylindrical mandrel, and then self-deployed by the controlled release of elastic

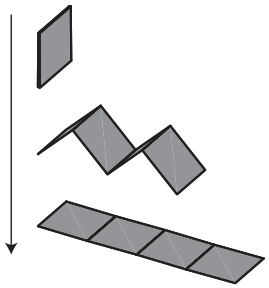

(a) Z-folding (accordion-type folding) of a solar array [78] [70]

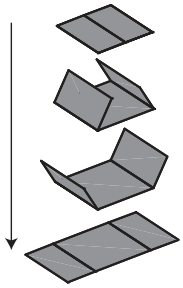

(b) "Tri-fold" packaging concept [48]

Figure 2.1: Packaging concepts for foldable strip architectures with rigid panels.

strain energy in the deployable booms. Another example is the recent technology demonstration OrigamiSat-1, in which a 1 m $\times$ m membrane deployed by four diagonal open section carbon fiber reinforced plastic (CFRP) thin-shell booms [42] was partially covered with copper indium gallium selenide (CIGS) cells and shape memory alloy antennas. In these examples, the booms are coiled with a deployment mechanism that supports them and constrains their deployment.

An alternative approach was introduced in the Caltech Space Solar Power Project spacecraft architecture [4], which considers large deployable structures consisting of multiple strips and which are packaged through a combination of folding and coiling. The present study is motivated by the desire to develop accurate simulation models for the deployment dynamics of these future deployable structures which include several thin-shell components that are folded together and spring open upon release.

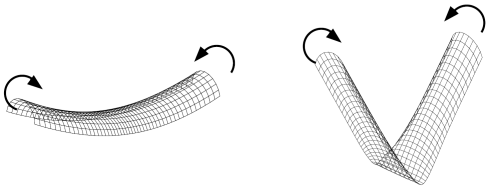

(a) Localized folds in a tape spring (image adapted from [90])

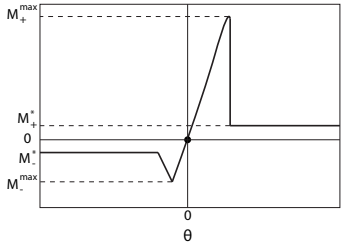

(b) Schematic moment-rotation relationship for a tape spring

Figure 2.2: Non-linear mechanical response of a tape spring under bending. After the initial linear behavior, a snap-through instability leads to the formation of localized folds.

The problem of folding and deploying thin-shell structures has been extensively studied in the past for tape springs, i.e. cylindrical shells with a circular arc cross section. Under applied bending moments, these structures exhibit a non-linear mechanical response and undergo snap-through instabilities, resulting in the formation of localized elastic folds. Figure 2.2a shows two geometric configurations of a tape spring. For small applied rotations, the tape spring deforms uniformly. At the buckling limit, the cross section of the tape spring flattens in a small region, creating an elastic fold. Figure 2.2b shows a notional moment-rotation relationship for a tape spring: after an initially linear response, the bending moment drops and becomes mostly independent of the applied rotation. The first documented study of the geometry of elastic folds dates back to the 1920s [11], although models to predict the moment-rotation relationship were not developed until the 1950s [108]. They were later expanded by Rimrott [82] and Mansfield [64]. Seffen and Pellegrino [90] investigated the dynamics of initially folded tape springs during strain energy-driven deployment. Their study showed that elastic folds propagate along the axis of the shell, resulting in a complex but predictable deployment behavior.

More recently, the dynamic deployment of foldable tubular shells with longitudinal cutouts that create elastic hinges at some specific locations has been studied [63], after the successful implementation of this concept in the 20-m-long antennas on board the MARSIS spacecraft [67].

All of this previous research has focused on a single thin-shell structure, either with a single elastic fold or with multiple folds whose propagation is prevented by the geometry of the shell (as in the case of foldable tubes). Further developments of foldable strip architectures will involve the deployment of shell structures in which multiple shells are folded together, which is the focus of the present thesis.

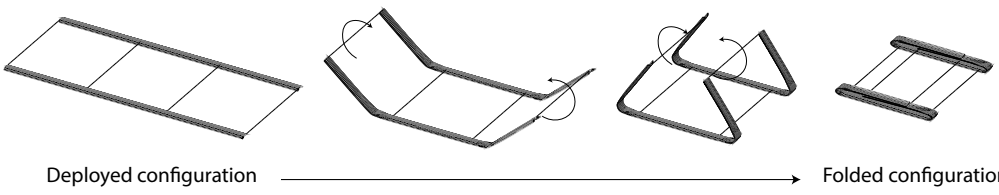

Figure 2.3: Concept of foldable strip with tape spring longerons.

The experimental part of the study involved the design and construction of high-quality test articles, as well as the development of a suspension system with low inertia and friction, and robust against changes of the strip geometry that might occur

due to propagation of the elastic folds. 3D Digital Image Correlation (DIC) was used to characterize the deployment with high-speed cameras, and an algorithm to identify the elastic folds and track their propagation from DIC images was developed. The influence of air on the dynamic deployment of the strips was investigated by performing deployment experiments both in air and in vacuum. The effects of a thin film attached to the longerons and representing, for example, the photovoltaic cells and the electric substrate of a solar array, was also studied.

The computational part of the study used a high-fidelity finite element model of the strip to capture the elastic deformation and localization that occur during the initial folding of the strip, the self-contact between different parts of the structure as the folding develops, and the strain energy stored during the folding process. It also captured the deployment dynamics and self-latching of the structure, and the effects of air on the deployment process. This part of the study builds on previous studies of the folding and deployment of tape springs [90] and tubular thin shells with longitudinal cutouts [63].

The chapter is organized as follows. Section II describes the geometry of the strips and the suspension system. Section III discusses the implementation and characterization of the experimental setup. Section IV presents the experimental results, and addresses the effect of attaching a thin film on the strip deployment, as well as the influence of air during deployment. Section V describes the finite element model of the strip, discussing the simulation technique and the simulation parameters. Section VI presents the results from the simulations and compares them with the experiments. In Section VII, the effect of the initial and boundary conditions of the structure on its deployment dynamics is investigated through experiments. Finally, Section VIII discusses the results and concludes the chapter.

2.2 Description of Test Configuration

The basic architecture of the strip was derived from the Caltech Space Solar Power Project that has been described in previous publications [4, 85]. In the present study, the overall shape of the strip was simplified to a rectangle, to create a plane of symmetry that would allow a more symmetric deployment.

2.2.1 Strip Design

Figure 2.4 shows a strip consisting of two thin-shell longitudinal elements, herein called "longerons," which provide bending stiffness to the deployed strip, and can be folded by forming elastic folds. They have an open cross section consisting

of two circular arc flanges, connected by a flat web. This cross section design, first introduced in the Triangular Rollable And Collapsible (TRAC) booms [83] is symmetric with respect to the axis of bending of the strip, and hence the moment-rotation relationship is independent of the sign of the moment. The longerons are connected by transverse rods, called "battens," which have a rectangular cross section and are responsible for the bending stiffness of the strip in the transverse direction, as well as for coupling the deformation of the longerons. The structure formed by the longerons and battens supports a thin film that in an actual application would support functional elements, such as solar cells or RF antennas. The strip is terminated by two rigid connectors mounted in the middle of the outermost battens.

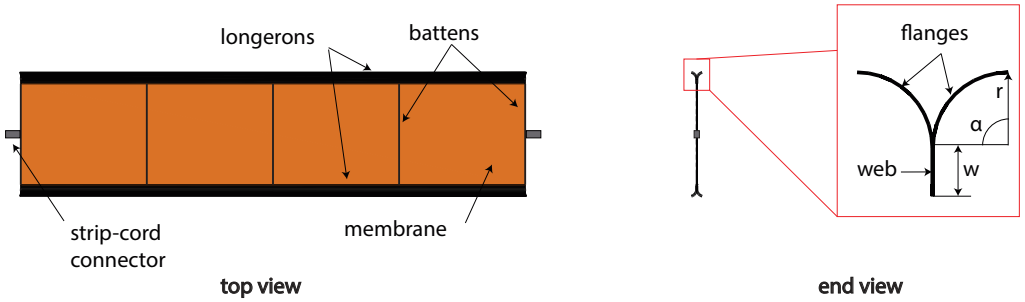

Figure 2.4: Strip geometry: top view (left); side view and detail of TRAC longeron geometry (right).

2.2.2 Suspension System Concept

Testing the deployment of thin-shell deployable structures in the presence of gravity is challenging, due to existence of low stiffness deformation modes in the folded configurations of these structures. Although gravity-related loads are rather small, due to the lightness of these structures, they can have a significant impact on deployment, and in fact many of these structures are unable to fully deploy under gravity unless they are properly supported throughout the deployment process.

Therefore deployment testing of lightweight structures may involve drop towers [59] [94] or parabolic flights [9, 21] to achieve micro-gravity for a few seconds, although in most cases deployable structures are supported for deployment by a suspension system.

Vertical cords can be attached to a fixed point [66], with or without soft springs that allow extension of the cords with minimal variation of their tension (Fig. 2.5a).

Nested fly beams have been used to create a "marionette"-like suspension [33]. For deployment experiments, the cords are generally attached to sliders following the structure, in order to keep the cords vertical at all times (Fig. 2.5b). A drawback of this solution is the inertia and friction of the sliders can significantly affect the deployment [22]. These effects can be avoided using active gravity compensation systems [34], which allow for zero-stiffness rigid body motion, zero friction, and minimal added mass. However, such systems involve significant mechanical complexity and are generally adopted for heavier structures with simpler kinematics.

A passive suspension system was chosen due to its simplicity and the potential for accurately modeling its interaction with the structure during deployment. However, the presence of elastic folds made it challenging to implement a suspension in which deployment occurs in a horizontal plane. Therefore, instead of trying to minimize the effects of gravity on the structure, a simpler suspension system was designed that allows the complete deployment under gravity, while making it possible to accurately estimate the constraint forces applied to the structure.

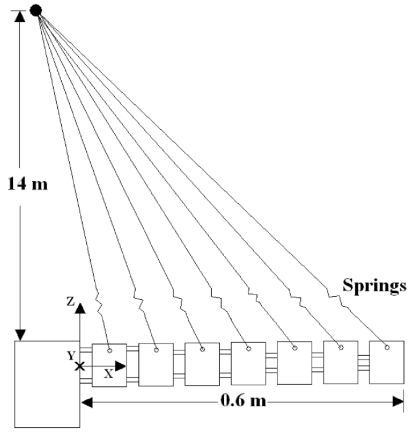

(a) Single-point suspension system for z-folded rigid solar array [78]

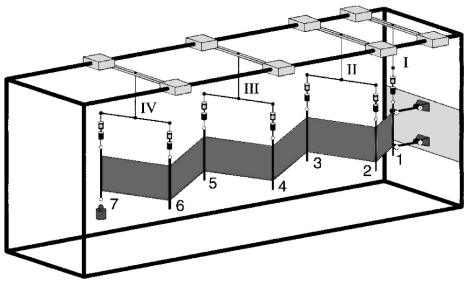

(b) Gravity offloading with sliding flybeams during deployment of a z-folded rigid solar array [22]

Figure 2.5: Examples of passive gravity compensation schemes for ground deployment of folded rigid solar arrays.

Several support schemes were considered, Fig. 2.6. A scheme with sliders, Fig. 2.6a, would simplify the trajectory of the ends of the strip; however, the mass of the sliders would be significant and their friction would be a significant source of uncertainty. Figure 2.6b shows two end cords attached to a single suspension point. Although this solution would add only a small mass to the strip, the resulting in-plane forces would counteract the elastic moments in the elastic folds, likely preventing

the complete deployment of the structure. An alternative solution is to connect each cord to a pulley, and to use masses to apply tension to the cords and compensate for the weight of the strip. This concept can be used to deploy the strip in 2 different orientations, i.e. against gravity, Fig. 2.6c, or assisted by gravity, Fig. 2.6d. Since the latter requires two sets of pulleys, thus increasing inertia and friction, the concept in Fig. 2.6c was chosen. Its implementation is discussed in the next section.

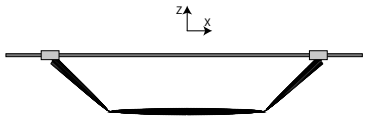

(a) Sliding supports

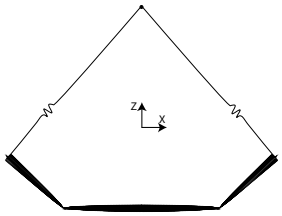

(b) Single-point suspension system with soft springs

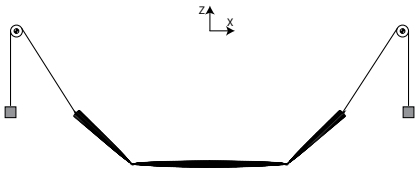

(c) Suspension system with counterweights (upward deployment)

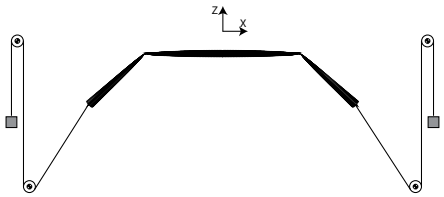

(d) Suspension system with counterweights (downward deployment)

Figure 2.6: Side views of suspension system concepts for ground deployment of foldable flexible strips.

2.2.3 Design of Suspension System

The suspension system and the parameters required to fully define a deployment experiment are shown in Fig. 2.7. Since the present study has focused on 1 m scale strips, the distance L_f = 1300 mm between the pulleys was chosen, to provide enough clearance for the structure during deployment.

When the strip is in the folded configuration the two forces are denoted by R in Fig. 2.7. These constraint forces are provided by a release mechanism that is instantaneously released to initiate deployment.

The folded configuration of the strip is defined by the position and angle of the elastic folds. For initially symmetric configurations of the folded structure, as considered in the present study, the initial geometry is defined by the distance between the folds

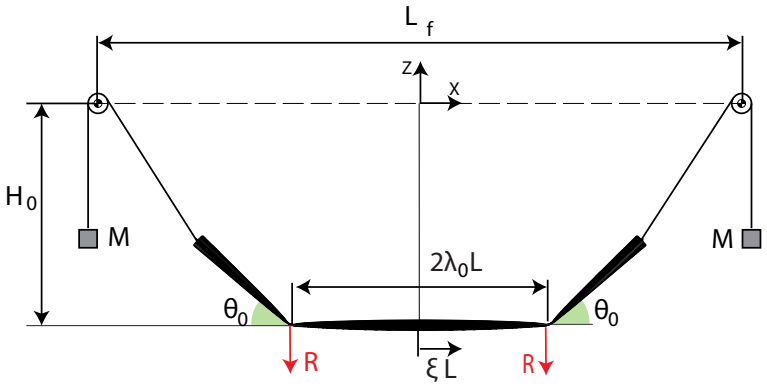

Figure 2.7: Geometry and design parameters of the suspension system developed for the deployment experiments.

$2\lambda_0 L$, with $\lambda_0 \in [0, 1]$ (where $\lambda_0 = 0$ corresponds to a single fold at the center of the strip), and the angle of the folds θ_0. λ_0 was set by the position of the release system, whereas θ_0 was not controlled directly, but it was controlled by the distance H_0 between the center of the strip and the pulleys, as shown in Fig. 2.7, and the mass M of the counterweights attached to the cords.

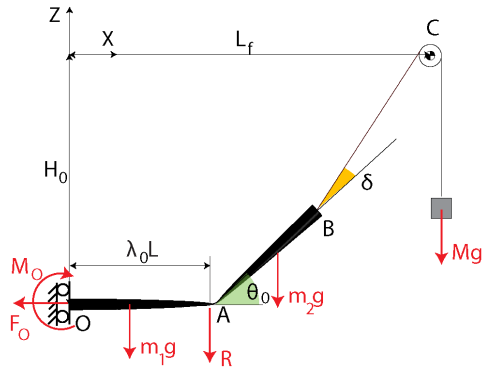

(a) Equilibrium of the strip

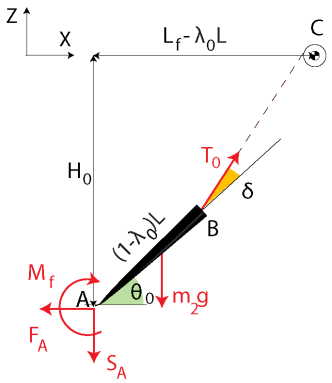

(b) Equilibrium of the region AB (from the fold to the end of the strip)

Figure 2.8: Free body diagram for a strip symmetrically folded. R is the vertical constraint applied by the release mechanism to prevent self-deployment.

The relationship between these parameters is governed by the static equilibrium of the folded strip, described by the free-body diagram in Fig. 2.8. Specifically, the equilibrium of the moments about the axis of the elastic fold for the region AB in Fig. 2.8b can be written as:

$$M_f - T_0(1-\lambda_0)L\sin\delta + m_2 g(1-\lambda_0)^2\frac{L^2}{4} = 0 \tag{2.1}$$

where $T_0 = Mg$ for the equilibrium of the moments for the pulley in C. Here, $m_1 = d\lambda_0 L$ and $m_2 = d(1-\lambda_0)L$ are the mass of each straight portion of the strip, with d representing the mass per unit length. Also, M_f is the steady-state moment of the elastic hinge, which can be estimated from plate theory (its value is also measured experimentally in Sec. 2.3.2). A second equation is required to solve the problem in the two unknowns θ_0 and δ. This is provided by a geometric condition, relating the angles θ_0 and δ with the known height H_0 and the location of the pulley C:

$$\tan(\theta_0 + \delta) = \frac{H_0 - (1-\lambda_0)L\sin\theta_0}{L_f - [\lambda_0 + (1-\lambda_0)\cos\theta_0]L} \tag{2.2}$$

Eqns. 2.1 and 2.2 represent a system of non-linear equations that can be solved numerically for given M, H_0, λ_0, and known geometry and stiffness of the strip. While, in principle, the choice of H_0 can be arbitrary, a lower bound to the mass of the counterweights exists, to guarantee that the suspension system can support the self-weight of the strip during deployment. This condition is met when the release mechanism applies a downward reaction R to maintain the strip in its folded state, i.e. $R \geq 0$ in Fig. 2.8a. This reaction can be easily calculated from the equilibrium of the forces on the strip along the vertical direction:

$$R = T_0 \sin(\theta_0 + \delta) - (m_1 + m_2)g \tag{2.3}$$

where θ_0 and δ have already been computed. The minimum mass of the counterweights corresponds to the limit case $R = 0$ and can be obtained by substituting $T_0 = Mg$ and solving for M:

$$M_{min} = \frac{(m_1 + m_2)g}{\sin(\theta_0 + \delta)} \tag{2.4}$$

This expression is a function of λ_0 and H_0 through the angles θ_0 and δ, and its maximum value increases as λ_0 and H_0 decrease. Therefore, choosing $H_0^{min} = 250$ mm as the minimum height of interest and $\lambda_0 = 0$, the plot in Fig. 2.9 is obtained.

The plot shows that the minimum mass for which the reaction of the release system would be positive is $M_{min} = 25$ g (for a strip without membrane, it would be $M = 12$ g). The plot also shows that, for $M > 25$ g, the fold angle quickly reaches a plateaux and becomes independent of the fold mass. However, for the

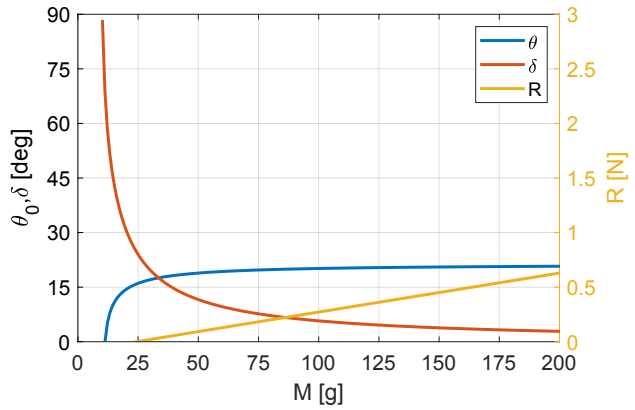

Figure 2.9: Initial fold angle θ_0 and cord angle δ as a function of the mass of the counterweights M, for a folded strip with $\lambda_0 = 0$ and $H_0 = 250$ mm. The right axis shows the reaction force from the release mechanism, which must be non-negative for the cords to support the self-weight of the strip.

chosen initial conditions, the maximum fold angle that can be achieved is only $\theta_0 = 20°$. To understand what range of initial fold angles can be achieved for different combinations of initial conditions, the equations above were solved for $\lambda_0 \in [0, 1]$ and $H_0 \in [0, 760]$ mm. In this case, a large value of mass $M = 200$ g was used, to capture the asymptotic value of θ_0. The results are presented as a contour plot in Fig. 2.10.

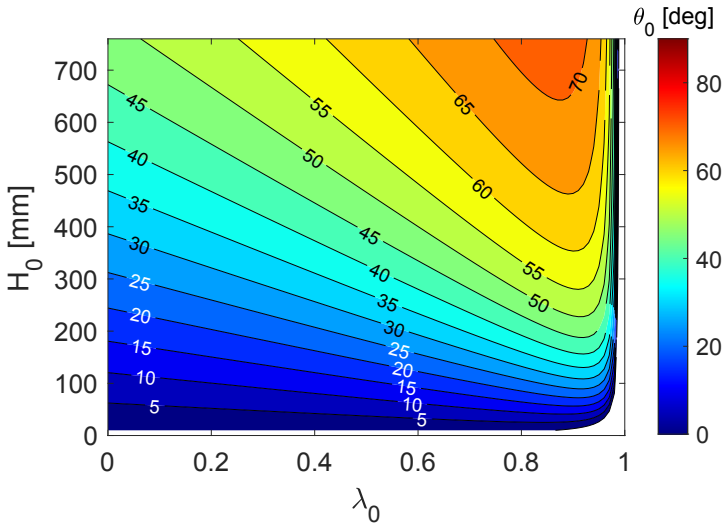

Figure 2.10: Maximum fold angle for different combinations of initial height H_0 and initial fold location λ_0.

The plot shows that the initial fold angle θ_0 increases both with H_0 and λ_0. For the range of heights considered, the maximum fold angle that can be achieved is about

45° when the strip has a single fold at the center, and about 60° when the folds are at $\lambda_0 = 0.5$.

Based on these considerations, a range of masses $M \in [20\,\text{g}, 100\,\text{g}]$ and initial heights $H_0 \in [250\,\text{mm}, 760\,\text{mm}]$ was identified. Experiments were carried out to explore the parameter space defined by λ_0, H_0, and M in these ranges. It was observed that the qualitative behavior of the strip during deployment does not vary significantly for most combinations of those parameters. Therefore, this chapter focuses on one specific set of parameters ($H_0 = 400$ mm, $M = 50$ g, $\lambda_0 = 0.45$), corresponding to an intermediate point of the parameter space, but representative of the behavior for a wider range of initial conditions. Results for different combinations of initial height, mass, and fold locations can be found in Sec. 2.7.

2.3 Experimental Setup

2.3.1 Strip Prototypes

Two strip prototypes based on the architecture presented in Fig. 2.4 were manufactured, one with and one without the membrane. Both prototypes, shown in Fig. 2.11, have the same nominal length $2L = 1125$ mm and have longerons placed 200 mm apart and connected by 5 equally spaced battens. The longerons have nominal flange radius $r = 12.4$ mm, flange opening angle $\alpha = 90°$, and web width $w = 8$ mm.

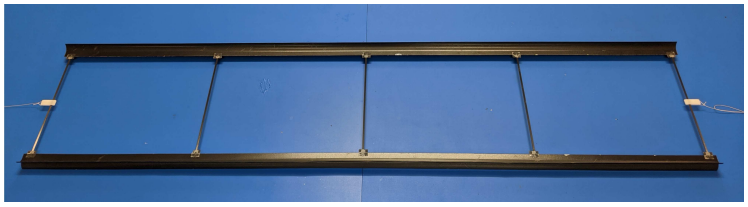

(a) Strip 1, without membrane

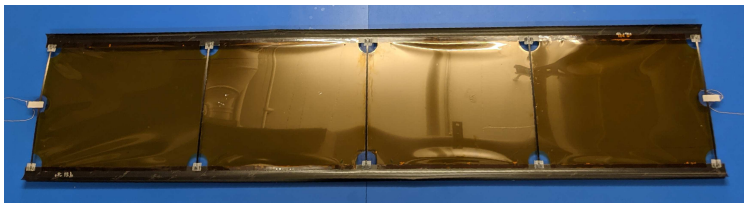

(b) Strip 2, with membrane

Figure 2.11: Strip prototypes.

The flanges were manufactured from ultra-thin composite prepregs. The stacking sequence was $[\pm 45_{GFPW}/0_{CF}/\pm 45_{CFPW}]$, where GFPW represents a Scrim Glass fiber plain weave (25 gsm), and CF denotes a unidirectional MR70 carbon fiber

(30 gsm). Both laminates had been pre-impregnated with 380 CE cyanide ester resin by North Thin Ply Technology. An additional $[\pm 45_{GFPW}]$ bonding layer (25 gsm Scrim Glass with the same resin) was interposed between the flanges in the web region. This laminate design has been previously shown to induce low stress concentration during coiling of TRAC longerons [56] and its stiffness properties have been characterized [57].

The battens consist of pultruded carbon fiber rods, with a 3 mm $\times$ 0.6 mm rectangular cross section, provided by CST The Composite Store, Inc. They are connected to the web of the longerons by Ω-shaped sleeves, made of 2-ply JPS 1067 glass fiber composites with PATZ-F4A resin. The strips are supported at the ends by PTFE-coated glass fiber cords, attached to 3D-printed plastic connectors, bonded to the center of the terminal battens. The two strip prototypes nominally differ only for the presence of a 50-μm-thick Kapton film bonded to the web of the longerons on one of the prototypes. The geometry of each strip was measured with a FaroArm laser scanner. The actual radius and opening angle of the longerons were computed from the point cloud generated by the FaroArm. The measured properties of the strips are reported in Table 2.1.

	Flange radius r [mm]	Flange angle α [°]	Total mass [g]
Strip 1 without membrane	12.4 ± 0.7	91.2 ± 4.6	23
Strip 2 with membrane	13.1 ± 1.1	80.3 ± 3.2	46

Table 2.1: Geometry and mass of strip prototypes.

2.3.2 Moment-Rotation Relationship for the Strips

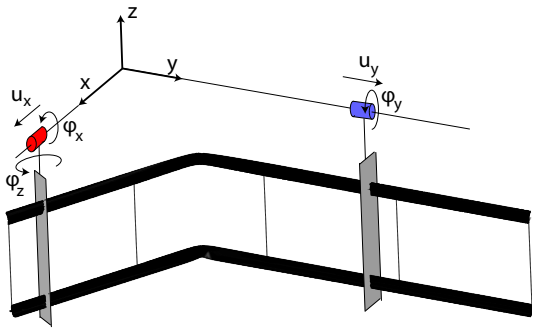

Figure 2.12: Schematic of experimental setup for strip bending tests.

The moment-rotation relationship for an elastic fold in the strip is of great importance, as it drives the self-deployment of the structure. It was measured with a large-rotation bending apparatus [84] that measures the bending moments at the end of the test sample as a function of the applied rotation, during quasi-static unfolding of a strip with an elastic fold.

The apparatus consists of two sliders mounted in orthogonal directions, as shown in Fig. 2.12. The strip was attached to acrylic clamps (grey in the figure) spaced 400 mm which were connected to the sliders. Note that the clamps were not symmetrically located with respect to the ends of the strip, to avoid forming a fold close to the central batten, because folds near a batten are energetically unfavorable and carry larger moments. One of the sliders can freely translate along and rotate around the y-axis, but rotations around the z-axis (bending axis) are not allowed. The other slider can translate along and rotate around the x-axis; its rotation about the z-axis is controlled by a brushless DC motor. Each slider is equipped with New Way air bearings (25.4 mm diameter, 90 psi operating pressure). Mini40 force/torque sensors by ATI Industrial Automation are attached to both sliders and measure all force and moment components applied by the structure, with a force resolution of 0.2 N and a torque resolution of 0.25 Nmm.

To carry out a test, the strip was initially folded to an angle of 35° by manually forming an elastic fold at the center. Then, a rotation in the opposite sense to the folding direction was applied in small increments, until the strip had fully deployed. The results of unfolding tests on the two strips are reported in Fig. 2.13. Each test was repeated 3 times, showing a consistent behavior, with rms error of about 2 Nmm for both strips. The maximum variation of the peak moment was 23 Nmm for the strip without membrane, and 14 Nmm for the strip with membrane, corresponding to respectively 6% and 13% of the peak values.

It was observed that during the unfolding process the fold undergoes shape and position changes . Specifically, for angles greater than 15°, the fold remains symmetric and the bending moment is mostly constant, slightly decreasing with the angle. At approximately θ =15°, a sudden increase in the bending moment occurs, and the shape of the fold switches from a symmetric to an asymmetric configuration. For smaller values of θ, the moment keeps increasing until it reaches a peak for $\theta \approx 3°$, after which the fold disappears, as a local buckle forms in the longeron flange that is under compression.

Both strips exhibited similar qualitative behavior, although the following quantitative

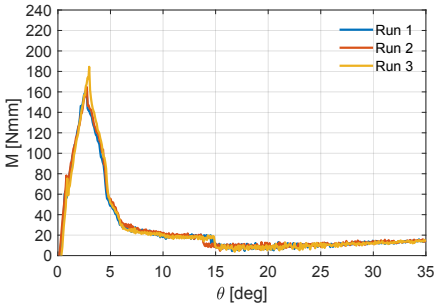

(a) Bending tests of strip without membrane

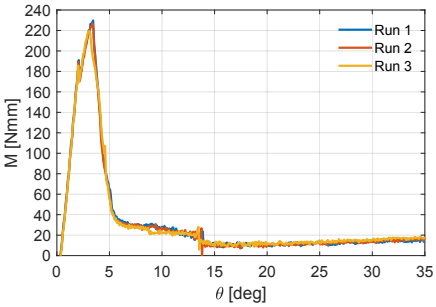

(b) Bending tests of strip with membrane

Figure 2.13: Moment-rotation relation for the two strip prototypes.

differences were noted. For $\theta > 15°$, the bending moment in the strip without membrane was about 15% higher than for the strip with the membrane, due to the larger flange angle of this strip, see Table 2.1. The strip with the membrane had 30% higher peak moment, due to the fact that the folds on the two longerons disappear at the same time, unlike the strip without the membrane, possibly due to the additional coupling between the longerons that is introduced by the membrane.

2.3.3 Experimental Apparatus

The test structure and experimental apparatus, consisting of the suspension system, the release mechanism, and the metrology system, are shown in Fig. 2.14.

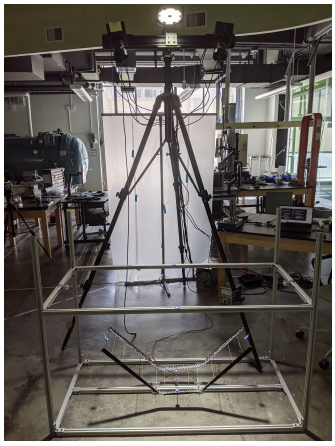

(a) Experimental setup with metrology system

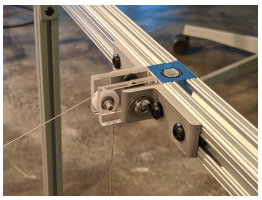

(b) Detail of pulley

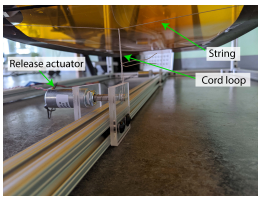

(c) Detail of release mechanism

Figure 2.14: Experimental apparatus for strip deployment tests.

The suspension system included two 12.4-mm-diameter, nylon miniature pulleys mounted on ball bearings (SP4088, from Carl Stahl Sava Industries). The pulleys were installed on a support structure consisting of aluminum T-slotted frames. By varying the height of the pulleys from the ground, the initial fold angle of the strip could be adjusted, as previously discussed in Sec. 2.2.3. It was shown by analysis that the inertia of the pulleys contributes to less than 1% of the total inertia of the system, and hence its effect was considered negligible. However, the analytical model suggested that friction in the ball bearings can significantly affect the dynamics of the suspension system, and therefore a detailed characterization of the friction of the system was performed. It will be discussed in the next sub-section.

The release mechanism was responsible for holding the strip in the folded configuration and releasing it upon a deployment command. The release actuation was provided by two R12X12 DC pull-type linear actuators (24 V, 2.5 W) from Magnet-Schultz of America. These actuators consist of solenoids that pull a central magnetic shaft upon powering. They were connected in parallel to a power supply, in order to achieve synchronized release, within 2 ms. The strip was connected to the release actuators by cords with negligible mass. Specifically, two cords across the strip were attached to the webs of the longerons; their location along the strip defined the initial position of the elastic folds. A cord loop was placed across the centers of the cords and the shaft of the corresponding release actuator, and was held taut by the counterweights of the suspension system. By retracting the shafts of the actuators, the cord loops were released and the deployment was initiated.

Lastly, the metrology system consisted of two Photron UX100 high speed cameras set at a frame rate of 500 fps, to acquire monochrome images. The system was configured to provide a 1.2 m field of view with 500 mm depth of field. A 72,000 lumens REL Sure Bright light module with 120 white LEDs completed the setup. A speckle pattern was applied to the top face of the longerons, with approximate speckle size of 5 mm, to perform Digital Image Correlation (DIC) on the image pairs obtained during each test. Photogrammetry was used to extract the coordinates of several targets placed on both the strip and the aluminum frame, which were used to define a global coordinate system for the experiment. Both DIC and photogrammetry measurements were performed using the VIC3D software by Correlated Solutions.

The experimental setup described above was used to perform deployment tests both in air and in vacuum. The tests in vacuum were performed in an altitude chamber with internal volume of 2.4 m $\times$ 2.4 m $\times$ 2.4 m, at NTS Santa Clarita, CA. During

these experiments, the pressure was maintained at 55 torr (corresponding to about 7% of standard atmospheric pressure). The temperature within the chamber, which was not actively controlled, varied between 20°C and 30°C.

2.3.4 Suspension System Characterization

The friction torque in the pulley bearings of the suspension system was measured experimentally. The experimental setup consisted of two masses $M_1 \neq M_2$ attached to the opposite ends of a cord, running on a pulley as shown in Fig. 2.15a. The masses, initially held stationary, started moving vertically as soon as they were released, with the heavier weight accelerating downwards. A target placed on this weight was tracked using the high speed camera system, which acquired images at 500 fps. Photogrammetry was performed with VIC3D to extract the coordinates of the target. From the measured vertical coordinates, the variation of the target height, h, was obtained as a function of time, Fig. 2.15b, and a second-order polynomial of the form $h(t) = c_2t^2 + c_1t + c_0$ was fitted to these data to estimate the acceleration of the mass:

$$\ddot{h} = 2c_2 \tag{2.5}$$

Each experiment was repeated 3 times, and the measured accelerations were repeatable within 1.5% of their mean value. The pulley friction torque was obtained from the equation of motion:

$$(M_1 - M_2)gR - T_f = \left[I_p + (M_1 + M_2)R^2\right] \frac{\ddot{h}}{R} \tag{2.6}$$

where R and I_p are the radius and the second moment of inertia of the pulley, respectively, and T_f is the friction torque on the pulley. Solving for T_f, substituting $\ddot{\beta} = \ddot{h}/R$, and using $\ddot{h}$ from Eq. 2.5 gives:

$$T_f = (M_1 - M_2)gR - \left[I_p + (M_1 + M_2)R^2\right] \ddot{\beta} \tag{2.7}$$

T_f was computed for nine different combinations of M_1 and M_2 in the range [15 g,... 100 g]. Given the relatively low angular velocity of the pulley during a deployment experiment, it is reasonable to neglect viscous effects in the pulley ball bearing, and to assume that friction is entirely due to the elastic rolling resistance [40], which increases linearly with the normal load on the bearing. Therefore, for the case shown in Fig. 2.15a, the normal force F_n is given by:

$$F_n = (M_1 + M_2)g - (M_2 - M_1)\ddot{\beta}R \tag{2.8}$$

where the first term on the right-hand side describes the static contribution from the weight of the two masses, whereas the second term captures the inertial effects. This equation indicates that the friction torque depends on both the sum $M_1 + M_2$ and the difference $M_2 - M_1$ of the two masses. Figure 2.15c shows a quadratic polynomial fit of the measured values of T_f as a function of $M_1 + M_2$ and $M_2 - M_1$. The plot shows that the friction increases with $M_1 + M_2$, but it becomes very small if the masses are very different (as $F_n \rightarrow 0$ when $M_2 >> M_1$) or if they are very similar (in which case the velocity of the pulley is very low).

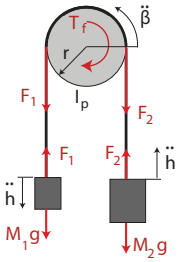

(a) Schematic of the friction characterization experiment

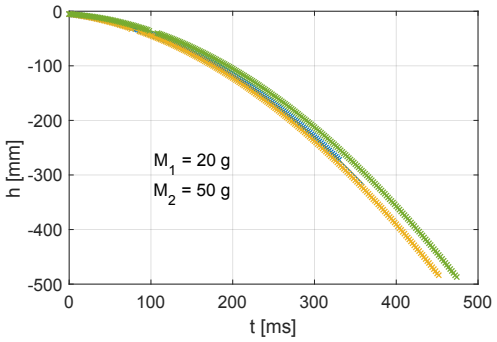

(b) Example of measurements from photogrammetry for $M_1 = 20$ g and $M_2 = 50$ g. Each color corresponds to a different run of the same experiment

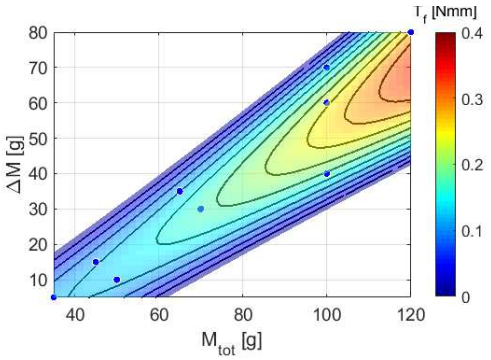

(c) Measured values of friction torque T_f and fitting surface as a function of M_{tot} and ΔM

Figure 2.15: Characterization of pulley friction torque.

2.4 Experimental Results

Deployment experiments were performed on the two strip prototypes (with membrane and without membrane) both in air and in vacuum. Each experiment was repeated three times and the results of repeated tests were consistent. Overall, the

experiments exhibited very similar qualitative behavior, Figure 2.16 shows snapshots from the deployment in vacuum of the strip with membrane, starting from the folded configuration, with H_0 = 400 mm. The strip maintained its initial symmetry until the end of deployment, with the elastic folds remaining stationary and opening out monotonically. At t = 300 ms, symmetry was lost as one of the elastic folds (on the right hand side) latched before the other fold. After both folds had latched, the strip began to vibrate in a small amplitude, smoothly curved mode.

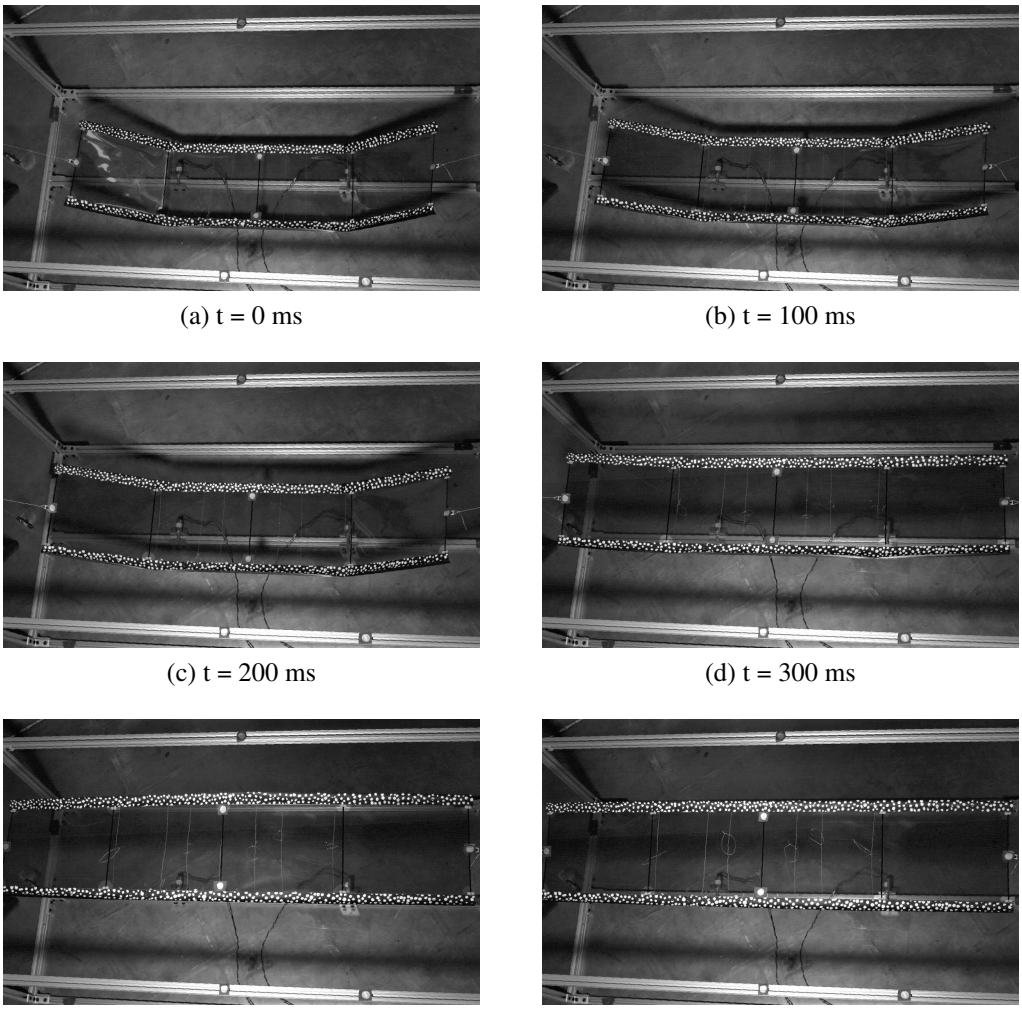

(a) t = 0 ms (b) t = 100 ms

(c) t = 200 ms (d) t = 300 ms

(e) t = 400 ms (f) t = 500 ms

Figure 2.16: Snapshots from deployment of strip with membrane, in vacuum.

The images captured by the high speed cameras were processed with DIC, which provided a point cloud for each longeron, at each frame. An algorithm was developed in MATLAB to identify and track the elastic folds and also measure the fold angles. The algorithm consists of an initialization phase, which is run on the first image

taken during the experiment, and a loop, performed on all subsequent frames. The initialization consists of the following steps:

1. Definition of global coordinate frame: the coordinates of 3 targets located on the aluminum frame (P_0, P_1 and P_2 in Fig. 2.16a) are extracted with photogrammetry and are used to define a global coordinate system consistent with Fig. 2.7.

2. 2D projection: the point clouds are projected on the x-z plane (see Fig. 2.7) for increasing values of x.

3. Definition of curvilinear abscissa: the centerline of each longeron is obtained by computing the median of the coordinates of a 50 points-moving window (Fig. 2.17a). From a statistical perspective, the median is more robust than the mean to outliers in noisy data [68] and therefore median filters are often used in combination with DIC [37]. A curvilinear abscissa $s = \xi L$ (Fig. 2.7) is defined on the centerline, using $s_i = s_{i-1} + \Delta s_i$, for $i = 2, ...N_p$. Here, Δs_i is the distance between 2 consecutive points on the centerline and N_p is the total number of points. The origin of the abscissa s is defined at the center of the strip. A value of s is then assigned to each point in the cloud, by projecting it on the centerline of the longeron and interpolating the previously computed values of s on the centerline. Note that the curvilinear abscissa defines a body fixed frame, which identifies each point in the cloud, throughout deployment.

4. Computation of local tangent: the local tangent $\mathbf{T}(s)$ to each longeron is computed by performing a Principal Component Analysis (PCA) on a 50 points-moving window from the point cloud [46]. By performing an eigenvalue analysis on the covariance matrix of the coordinates of the points in the moving window, this algorithm returns the directions along which the points are distributed. The direction associated with the largest variance identifies, in this case, the local tangent to the longeron. The use of PCA allows to filter the noise due to some of the points being on the web and others on the flange of the longerons, resulting in a robust algorithm. Each local tangent is associated with a value of the curvilinear abscissa that corresponds to the median of the abscissas of the points in the moving window. By computing the dot product of the local tangents with the global x-axis, the local angle $\theta(s)$ of the longeron as a function of s is obtained, Fig. 2.17b.

5. Identification of folds: the longitudinal curvature $\kappa(s)$ of each longeron is computed from $\kappa(s) = \|\frac{d\mathbf{T}(s)}{ds}\|$, where the derivative is computed numerically using a symmetric finite difference scheme. The resulting curvature is first smoothed using a 50 point-moving average, Fig. 2.17c. The two highest peaks in the $\kappa(s)$ curve define the initial location of the elastic folds.

Once this initialization has been completed, the algorithm iterates over each frame, repeating only steps 4) and 5) of the list above. To track the localized folds, the search for the peaks in longitudinal curvature is performed in a ± 20 mm region centered at the location of the folds from the previous frame. In this way, the folds can be tracked even when their longitudinal curvature becomes small, towards the end of deployment, and hard to distinguish from the noise floor.

The outcome of the algorithm described so far is a map showing the distribution of orientation and curvature along each longeron, as a function of time. An example of these maps is shown in Fig. 2.18 for the deployment in air of the strip without mem-

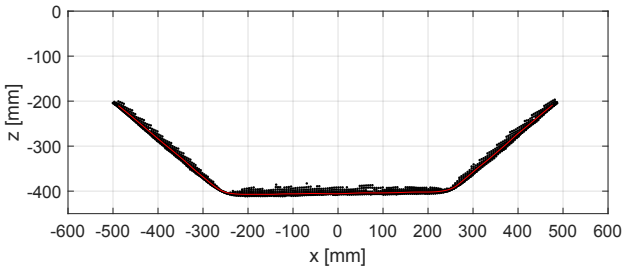

(a) Point cloud of a longeron projected on the x-z plane, and its centerline (in red)

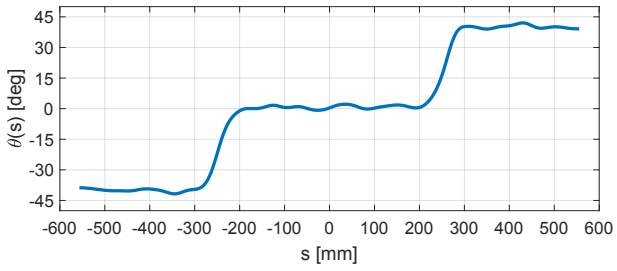

(b) Orientation of the local tangent to the longeron, measured from the x-axis

Figure 2.17: Calculation of local orientation and longitudinal curvature of a longeron, starting from a point cloud extracted from DIC, at a given time step. Data from deployment test in air of a strip without membrane.

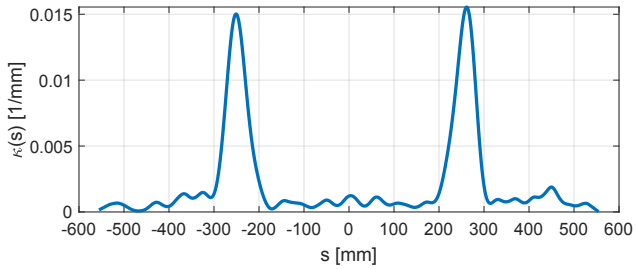

(e) Distribution of longitudinal curvature on the longeron

Figure 2.17: Calculation of local orientation and longitudinal curvature of a longeron, starting from a point cloud extracted from DIC, at a given time step. Data from deployment test in air of the strip without membrane (cont.)

brane. In these maps, the curvilinear abscissa on the y-axis is non-dimensionalized with respect to the length of the strip using $\xi = \frac{s}{L}$, so that $\xi \in [-1, 1]$, with $\xi = 0$ being at the center of the strip. The results for the two longerons are very similar and therefore only one map has been shown.

Figure 2.18a shows that in each longeron there are three distinct regions with uniform orientation. Specifically, the central region is approximately horizontal, whereas the other two regions have equal and opposite slope, decreasing over time until the strip fully deploys. Figure 2.18b shows two well-defined curvature peaks, corresponding to the location of the elastic folds, which remain stationary during deployment. Although these maps provide a full-field characterization of the deployment process, a more compact description of the deployment test is useful for easier comparison of the results. Therefore, in the rest of this chapter, the results are presented in terms of the angle of the folds and the height of the center of the strip vs. time. These plots provide insights into the dynamics of the elastic folds, as well as the rigid body translation of the structure. The angle of each fold is computed by taking the median of $\theta(s)$ between the location of the fold and the end of strip, at each time increment. The height of the center of the strip is provided by the z coordinate of two targets placed next to the center of each longeron (C_1 and C_2 in Fig. 2.16a), tracked with photogrammetry. The results for each experiment are shown in the rest of this section.

Figure 2.19a shows plots of the angle of the elastic folds as a function of time, for the strip without membrane. Since each longeron has two folds, the plot contains two lines starting from equal and opposite angles. Solid, dashed, and dotted lines correspond to different runs of the same experiment. Also, green and blue lines correspond to the two longerons for the tests in air, orange and red lines to the

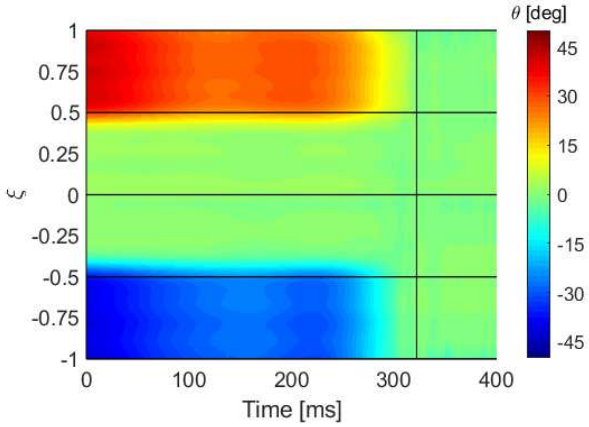

(a) Map of local orientations

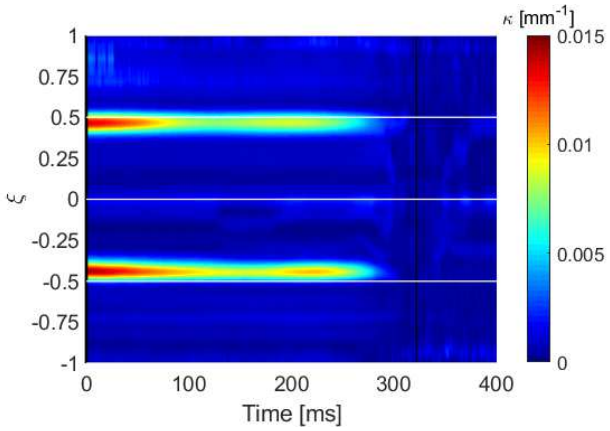

(b) Map of longitudinal curvature

Figure 2.18: Distribution of local orientation $\theta(\xi)$ and longitudinal curvature $\kappa(\xi)$ over time for a strip without membrane deploying in air. ξ represents a non-dimensional curvilinear abscissa, which is 0 at the center of the strip and ± 1 at the ends. Results are shown for one longeron only.

longerons for the tests in vacuum. In this plot, the deployment time can be defined as the time when all fold angles become zero for the first time.

Overall, the tests are symmetric, with both longerons undergoing the same angle variation on both folds. The fold angle starts from approximately $\pm 42°$, and then decreases until becoming zero at about $t = 300$ ms. During deployment, an oscillation of the fold angle, with a period of about 220 ms, can be observed. After reaching $\theta \approx 0°$, the localized folds disappear, and the strip vibrates with small-amplitude deformations.

Comparing the tests in vacuum and in air, it can be observed that there is almost no difference, indicating that the effects of added air mass and air drag on the unfolding

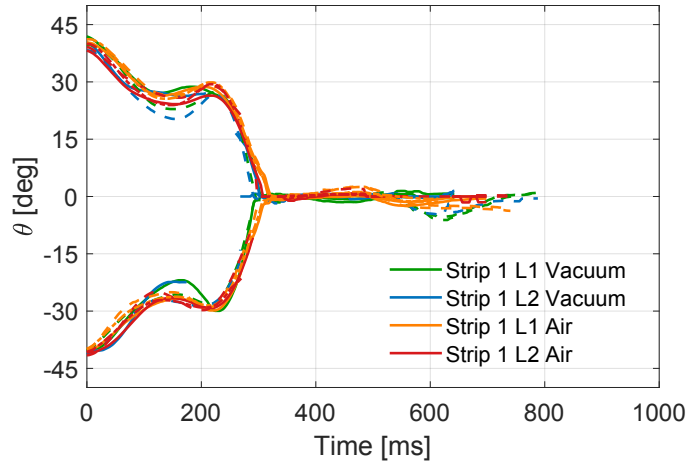

(a) Fold angle

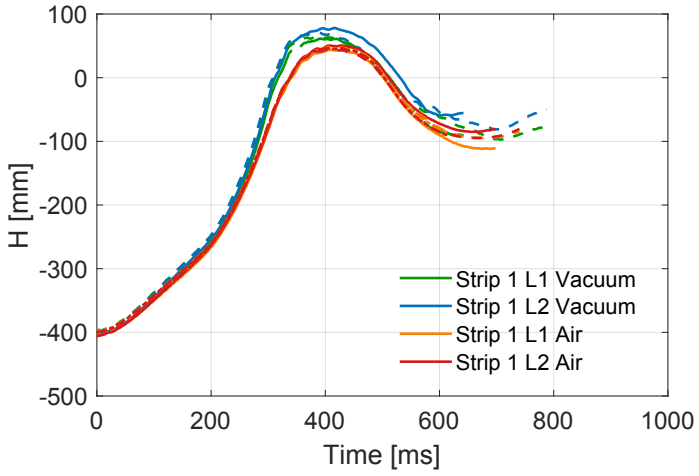

(b) Height of strip center

Figure 2.19: Experimental results for strip without membrane. Initial conditions: $M = 50$ g, $\lambda_0 = \pm 0.45$, $H_0 = 400$ mm. Solid, dashed, and dotted lines correspond to different runs of the same experiment.

process of a strip without membrane are negligible. The plot in Fig. 2.19b shows the height of the center of the strip during deployment (with the zero corresponding to the height of the pulleys). The plot shows that the height increases monotonically until the strip is fully deployed at $t = 300$ ms. Afterwards, the structure continues to move upwards as a rigid body and it overshoots $H = 0$, reaching a maximum height at $t = 400$ ms. The longerons maintain the same height during deployment, indicating that there is no twisting of the strip. In this case, comparing the experiments in air and in vacuum, it can be noticed that the latter is faster during the last portion of deployment (after $t = 250$ ms), and it reaches a higher peak at approximately the

same time.

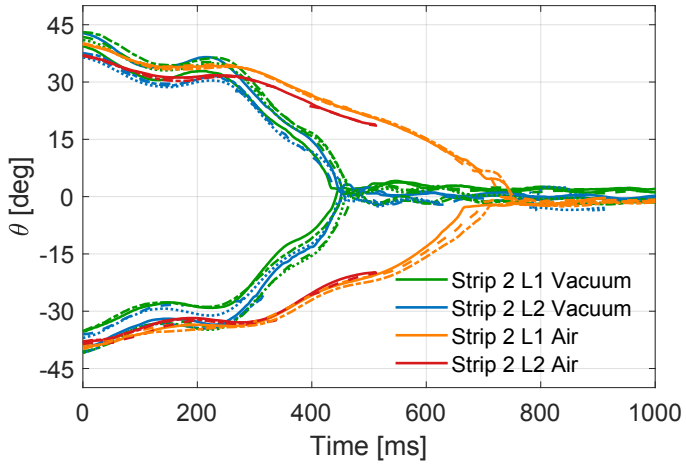

(a) Fold angle

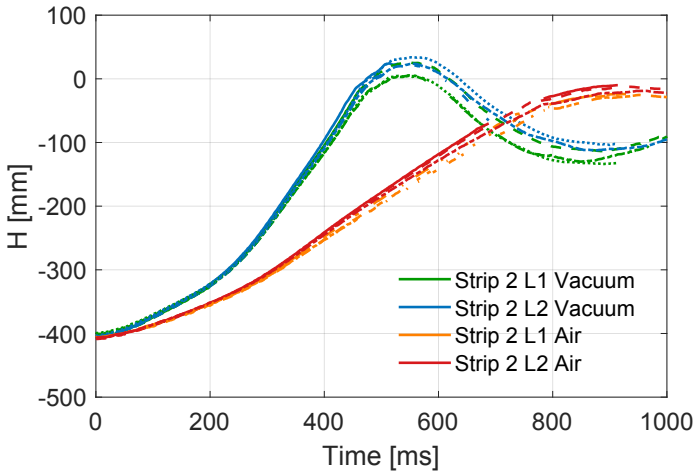

(b) Height of strip center

Figure 2.20: Deployment results for experiments on strip with membrane, in air and vacuum. Initial conditions: $M = 50$ g, $\lambda_0 = 0.45$, $H_0 = 400$ mm. Solid, dashed, and dotted lines correspond to different runs of the same experiment.

Figure 2.20 presents the results for the strip with membrane, both in air and in vacuum. Again, the behavior of the strip is symmetric and the three runs of the experiment are consistent. However, for this strip the presence of air plays a significant role, with the deployment in air being about 1.7 times slower than in vacuum (750 ms vs. 450 ms). Similarly to the strip without membrane, the fold angle oscillates during deployment, with an average period of 280 ms in air vs. 220 ms in vacuum. Also, the amplitude of the oscillation is smaller for deployment in air than in vacuum. Figure 2.20b shows the height of the center of the longerons

over time. For deployment in air, the strip reaches its final height after 950 ms, never overshooting the vertical location of the pulleys. For deployment in vacuum, the vertical motion is much faster and the maximum height is reached after 550 ms.

In summary, the experiments have shown that, for the suspension system concept studied in this chapter (and for the chosen values of H_0 and M), the elastic folds do not move and essentially behave as fixed, self-latching elastic hinges, deploying in a consistent and repeatable fashion. If the structure is folded in a symmetric way, symmetry is also preserved throughout the deployment, which is very advantageous as it simplifies the development of mathematical models to predict the dynamics of the structure.

2.5 Numerical Model

Numerical simulations of the packaging and deployment of the strip were carried out with the Simulia Abaqus Explicit 2020 finite element software. The Abaqus model is shown in Fig. 2.21. The longerons were modeled with S4R reduced-integration shell elements, and their material properties were defined using direct specification of the ABD matrix for the flanges and the web, based on previous measurements on coupons of a similar laminate [57]. The battens were modeled with B31 linear beam elements. The Ω-shaped connectors between the longerons and the battens were assumed rigid and were modeled with kinematic coupling constraints between the end nodes of the battens and a region of the longeron web of the same size as the physical connector. The suspension system was modeled using a combination of one-dimensional connector elements. More details about this model are provided later in this section. The membrane was bonded to the webs of the longerons and to the battens using tie constraints.

A uniform mesh of approximately 2 mm × 2 mm was used for all parts of the model. Based on the essentially symmetric deployment observed in the experiments, symmetry about the mid-plane of the strip was assumed, thus reducing the total number of elements by a factor of two. The resulting model contained 81,355 nodes and 79,556 elements, i.e. 24,156 shell elements and 54,900 membrane elements.

2.5.1 Membrane Formulation

Because of their small thickness, membranes have very small bending stiffness and cannot sustain any in-plane compressive loads. Wrinkling instabilities arise whenever the principal stress components in a membrane have opposite sign. A detailed numerical characterization of the wrinkles, in terms of wavelength and

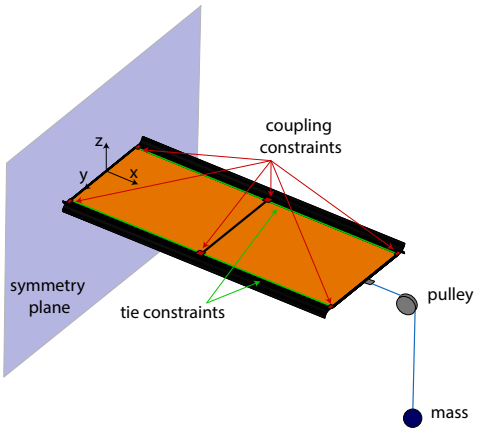

(a) Finite element model of a symmetric strip. Longerons and battens are connected by rigid coupling constraints; tie constraints connect the longerons to the membrane

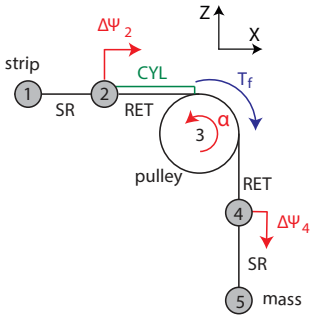

(b) Schematic of suspension system model, using 1D connector elements. Slip ring (SR) elements model the cord passing over the pulley; retractor (RET) elements convert the motion of the cords in rotation of the pulley. Cylindrical (CYL) elements introduce friction in the pulley

Figure 2.21: Description of finite element model of strip with membrane.

amplitude, requires a shell element formulation, capable of capturing the small, but still finite, bending stiffness of the membrane [106]. However, this approach is computationally expensive, as very fine meshes are required to accurately capture the short wavelength of the wrinkles. On the other hand, the onset and orientation of the wrinkles can still be predicted accurately with less expensive membrane elements [106], by implementing a wrinkling theory into an *ad hoc* material model, known as the Iterative Material Model (IMP) [71][72]. This model is based on a mixed stress/strain criterion to identify three regimes for the membrane: slack, wrinkled, and taut.

Each regime is associated with a different material tangent stiffness matrix. For a taut membrane, the constitutive relation is based on the standard stiffness matrix $\mathbf{D_t}$ for an isotropic membrane. A slack state corresponds to no stress in the membrane, hence the stiffness matrix $\mathbf{D_s}$ is null. Finally, for a wrinkled membrane, an effective stiffness matrix $\mathbf{D_w}$ is defined, based on the assumption that the wrinkles are aligned with the direction of principal stress in the membrane, and that the stress is zero in

the direction normal to the wrinkles. Hence, the resulting model is expressed as:

$$\mathbf{D_s} = \mathbf{0} \tag{2.9a}$$

$$\mathbf{D_w} = \frac{E}{2}\begin{bmatrix} 2(1+P) & 0 & Q \\ 0 & 2(1-P) & Q \\ Q & Q & 1 \end{bmatrix} \tag{2.9b}$$

$$\mathbf{D_t} = \frac{E}{1-\nu^2}\begin{bmatrix} 1 & \nu & 0 \\ \nu & 1 & 0 \\ 0 & 0 & (1+\nu)/2 \end{bmatrix} \tag{2.9c}$$

where E is the elastic modulus and the parameters P and Q are functions of the engineering strains ϵ_x, ϵ_y and γ_{xy}, defined as:

$$P = \frac{\epsilon_x - \epsilon_y}{\epsilon_1 - \epsilon_2} \tag{2.10a}$$

$$Q = \frac{\gamma_{xy}}{\epsilon_1 - \epsilon_2} \tag{2.10b}$$

where ϵ_1 and ϵ_2 are the principal strains.

Various implementations of the IMP algorithm have been successfully used in finite element codes, both with implicit [1] and explicit [14] integration schemes. The particular implementation that was used in the present study was the Abaqus Explicit VUMAT subroutine in Ref. [14].

2.5.2 Suspension System Model

Models for cables and pulleys have been developed in the context of cranes, electrical transmission lines, and seat belts. Electrical transmission lines loaded by self-weight have been modeled as truss elements with zero-sized frictionless pulley were allowed to slide[7]. A formulation that accounts for friction between cords and pulleys in cranes[49] allows for different tensions in the cord segments on the two sides of the pulley, but does not consider inertial effects on the pulley.

The chosen model was based on seat belt systems models for dynamic simulations of automotive crash events [23] [41], which use combinations of slip ring and retractor elements. Slip rings are 2-node elements that enable a "material flow" degree of freedom, which allows mass to enter or exit the element, and hence to increase or reduce the element's length without elastic deformation. Connecting two slip rings in series, the mass exiting from one element enters the other element through their

shared node. Retractor elements, instead, convert the material flow at one node into rotation of the other node. Both of these elements are available in Abaqus.

A schematic model of a suspension pulley is shown in Fig. 2.21b: the circles 1-5 represent the nodes of the connector elements. Node 1 corresponds to the strip-cord connector and is connected to the central nodes of the strip outermost batten using MPC beam constraints. Node 3 represents the pulley, which has only one rotational degree of freedom, about the y-axis. Node 5 represents the counterweight attached to the end of the cord, whereas nodes 2 and 4 are auxiliary intermediate nodes. Slip ring (SR) elements model the cords, connecting nodes 1-2 and 4-5. To prevent the cords from experiencing axial compression during dynamic loading, a bi-linear elastic model is assigned to the slip rings, with tensile stiffness $K_t = 1000$ N/mm and compressive stiffness $K_c = 1$ N/mm. A sensitivity study for these parameters showed that, under the expected loads, the cords effectively behave as rigid in tension and slack in compression.

To take into account the inertial effects of the pulley, retractor elements (RET) between 2-3 and 4-3 convert the material flow at nodes 2 and 4 into rotation of node 3, according to:

$$\beta = \frac{\Delta\Psi_2}{R} = \frac{\Delta\Psi_4}{R} \tag{2.11}$$

where R is the radius of the pulley and $\Delta\Psi_2$, $\Delta\Psi_4$ define the material flow at nodes 2 and 4. Note that $\Delta\Psi_2 = \Delta\Psi_4$ because the retractor elements are connected in series.

Lastly, friction in the pulley bearing was captured by adding a second connector element between nodes 2 and 3, in parallel with the retractor element. This element models a cylindrical joint (CYL) that constrains all relative displacements between its nodes, except for the relative rotation about the y-axis. It provides the friction torque associated with the rotational degree of freedom, β, through the relationship:

$$T_3 = -\text{sign}(\beta) T_f \tag{2.12}$$

where T_f is a constant obtained from the experimental characterization of the suspension system described in Sec. 2.3.4.

The experiment presented in Sec. 2.3.4 was used as a benchmark to verify the model of the suspension system, whose results showed very good agreement both with an analytical solution and the experiment, see Fig. 2.22.

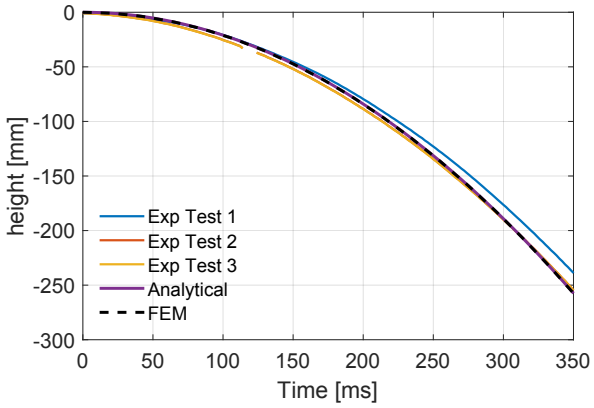

Figure 2.22: Verification of suspension system model using the experiment in Fig. 2.15a, with $M_1 = 20$ g and $M_2 = 50$ g.

2.5.3 Air Model

Modeling the effect of air on the deployment dynamics of lightweight large-area structures in a general way would require a coupled fluid-structure model[53] which would be beyond the scope of the present study. The approach that was adopted was based on existing models for the vibration of large membranes. Membranes vibrating in air have lower natural frequencies and higher damping than in vacuum [110], and for simple geometries it can be shown that the effect of air pressure in the equations of motion can be described in terms of a frequency-dependent added mass and a radiation damping term[53].

A simple vibration model [92] used a geometric argument to define an effective air volume, based on the velocity field for any chosen vibration mode and defined an added air mass that was distributed in a non-uniform fashion, in order to be maximum at the center of the membrane and zero at the edges. Higher fidelity models have been developed to explicitly include the air around the membrane, either using the boundary element method [102] or defining an air box with finite elements [53].

Hence, it was assumed that a half-cylindrical volume around the strip is forced to move with the structure, as shown in Fig. 2.23. The height of the added-air volume above the structure only varies with the transverse coordinate, and is given by:

$$z_a(y) = \sqrt{\left(\frac{W}{2}\right)^2 - y^2} \tag{2.13}$$

where W is the width of the strip. The corresponding mass of the air added to the

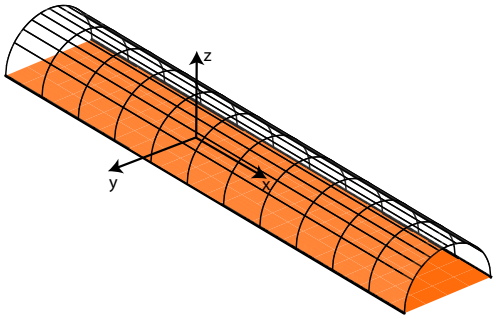

Figure 2.23: Volume of air mass added to the strip model with membrane.

structure is therefore:

$$m_a = 2\rho_a L \int_{-\frac{W}{2}}^{\frac{W}{2}} z(y)dy = \frac{\pi \rho_a W^2 L}{4} \tag{2.14}$$

where $\rho_a = 1.225\ kg/m^3$ is the standard air density.

The added air mass was uniformly distributed over the area of the Kapton membrane by scaling the mass of the membrane with the factor:

$$K = \frac{m_k + m_a}{m_k} \tag{2.15}$$

where m_k is the total mass of the membrane.

From an implementation standpoint, the added air mass could be introduced by increasing the density of the membrane. However, this would increase not only the inertia of the structure during deployment, but also its gravity loading, thus altering the starting folded configuration, as well as the height of the structure in its fully deployed state. Therefore, the added air mass was introduced by using mass scaling, which is a technique often used in quasi-static problems with explicit solvers. Mass scaling has the advantage of increasing the density of the material and, therefore, the stable time increment of the solver, drastically reducing the number of increments needed to perform long simulations. The mass scaling formulation in Abaqus only affects the inertial term in the equations of motion of the model, but the scaling coefficient is not included in the calculation of gravity loads. Therefore, it is ideal to model the effect of air on the dynamics of the structure, without affecting its equilibrium configuration.

Based on this model, the added air mass for a strip with membrane deploying in air was $m_a = 31.7$ g, which is compared to $m_0 = 46$ g for the strip with membrane. The added mass due to the residual air in the experiments in near-vacuum conditions, as described in Section 2.3.3, is 3.0 g, and it was neglected. For the strip without membrane, the air volume to consider would consist of two half-cylinders, with diameter equal to the width of the two longerons. The resulting added mass for deployment in air and would be 0.45 g and 0.04 g, respectively, and was neglected in the simulations.

The second aspect of the air-structure interaction, damping, can be simply expressed by a force D:

$$\frac{D}{A} = \frac{1}{2}\rho_a V_a^2 c_D \tag{2.16}$$

where ρ_a and V_a are the density and velocity of the undisturbed flow, A is the total area of the structure, and c_D is the drag coefficient, which depends on the geometry of the body and the Reynolds number. For a half-cylinder with the concave side facing the flow $c_D \sim 2.3$ [61].

This air drag model was implemented in Abaqus using a stagnation pressure load, defined as:

$$p_s = -c_s(\mathbf{v} \cdot \mathbf{n})^2 \tag{2.17}$$

with $\mathbf{v}$ being the velocity of the point on the surface where the load is applied, and $\mathbf{n}$ the local normal to the element. Substituting $|\mathbf{v}| = -V_a$ and equating the right-hand sides of Eqns. 2.16-2.17 gives:

$$c_s = \frac{1}{2}\rho_a c_D \tag{2.18}$$

In conclusion, air was only considered for the deployment in air of the strip with membrane, and its effects consisted of an additional mass, modeled by mass scaling with $k = 3.0$ of the membrane only. Damping was modeled as a stagnation pressure with coefficient $c_s = 1.4087\ kg/m^3$.

2.5.4 Simulation Details

The simulations were performed in Abaqus Explicit 2020 on the symmetric model shown in Fig. 2.21 and were organized in five steps, as described next.

1. In the first step, gravity was applied to tension the suspension cords. Localized folds were formed in the longerons by the application of equal and opposite

pressure of 0.1 MPa distributed on both flanges, over a 20 mm long region. This length includes enough elements to avoid locking of the mesh induced by excessive shearing.

2. A rigid cylinder with radius equal to the flange radius was used to push the strip into its folded configuration, using displacement control.

3. The residual kinetic energy in the structure was allowed to dissipate to less than 1% of the maximum strain energy. At this point, the folded configuration was considered to have reached equilibrium.

4. In the deployment step, the cylinder was instantaneously removed and the structure was allowed to self-deploy.

5. A final equilibrium step was carried out, to dissipate the kinetic energy from deployment and obtain the final configuration of the strip.

Numerical damping was used to reduce unphysical, high-frequency vibration that is a characteristic effect of explicit simulations. Previous studies have shown that a velocity-dependent viscous pressure, defined as $p = -c_v \mathbf{v} \cdot \mathbf{n}$, is very effective at dissipating such vibration in thin-shell structures [63][87]. Sensitivity studies of strip deployment have found that a small amount of linear bulk viscosity, proportional to the volumetric strain of the finite elements, is also beneficial to prevent numerical instabilities. Hence, a combination of both damping models was used. Table 2.2 presents the values of the main parameters for each of the simulation steps described above.

Step	Duration [s]	Linear bulk viscosity b_1	Viscous pressure c_v $[kg\ m^{-2}s^{-1}]$
1. Gravity	0.1	10^{-4}	10
2. Folding	0.5	10^{-4}	10
3. Equilibrium	0.3	10^{-4}	100
4. Deployment	1.0	10^{-8}	0
5. Equilibrium	0.3	10^{-4}	100

Table 2.2: Simulation parameters

The duration of the first three steps was chosen by trial and error, such that the correct folded configuration could be achieved in the shortest possible computational time. The duration of the deployment step was chosen to be longer than the actual deployment time of the strip (defined as the time at which the fold angles become

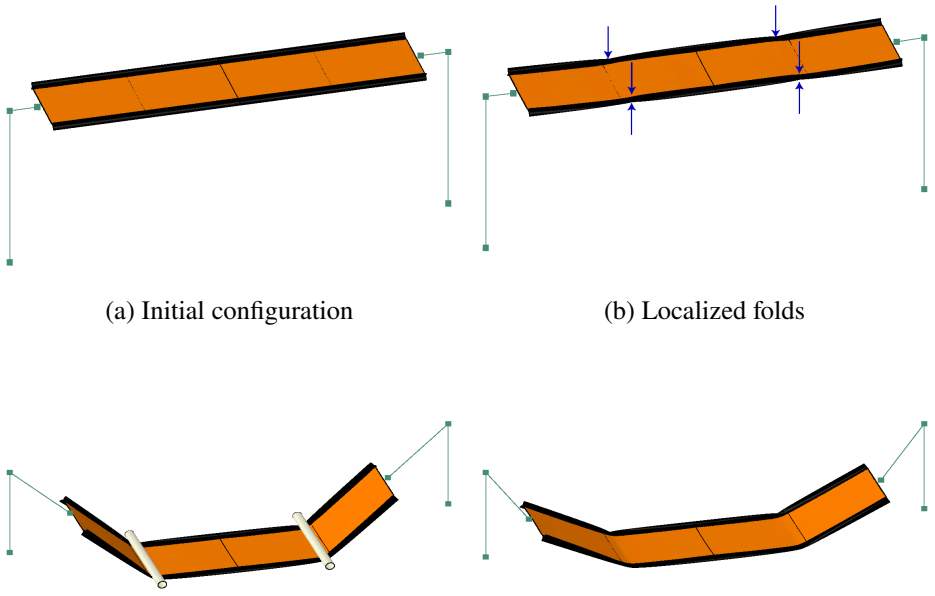

(a) Initial configuration

(b) Localized folds

(c) Folding

(d) Deployment

Figure 2.24: Simulation sequence (actual simulation only includes half of the strip): (b) Gravity is applied and the longerons are pinched to create localized folds. (c) Rigid cylinders are used to fold the structure. (d) After an equilibrium step to dissipate any residual kinetic energy from the folding step, the strip is deployed by instantaneously removing the cylinders. A second equilibrium step allows the strip to reach its final state.

zero for the first time). The duration of the final equilibrium step was chosen to allow sufficient dissipation of the end-of-deployment vibration and rigid body oscillation of the strip, using the previously chosen values of the numerical damping. With these settings, a complete simulation of packaging and deployment, using 8 CPUs on a server with 3.5 GHz Intel Xeon Gold 6144 processor took about 83 hours 45 minutes (30 hours 20 minutes for folding, 53 hours 25 minutes for deployment) for a strip with membrane, 25 hours 25 minutes for a strip without membrane (17 hours 20 minutes for folding, 8 hours 5 minutes for deployment).

Figure 2.25 shows the energy contributions thorughout the simulation of the strip with membrane, deploying in air. The artificial energy, associated with hourglassing modes in the finite element mesh, is very small throughout the simulation. The viscous dissipation increases during the folding process and is associated with the viscous pressure introduced during that step. In the deployment phase, it slightly

grows due to the air drag. In the final equilibrium step, the viscous dissipation further increases as additional damping is introduced in the model (in the form of viscous pressure and bulk viscosity) to reach the final equilibrium state. Regarding the strain energy of the strip, the largest contribution comes from the formation of the elastic folds during pinching of the longerons, in the first step of the simulation. Additional strain energy is stored during folding, as the angle of the folds is increased. During the deployment step, the strain energy gradually decreases to 10% of its value in the folded configuration, when the elastic folds latch in the deployed configuration. The residual strain energy, associated with elastic vibration of the strip, is released in the final equilibrium step.

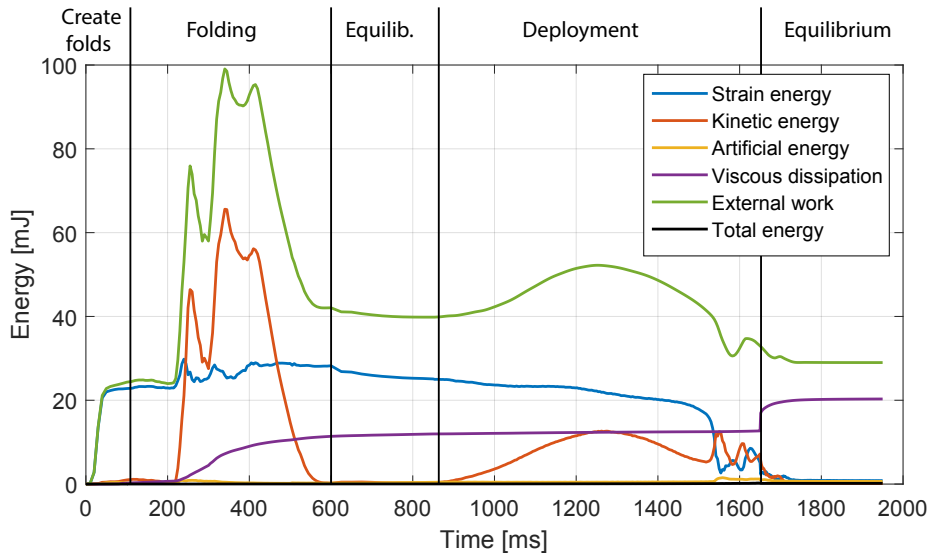

Figure 2.25: Energy balance for strip with membrane deploying in air. Initial conditions: $H_0 = 400$ mm, $\lambda_0 = 0.45$, $M = 50$ g.

Note that the folding process is not quasi-static, since the kinetic energy is quite high compared to the strain energy, but is dissipated to less than 1% of the strain energy before the initiation of deployment. The same approach was previously adopted in Ref.[63]. During deployment of the strip, the kinetic energy varies smoothly, reaching its maximum after 420 ms from the beginning of deployment; then, it suddenly increases when the elastic folds latch, and oscillates afterwards. In the final equilibrium step, the residual kinetic energy is almost entirely dissipated. Finally, the overall energy balance is described by the total energy E_{tot}, defined by the following equation (in which only the relevant terms for this problem have been

retained):

$$E_{tot} = E_S + E_A + E_{VD} + E_K - E_W = \text{const} \tag{2.19}$$

where E_S is the strain energy, E_A is the artificial energy, E_{VD} is the viscous dissipation, E_K is the kinetic energy, and E_W is the external work. Figure 2.25 shows that the total energy (in black) remains constant and approximately equal to zero throughout the entire simulation, indicating that there is no energy loss from or injected into the model.

2.6 Comparison between Numerical Results and Experiments

The first part of this section presents a validation of the numerical model in Section 2.5 that uses the quasi-static unfolding of a strip as a benchmark problem. The results from the numerical simulation are compared with the experimental data presented in Sec. 2.3.2. The second part of the section presents a comparison between the experimentally measured deployment behavior of the strips, with and without membrane, with the correspoding numerical simulations.

2.6.1 Model Validation

A quasi-static unfolding simulation of the strips was performed using the static implicit solver in Abaqus 2020. The boundary conditions matched the geometry and kinematics of the experimental setup described in Sec. 2.3.2. The simulation was structured in 4 steps. First, a small pressure load was applied to the flanges at the center of the longerons, in order to facilitate the formation of elastic folds, similarly to step 1 in Sec. 2.5.4. Then, the strip was folded to an angle $\theta = -35°$ by controlling the rotation of its ends. Next, the pressure load was removed and then the strip was unfolded by prescribing its end rotation. The deployment simulation showed that the strip undergoes several instabilities, because the elastic folds tend to move along the longerons, which makes convergence difficult to achieve. A small amount of viscous stabilization was introduced to help the solver achieve equilibrium and an analysis of the sensitivity to this parameter showed that a maximum allowable ratio of stabilization energy to total strain energy on the order of 10^{-7}, provides sufficient stabilization with negligible effect on the predicted moment in the strip. However, stabilization up to 10^{-4} was required in the final part of deployment, when snapping of the elastic folds releases significant amounts of energy.

The results are shown in Fig. 2.26 for the strip with and without membrane. Overall, the simulations are in good agreement with the experiments for large angles ($\theta > 10°$), correctly capturing the steady-state moment of the strip. For smaller

angles, the localized folds disappear and the simulations significantly overpredict the peak moment, which is over 2 times higher than the measured value for the strip without membrane, and 1.4 times higher for the strip with membrane.

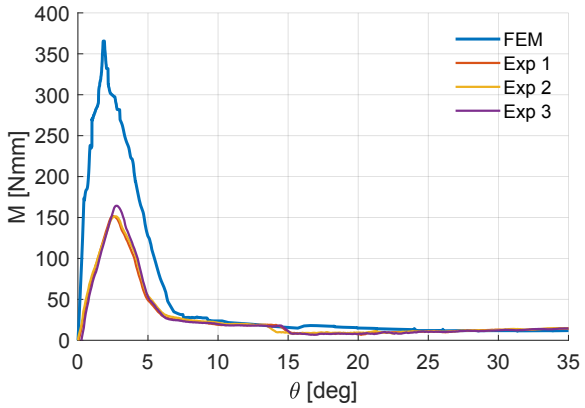

(a) Strip 1, without membrane

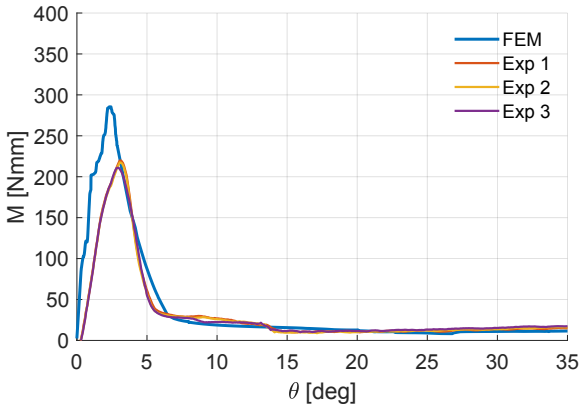

(b) Strip 2, with membrane

Figure 2.26: Comparison between simulations and experiments for quasi-static deployment.

There are two reasons for this discrepancy. First, as explained in Sec. 2.3.2, the experiments show that the localized folds transition from a symmetric to an asymmetric configuration for $\theta \approx 15°$. At the peak moment, the localized folds turn into local buckles along the compression flanges. As $|\theta|$ is decreased, the buckle's amplitudes gradually decrease as the applied rotation is reduced. The simulation misses this transition from symmetric to asymmetric folding, although it captures well the transition to local buckling of the compression flanges. Hence, it follows a higher-energy equilibrium path, which results in a higher peak moment.

This difference in behavior is not surprising, as thin-shell structures exhibit multiple

energetically-similar equilibrium paths [86], and the choice between different paths is very sensitive to small geometric imperfections in the structure. Therefore, since no imperfections were introduced in the simulation, the model follows the most symmetric equilibrium solution, which is not necessarily the lowest energy path. For the same reason, in the simulation the localized folds on the two longerons disappear at the same time, but in the experiment this only happens for the strip with the membrane. This explains why the error is smaller in this case. This result suggests that the coupling between the longerons introduced by the membrane might help making the structure less sensitive to imperfections, leading to a more deterministic and predictable behavior.

2.6.2 Comparison of Deployment Results

The results of the deployment simulations have been compared to the experiments on the two strips (with and without membrane), both in air and in vacuum. The plots in Figs. 2.27-2.29 present the evolution of the fold angle and the height of the center of the strip as a function of time.

Green and blue lines correspond to the experimental data for the two longerons; red lines represent simulations. Different runs of the same experiment are indicated by solid, dashed, and dotted lines.

Figure 2.27 shows the results for the strip without membrane. The simulation closely matches the experiments. The fold angle decreases symmetrically for both longerons, and hence only one angle has been plotted, and oscillates during the process. The amplitude and period of the oscillations are well captured by the simulation, and the deployment time is 4% slower than the mean deployment time from the experiments. When the fold angles become zero for the first time, latching of the longerons occurs and the strip starts vibrating. Figure 2.27b shows the evolution of the height of the center of the strip. The simulation and the experiments start from the same height (400 mm below the position of the pulleys), and match very closely for the initial 250 ms of deployment. After this time, the simulation becomes slightly faster than the experiment and reaches a 30 mm higher peak height.

Figures 2.28a and 2.28b show the results for a strip with membrane, deploying in vacuum. Again, there is very good agreement between simulation and experiments, with the predicted fold angle being within the envelope of experimentally measured angles, and the predicted deployment time being less than 5% slower than the mean experimental value. Regarding the height of the center of the strip, the simulation

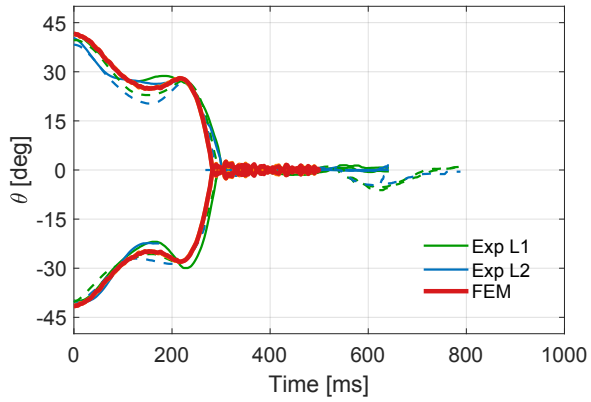

(a) Fold angles

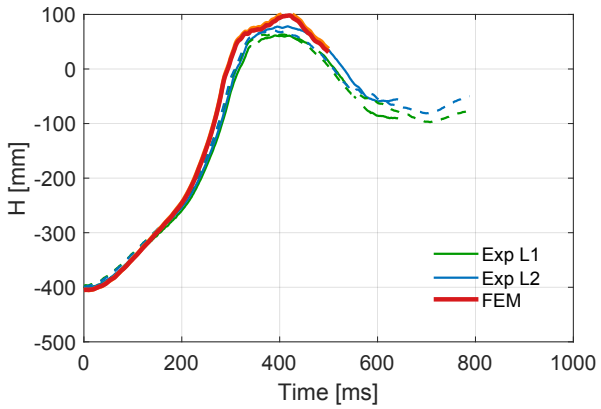

(b) Center height

Figure 2.27: Comparison between experiments in vacuum and simulations for a strip without membrane. Initial conditions: $H_0 = 400$ mm, $\lambda_0 = 0.45$, $M = 50$ g.

starts from the same value as the experiment, but becomes slightly slower after 150 ms, maintaining a 30 mm constant offset after this point. However, at the end of deployment, it reaches the same maximum height at approximately the same time.

Figures 2.29a and 2.29b present the results for a strip with membrane deploying in air. The simulation correctly captures the amplitude and period of the oscillation in the fold angle, as well as the deployment time. Because of the symmetry assumption in the finite element model, the two folds on each longeron disappear at the same time, whereas in the experiments there is a delay of 50 ms on average, possibly due to geometric imperfections and/or initial pre-stress in the Kapton membrane. A very good agreement is also found in the evolution of the height of the center of the strip (Fig. 2.29b), throughout the entire deployment process.

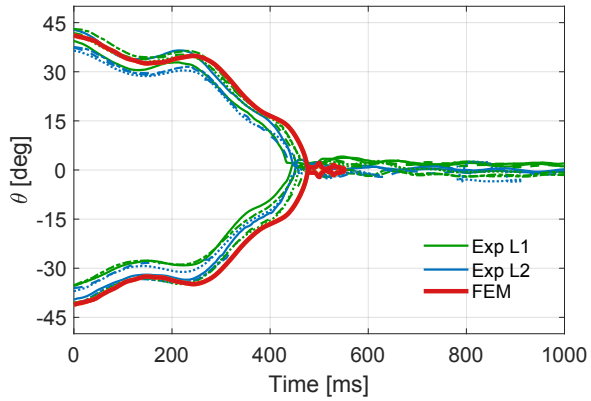

(a) Vacuum - Fold angles

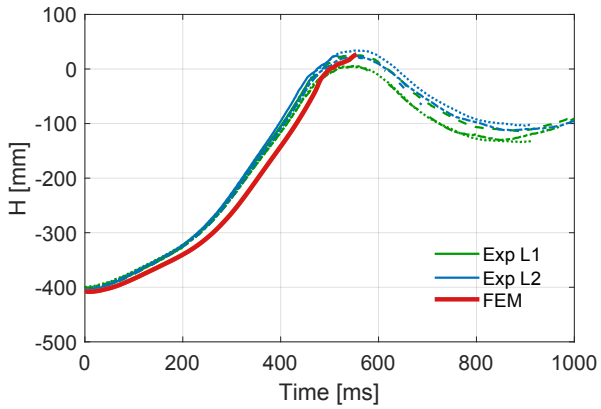

(b) Vacuum - Center height

Figure 2.28: Comparison between experiments and simulations for a strip with membrane. Initial conditions: $H_0 = 400$ mm, $\lambda_0 = 0.45$, $M = 50$ g.

2.7 Experimental Investigation of the Effect of the Initial Conditions on the Strip Deployment

The results presented so far assumed a fixed set of initial conditions ($H_0 = 250\ mm$, $\lambda_0 = 0.45$, and $M = 50$ g), representative of the behavior of the strips under a wider range of initial conditions. In this section, the experimental results that motivated this choice are presented. The experiments were carried out on the strip prototypes and with the experimental apparatus described in Sec. 2.3.

2.7.1 Design of Experiments

To explore the parameter space for the problem, 3 different values of initial heights H_0, 5 masses M, and 6 initial fold locations λ_0 were chosen for the experimental campaign from the suitable ranges defined in Sec. 2.2.3. Fig. 2.30 shows a map of all the combinations of initial conditions tested, for each strip prototype. The

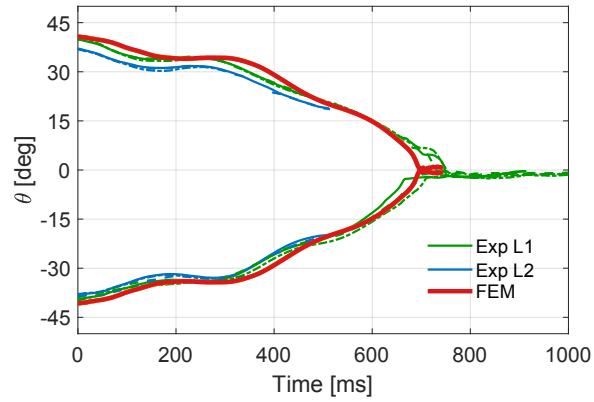

(a) Air - Fold angles

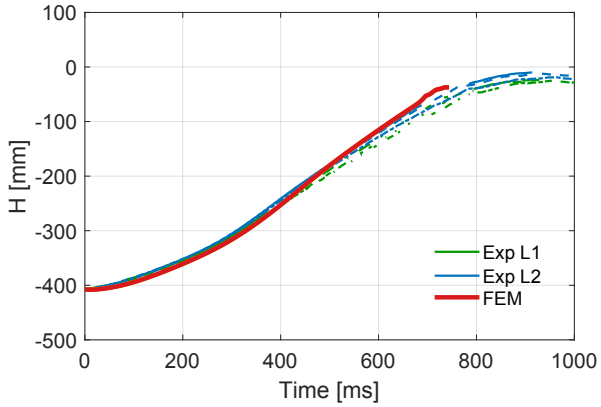

(b) Air - Center height

Figure 2.29: Comparison between experiments and simulations for a strip with membrane. Initial conditions: $H_0 = 400$ mm, $\lambda_0 = 0.45$, $M = 50$ g.

lowest mass of the counterweights was $M = 20$ g for the strip without membrane, and $M = 30$ g for the one with the membrane. The largest mass tested was limited to $M = 100$ g, to avoid damaging the strips due to bending of the terminal battens, to which the cords were attached.

The experimental results were processed using the algorithm described in Sec. 2.4, and the results were compared using 3 metrics:

- initial fold angle θ_0, defined as the mean absolute value of angle of the elastic folds in the strip (2 on each longeron) at the time $t = 0$;
- deployment time t_d, defined by the time at which all the elastic folds have latched for the first time (see Fig. 2.31a);

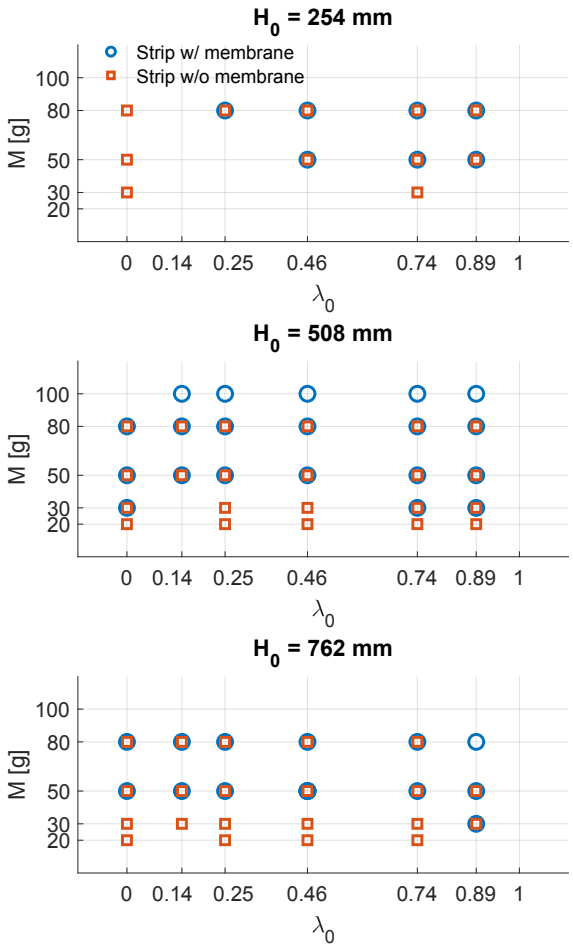

Figure 2.30: Combinations of initial condition for the strip deployment experiments.

- maximum fold propagation p_{max}, defined as the maximum distance traveled by an elastic fold during deployment. Its non-dimensional counterpart, $\Delta\lambda_{max} = \frac{p_{max}}{L}$, is defined in Fig. 2.31b.

The repeatability of the experiments was assessed by performing 3 runs for each combination of initial conditions and each strip. For each of the metrics y_i defined above, the maximum deviation across nominally identical runs of the j-th test case was computed as $\Delta y_{ij} = \max_{k=1,..3} y_{ij}^{(k)} - \min_{k=1,..3} y_{ij}^{(k)}$. The RMS of Δy_i was used as a measure of repeatability, and the results are summarized in Table 2.3. Note that, for $\Delta\theta_0$ and Δt_d, the percent variation is computed with respect to the mean value of each test case; for p_{max}, the half-length of the strip L is used instead.

The table shows that the experiments were very consistent for both strips, with the initial fold angles θ_0 and deployment time t_d being repeatable within 2% and 3% of their mean value, respectively. The maximum fold propagation p_{max} varied, on

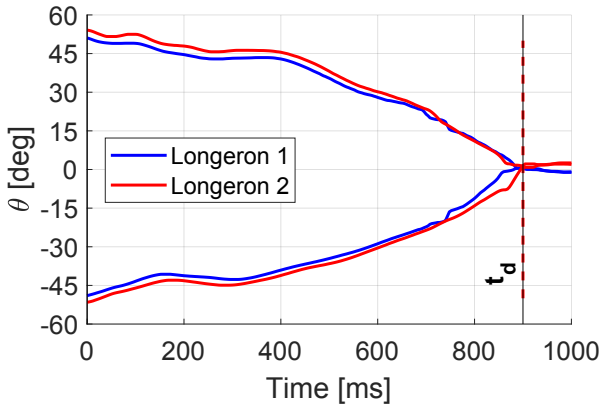

(a) Typical plot of fold angle vs time

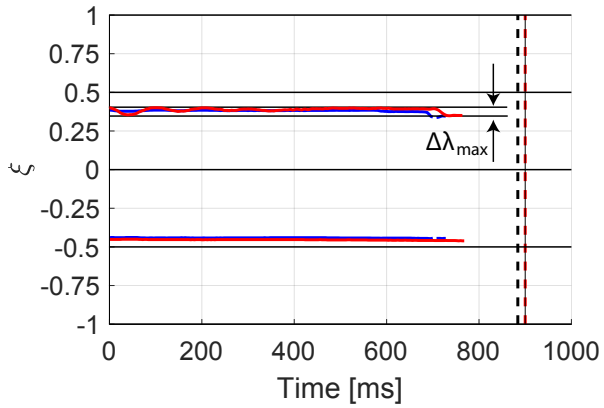

(b) Typical plot of fold location vs time

Figure 2.31: Definition of relevant metrics for the strip deployment experiments: deployment time t_d, initial fold angle θ_0, and maximum fold propagation $\Delta\lambda_{max}$. θ_0 is defined as the mean absolute value of the initial fold angle for the 4 folds.

	$\Delta\theta_0$	Δt_d	p_{max}
Strip w/o membrane	0.45° (1.2 %)	11 ms (2.6 %)	18.8 mm (3.3 %)
Strip with membrane	0.53° (1.4 %)	20 ms (2.6 %)	9.8 mm (1.7 %)

Table 2.3: Repeatability of deployment tests for strips with and without membrane.

average, by about 10 mm for the strip with membrane and 20 mm for the strip without membrane.

2.7.2 Experimental Results

The results for the strip without membrane are summarized in Fig. 2.32. The plots report initial fold angle θ_0, deployment time t_d, and maximum fold propagation p_{max} as a function of the initial fold location λ_0. Each marker corresponds to a

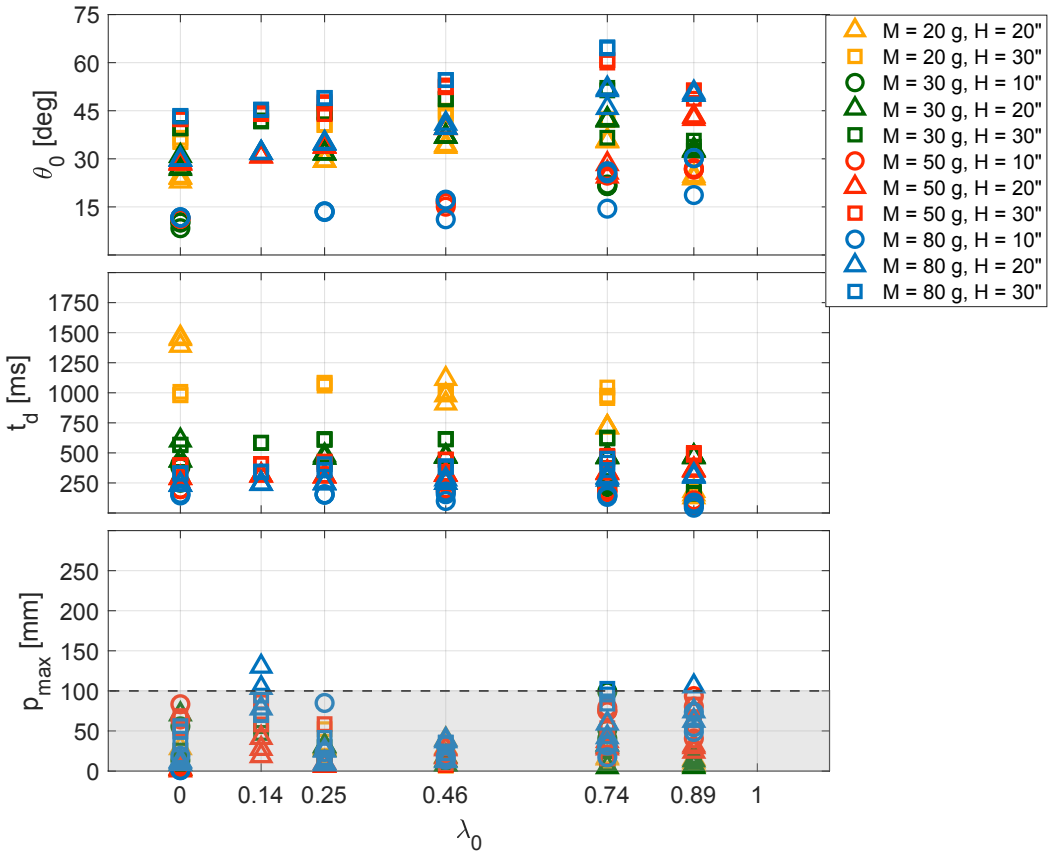

Figure 2.32: Results for strip without membrane.

different run of an experiment; different colors correspond to different masses of the counterweights M, and different marker shapes correspond to different initial heights H_0. The first plot from the top shows that, for given initial fold location, θ_0 increases with the initial height H_0, as well as with the mass M. For fixed M and H_0, the initial fold angle also increases as the folds move towards the ends of the strip. Using different combinations of M and H_0, it is possible to achieve initial fold angles between 10° and 65°, which are in agreement with the predictions from Fig. 2.10.

The middle plot in Fig. 2.32 shows that the deployment time t_d heavily depends on the mass of the counterweights M, ranging from about 1.5 s for a mass of $M = 20$ g, down to less than 200 ms for a mass of $M = 80$ g. Increasing the initial height H_0 also increases the deployment time, as the initial angle θ_0 becomes larger. However, for fixed M and H_0, the deployment time is mostly independent of the location of the folds.

Finally, the bottom plot in Fig. 2.32 shows that some propagation of the elastic folds can occur. However, in most cases, this propagation results from the folds oscillating about their initial position. To isolate experiments with a more interesting behavior, a threshold of $\overline{p}_{max} = 100$ mm was chosen (dashed horizontal line in the plot). The experiments with $p_{max} > \overline{p}_{max}$ correspond to configurations with the folds close either to the center of the strip ($\lambda_0 = 0.14$) or to its ends ($\lambda_0 > 0.74$). In the next section, these two regimes will discussed in more detail.

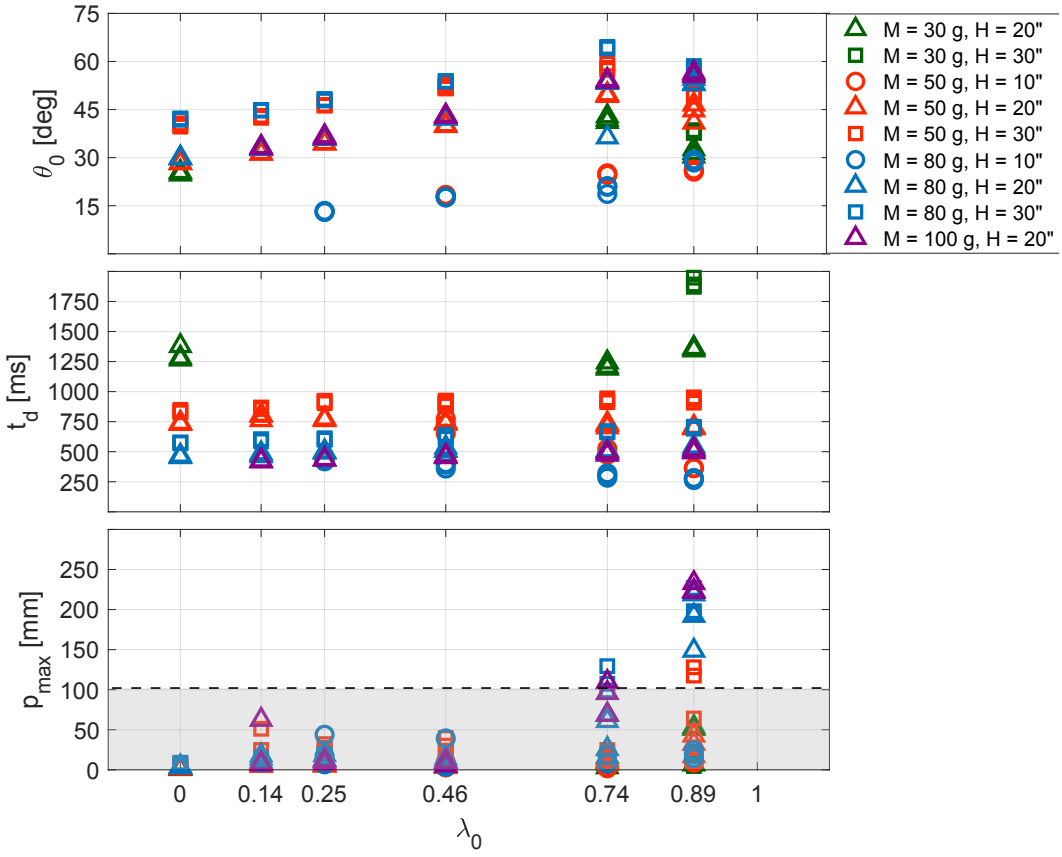

Figure 2.33: Results for strip with membrane.

Fig. 2.33 shows the results from the experiments on the strip with membrane. The top plot confirms the dependency of θ_0 on the initial conditions, already discussed for the previous case. The middle plot shows the same qualitative behavior as the strip without membrane. However, for the same initial conditions, the deployment time for the strip with membrane is approximately twice the time for the other strip. This is consistent with the higher inertia and weight of the strip, due to the presence of the membrane. The bottom plot in Fig.2.33 shows some differences between

the two strips in the maximum fold propagation. Specifically, for the strip with membrane, the propagation is more pronounced when the folds are close to the ends of the strip, where they can propagate for up to a 1/4 of the total length of the strip. On the other end, no propagation occurs when the folds are close to the center of the strip, unlike the strip without membrane.

2.7.3 Special Cases of Propagation of the Elastic Folds

This section focuses on the propagation of the elastic folds during deployment of the strip prototypes, for certain combinations of initial conditions. In particular, two regimes can be identified, with qualitatively different behavior: folds close to the center of the strip, and folds close to its ends. A schematic of the folded strip for the 2 cases is shown in Fig. 2.34.

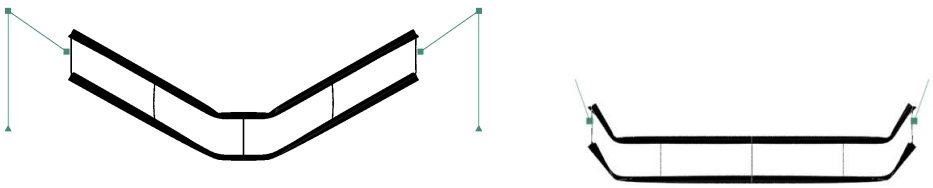

(a) Folds close to the center of the strip (λ = 0.14)

(b) Folds close to the ends of the strip (λ = 0.91)

Figure 2.34: Special configurations of a folded strip for which fold propagation can occur.

Fig. 2.35 shows fold angle and fold location for the strip without membrane, with initial conditions M = 80 g, H_0 = 508 mm, and λ_0 = 0.14. During deployment, the fold angle θ remained mostly symmetric, starting from an initial value of about 30° and fully deploying after 244 ms (Fig. 2.35a). However, shortly after the release of the strip, one of the folds on each longeron propagated towards the other fold, merging with it after 36 ms and 48 ms, for the 2 longerons. Soon after this (at t = 72 ms and t = 56 ms, respectively), the remaining fold moved to the center of the strip, without propagating further until the end of deployment.

The other 2 runs of the same experiment showed the same qualitative behavior, with the folds always merging and moving to the center of the strip. However, the order in which the events occurred varied, and the folds would sometimes move to the center of the strip and merge there, rather than creating the asymmetric configuration

shown in Fig. 2.35b.

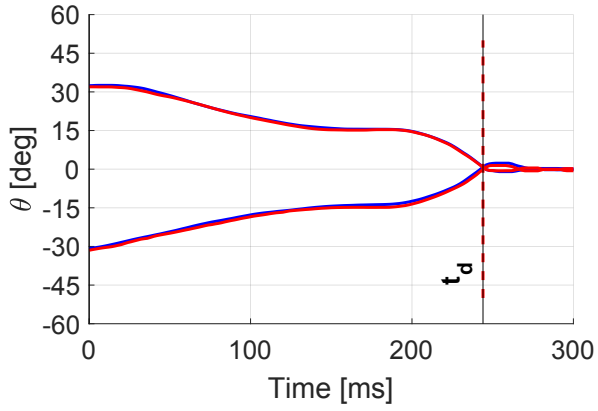

(a)

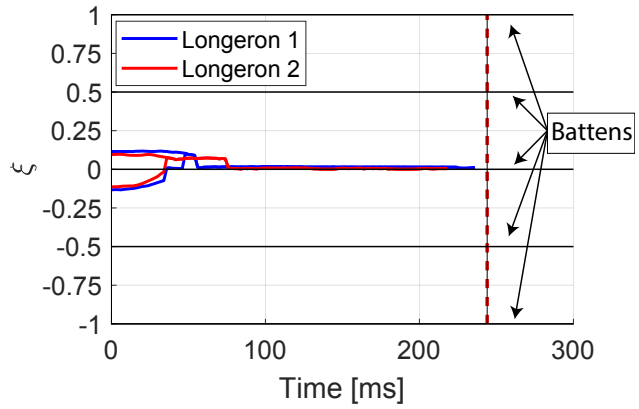

(b)

Figure 2.35: Propagation of the elastic folds in the strip without membrane, for M = 80 g, H_0 = 20", and λ_0 = 0.14.

Fig. 2.36 shows an example of propagation of the folds for the strip with membrane, with initial conditions M = 100 g, H_0 = 508 mm, and λ_0 = 0.91. In this case, the strip deployed from an initial angle $\theta_0 \approx 55°$, and the longerons reached their deployed state at about the same time, after 516 ms. Fig. 2.36b shows that, in this case, 3 of the 4 folds propagated towards the center of the strip, whereas the fourth one remained stationary. The rate of propagation of the folds is approximately the same, although one of the them stopped at ξ = 0.67, while the others propagated until reaching $\xi = \pm 0.5$, which, interestingly, corresponds to the location of the second and fourth battens in the strip. Despite some variability in the extent of the fold propagation and the order of propagation, other runs of the same experiment and different experiments with folds close to the ends share the following qualitative traits:

- the folds never propagate past the location of the battens;
- one of the 4 localized folds does not propagate, resulting in a non-symmetric deployment process.

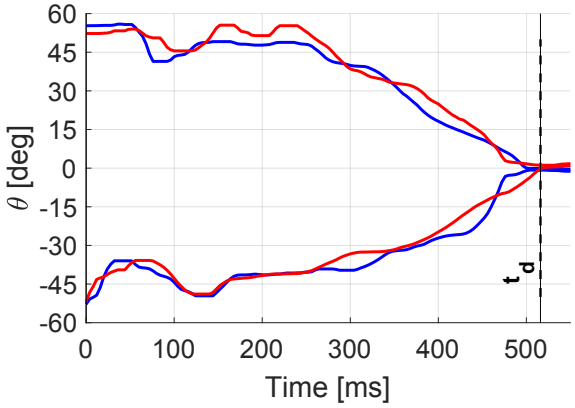

(a)

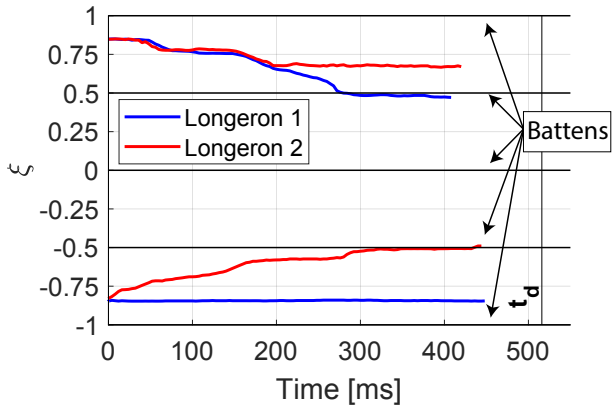

(b)

Figure 2.36: Propagation of the folds in the strip with membrane, for $M = 100$ g, $H_0 = 20$", and $\lambda_0 = 0.91$.

The first point can be explained in terms of a local stiffening effect of the battens, which are connected to the flange of the longerons by glass fiber Ω-shaped connectors. The additional bending stiffness introduced by the connectors likely creates an energy barrier that stops the propagation of the folds. Although definitive proof of this mechanism has not been presented yet, the results in this section hint at a potential way to passively control the propagation of the elastic folds by artificially stiffening the longerons at opportune locations.

The second point mentioned above, i.e. the strip locking in a non-symmetric configuration with only a stationary fold, is not understood yet. However, the fact that it is more pronounced in the strip with the membrane than in the other strip suggests that this could be an artifact of the shear constraints introduced by the membrane. Similarly, this coupling between longerons might explain why, in the strip with membrane, the fold merging mechanism at small λ_0 (presented in Fig. 2.35) was never observed.

2.7.4 Discussion

The experimental campaign presented in this section showed that, for most combinations of initial conditions, the strips exhibit the same qualitative behavior, with the folds remaining stationary and the overall deployment being mostly symmetric.

There are few instances, discussed in the previous section, in which the symmetry of the deployment is broken and the elastic folds propagate. While this behavior is interesting and can shed some light on the interaction between different components of the space structure, it only occurs in extreme cases, where the folds are very close to each other or to the ends of the strip. Such cases are of limited practical interest and, therefore, were not be investigated further in this thesis.

An intuitive way of packaging a strip by using two elastic folds would be to divide it in 3 parts of equal length (corresponding to $\lambda_0 = 0.33$), so that the two end portions would lie on top of each other when folded (see Fig. 2.3). Alternatively, $\lambda_0 = 0.5$ would result in a larger central panel and two side panels with half its length, as shown in Fig. 2.1b; in this case, the side panels would not overlap when folded. Based on these considerations, the intermediate value of $\lambda_0 = 0.45$ was chosen as a reference for the strip deployment study in Chapter 2. The intermediate value of initial height $H_0 = 508$ mm (20") was selected because it provides a relatively large initial fold angle ($\theta_0 \approx 45°$) without sacrificing the quality of the DIC measurements. Greater heights, indeed, make it difficult to track the entire strip throughout the its range of motion due to the large out-of-plane displacements, often resulting in partial and/or noisy data.

Finally, regarding the mass of the counterweights, the experiments showed that a mass of $M = 30$ **g** would be the minimum to effectively support either strip prototype. However, the resulting deployment would have been quite slow (longer than 1 s), which would have made it difficult to capture dynamic effects, such as the interaction with air. On the other hand, large masses (between 80 g and 100 g) would

result in a much faster deployment, but the dynamics of the structure might have been dominated by the suspension system. Therefore, $M = 50$ g was chosen for the final experiments, as it provides a good compromise between those conflicting considerations.

2.8 Conclusion

This chapter has presented a study of the dynamic deployment of rectangular space frames composed of interconnected, ultralight thin-shell longerons. The structures were initially folded by forming two elastic folds, and were then deployed by releasing the stored elastic energy. An experimental setup was designed to symmetrically fold 1.125-m-long structural prototypes, which were supported by a cord suspension system and deployed against gravity with the assistance of two edge masses. Digital Image Correlation was used to measure the deformation of the structure during deployment, and an algorithm was developed to track the location and angle of the elastic folds, robust against noisy and incomplete point clouds. The algorithm, implemented in MATLAB, can be easily adapted to different shell geometries and to point clouds obtained from different measurement techniques, and is available to the interested reader at the following link `https://github.com/apedivel/thin_shell_localized_folds.git`.

Deployment experiments have shown that a symmetrically folded structure remains essentially symmetric during the deployment process. For the particular experiments presented in the chapter, the elastic folds did not move along the longerons, behaving as non-linear elastic hinges. In other experiments, with different initial locations for the elastic folds (very close to the center or to the ends of the strips) and not presented in this chapter, the folds did move, although they were often constrained by the battens to remain within one bay of the structure.

The present simulation method can be used to predict the effects of different loading and boundary conditions on the deployment of the structure, which can be significant. For example, Fig. 2.37 compares the evolution of the elastic folds $\theta(s)$ for the strip without membrane, if the end masses are replaced with constant force retractors. This plot shows that free deployment in 0 g would be almost twice as fast as the benchmark case studied in this chapter (deployment with gravity and suspension system with 50-g end masses), with a deployment time of 144 ms vs. 282 ms. Also, the angle of the folds monotonically decreases during free deployment, whereas it oscillates in the final part of deployment for the benchmark case. The oscillation

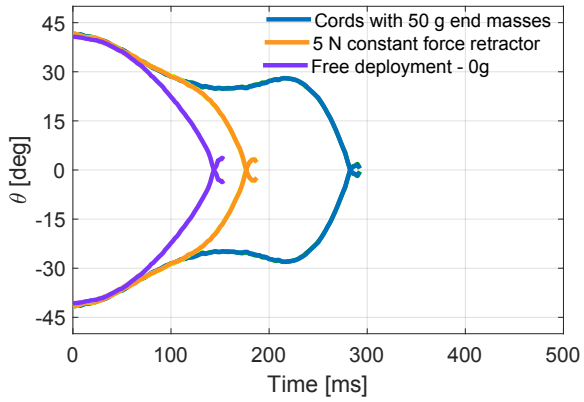

Figure 2.37: Effect of boundary conditions and gravity on the deployment of a strip.

in the fold angle is due to the inertia of the end masses. This was confirmed by simulating a variant of the suspension system, where the counterweights are replaced by a constant force spring retractor with negligible inertia, providing the same amount of cord tension (5 N) as the benchmark suspension system. The results for this case (yellow lines in Fig. 2.37) show that the fold angle is the same as the suspension system with counterweights for the first 110 ms of deployment, but it decreases much faster afterwards and remains monotonic. The deployment time for this case is 175 ms, only 20% slower than free deployment in 0 g.

These results indicate that, although the suspension system presented in this chapter offers a relatively simple implementation and can be accurately characterized experimentally and modeled in simulations, alternative suspension concepts may be devised that provide a closer approximation to deployment under zero-g conditions.

The effect of air on the deployment dynamics of these structures has been experimentally characterized for the first time. It has been shown that the interaction with air significantly slows down the deployment of a strip prototype supporting a thin membrane. However, this effect becomes negligible in the absence of the membrane.

A finite element model of deployment has been developed. Quasi-static deployment simulations were able to correctly predict the steady-state moment of the strip prototypes, but significantly overpredicted the peak moment at the end of deployment. This discrepancy was attributed to the longerons being sensitive to geometric imperfections, such as local variations of the flange radius and angle. Such imperfections were not considered in this chapter, and require further work to be experimentally characterized and included in simulations. As far as the dynamic deployment sim-

ulations are concerned, they correctly capture the initial equilibrium configuration in the folded state, and accurately predict the evolution of the fold angles during deployment, with less than 5 % error on the deployment time. A simple model to estimate the added mass of air from the geometry of the structure, as well as an air drag model based on drag coefficients from literature, has been proposed. Simulations made with this model closely match the deployment behavior observed in experiments, both qualitatively and quantitatively. Although the present study has considered initial folding angles of about 45°, it would be interesting to investigate the deployment of fully folded strips, which would require a different suspension system.

In conclusion, it has been shown that the packaging and deployment of space frames consisting of thin-shell longerons can self-deploy in a reliable and repeatable fashion. This represents a promising path forward to the application of thin-shell technologies to novel lightweight solar array concepts and other applications.

Chapter 3

PACKAGING AND DEPLOYMENT KINEMATICS OF A THIN-SHELL SPACE STRUCTURE

Parts of this chapter were modified from the following publication:

[1] Eleftherios Gdoutos, Alan Truong, Antonio Pedivellano, Fabien Royer, and Sergio Pellegrino (2020). "Ultralight deployable space structure prototype". In: *AIAA Scitech 2020 Forum*. 2020-0692.

[2] Antonio Pedivellano, Eleftherios Gdoutos, and Sergio Pellegrino (2020). "Sequentially controlled dynamic deployment of ultra-thin shell structures". In: *AIAA Scitech 2020 Forum*. 2020-0690.

3.1 Introduction

Thin-shell strips offer a simple architecture to build bending-stiff planar structures using the one-dimensional packaging concepts established for deployable booms. In Chapter 2, a folding scheme was proposed to deploy a strip under its own strain energy, only requiring a simple release mechanism to hold down the structure during launch and initiate deployment once in space. This solution is well-suited for small scale applications (< 1 m^2), for which simplicity and cost effectiveness are prioritized. As the size of the structure increases, a larger number of elastic folds would be needed, resulting in a complex deployment dynamics. In this case, coilable strips offer a more efficient and scalable solution, of which the Roll-Out Solar Array (ROSA) [38] represents the best example demonstrated in space so far. Strip architectures up to 100 m^2-area have been proposed [65], based on the ROSA concept. Larger structures can be achieved by stacking multiple independent strip units side by side, like in the MEGA-ROSA concept [65]. However, each of these strips would require its own deployment mechanism, increasing complexity and stowed volume of the structure. An alternative approach would be to build a continuous structure that extends in two directions and is deployed by a single deployment mechanism. In this case, bi-axial compaction is required to achieve efficient packaging.

In this chapter, a square space frame architecture, composed of interconnected thin-shell strips, is presented. Its kirigami-inspired packaging scheme was first proposed by Arya et al. [4], and consists of a combination of folding and coiling techniques.

While this concept has been previously demonstrated on membranes, in this chapter we apply it to an actual thin-shell structure, and we propose the following objectives:

- Design a systematic and repeatable folding procedure to package the structure;
- Develop a deployment mechanism to achieve controlled and robust coiling/uncoiling of the structure;
- Devise a strain-energy deployment scheme to deploy structures with a large number of thin-shell components in a predictable and reliable fashion.

In the next section, the architecture of the space structure and its packaging scheme are introduced. The challenges with the implementation of this concept are discussed, and the layout of the chapter is presented.

3.2 Background

Multiple architectures and packaging schemes for planar structures have been developed in the context of deployable membranes, such as solar arrays, reflectors, and drag sails. Architecture studies by the European Space Agency (ESA) suggest that square architectures, supported by 4 diagonal booms, offer the best compromise in terms of deployability, complexity, and maneuverability [58].

Several solar sails have been flown based on this architecture: the Lightsail-1 mission [8] demonstrated a 32 m^2 membrane, composed of 4 triangular quadrants, each folded in two directions using a map folding scheme [81], as shown in Fig. 3.1b. The same concept was used on De-orbit Sail [97], a 25 m^2 drag sail flown in 2014. A different packaging scheme is used for NEA Scout [62], a NASA mission featuring a 85 m^2 solar sail, set to launch in November 2021. In this case, the membrane is Z-folded along one direction to become a rectangular strip, and then spooled about 2 cylinders to reach its stowed configuration (see Fig. 3.1a).

An alternative folding scheme for a square structure consists of creasing concentric squares in alternating directions (mountain and valley folds), and adding 4 diagonal valley folds. This crease pattern is known in the origami community as a pleated hyperbolic paraboloid (or hypar), due to its natural tendency to form a saddle shape. Demaine et al. [13] studied the kinematic compatibility of this folding pattern with an ideal surface [12]; Seffen [91] developed an analytical model to predict the shape of the structure for applications in compliant mechanisms and morphing structures. In the field of deployable structures, the hypar folding scheme was applied in the

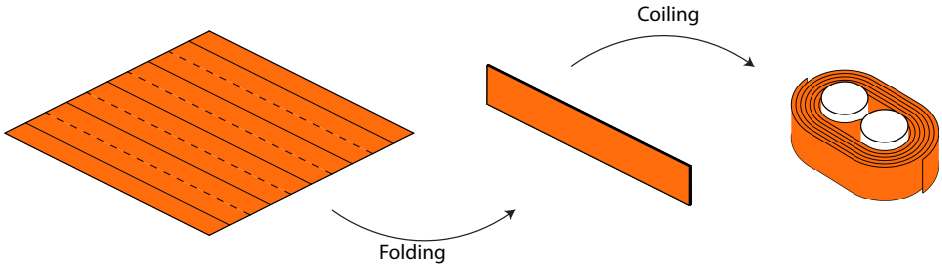

(a) Packaging of a square/rectangular structure by Z-folding in one direction, then coiling around 2 cylinders

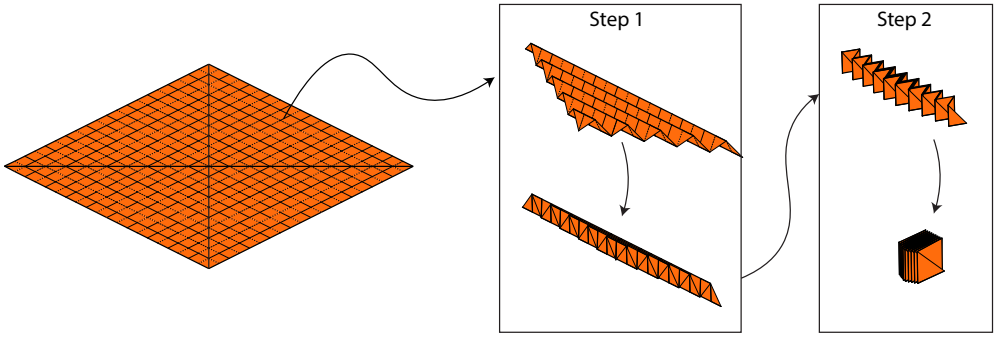

(b) Packaging of a square structure made of disconnected triangular quadrants: each quadrant is Z-folded in both directions like a map

Figure 3.1: Examples of bi-directional compaction schemes for large area membranes.

late 1980s to fold thin membranes deployed by centrifugal forces [52], during the experimental campaign leading to the Znamya-2 mission, the first large reflector demonstrated in space, in 1993. In this context, circular membranes were folded with 2-fold, 4-fold, and 6-fold symmetry, and the ends of the folded star were coiled about a large central hub. This study concluded that 4-fold symmetric structures provide better deployment performances than 2-fold symmetric structures. More recently, this symmetric scheme has been demonstrated on space webs (spin-stabilized cable nets to support large structures) [27] and membranes, with the IKAROS mission [74]. In both cases, a 2-step deployment scheme was used, in which the structure first uncoiled its 4 arms to achieve a star shape, then it unfolded into its planar deployed state.

Most solar sails consist of a continuous sheet or continuous triangular segments. However, stripped architectures have also been considered, in which each segment is composed of trapezoidal strips, each connected to the diagonal booms [60][17][19].

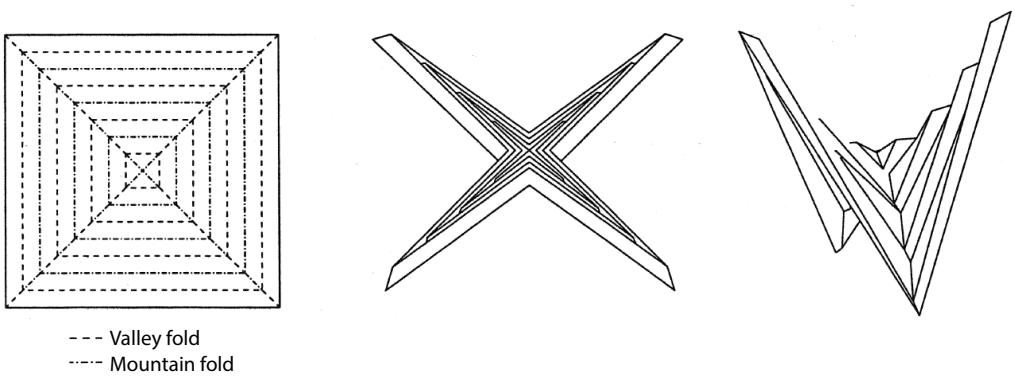

Figure 3.2: Origami pattern for a square structure. Releasing the folds generates an hyperbolic paraboloid (hypar). When fully folded, the square is reduced to a star shape. Image modified from [13].

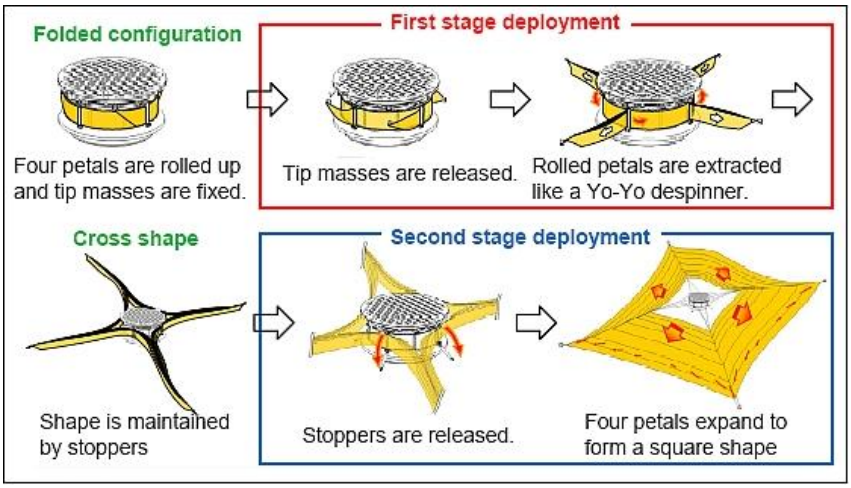

Figure 3.3: Deployment scheme of IKAROS [74]: the solar sail is deployed and stabilized by centrifugal forces applied by tip masses.

Greschik and Mikulas [31] suggested that such design makes it easier to compute stresses in the structure, as each strip is essentially subject to uniaxial loading. Also, the compressive and shear loads applied to the booms are distributed, rather than being applied at the tips as in other designs, thus allowing for smaller and lighter booms. A stripped design is also beneficial when used in combination with packaging concepts involving folding and coiling the structure, such as the ones in Figs. 3.1a and 3.3. Arya et al.[5] showed that, due to their finite thickness, stacked strips need to axially slide with respect to each other during coiling. Continuous sails prevent this motion, leading to wrinkles. Therefore, they proposed a concept of "slipping folds," consisting of introducing cuts along the creases of the membrane,

effectively resulting in a stripped design. A 4-fold symmetric structure based on this concept was proposed for the Space Solar Power Project at Caltech [4]. The novelty of this architecture was the use of thin-shell components to create bending-stiff strips, capable of achieving the shape accuracy needed for a space solar power application. The structural architecture and its packaging concept are presented in more detail in the next section.

3.3 Architecture and Packaging Concept

The space structure architecture is shown in Fig. 3.4. It is composed of 4 triangular quadrants, each containing several trapezoidal strips [85], connected by diagonal cords. Each strip includes 2 deployable longerons based on the triangular, rollable, and collapsible (TRAC) architecture [75], connected by transverse and diagonal rods (battens), supporting functional elements for a satellite [29][35]. Two rigid joints placed on the diagonal battens connect the strips to the diagonal cords, allowing rotations about the cord axis and preventing axial displacements [103].

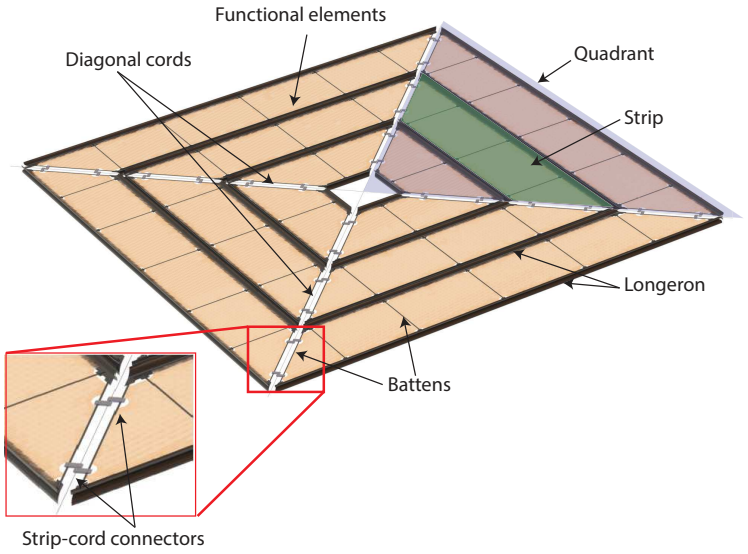

Figure 3.4: Architecture of a space structure that can be packaged two-dimensionally. Each quarter of the structure contains 3 trapezoidal strips (in this example); 4 adjacent identical strips constitute a square. Each strip includes 2 longerons, connected at the ends by diagonal battens. A variable number of transverse battens connect the longerons inside the strip. The strips are supported by diagonal cords via strip-cord connectors, placed on the diagonal battens. A flexible sheet covers the interior of each strip and simulates functional elements of the spacecraft.

The structure is packaged by first z-folding each quadrant (Fig. 3.5, A to C) and then coiling each arm of the resulting star-shape into a cylindrical shape (Fig.3.5,

C to E). A key aspect of this scheme is that, because of the 4-fold symmetry of the structure, z-folding the strips also requires bending the longerons. As it will be discussed later on, this aspect has important consequences on the deployment behavior of the structure.

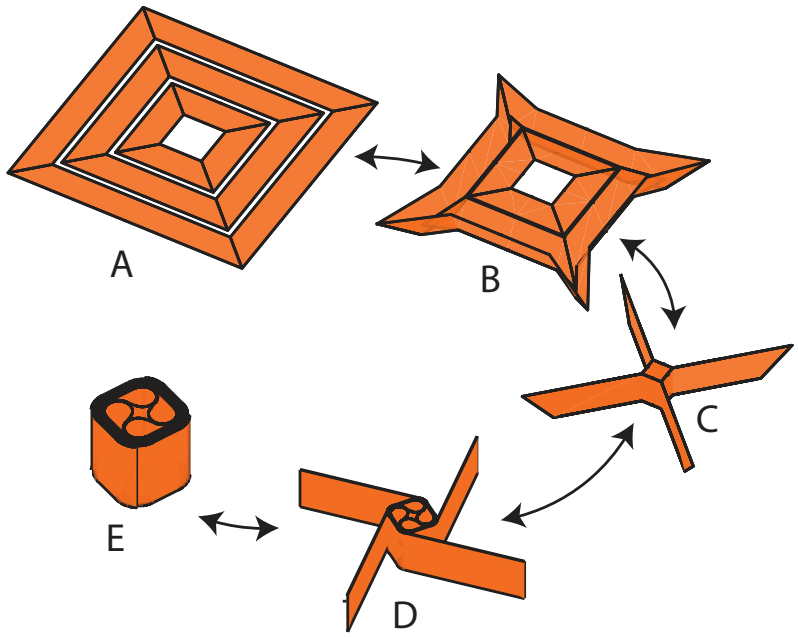

Figure 3.5: Packaging concept for a space solar power satellite.

The packaging concept described here is inspired by the "hypar" origami-scheme presented in Fig. 3.2. Arya et al. [4] converted this concept in kirigami by adding slipping folds, i.e. longitudinal cuts along the crease line that allow for relative sliding between strips, required to package membranes of finite thickness. To extend this packaging concept to thin-shell space structures, it is necessary to take into consideration their mechanical response. During folding, they oppose bending deformations and tend to form localized folds in unpredictable locations. This can potentially induce excessive stress and damage other structural components, such as the battens and their joints to the longerons. During coiling, thin-shell structures store strain energy and tend to release it by self-deploying, or by deviating from their nominal cylindrical shape. Coiling instabilities, such as local buckling or blossoming, have the potential of damaging the payload on the structure by imposing higher curvature than intended, or jamming the deployment mechanism.

Solving these challenges is the main objective of this chapter. First, a packaging

procedure is proposed to star-fold the space structure in a predictable and controllable way. The underlying idea is to exploit the nonlinear mechanics of the shells to impose localized folds at opportune locations, so that each strip would essentially behave as an assembly of rigid panels connected by hinges. This allows study of the kinematics of the structure using established tools for rigid spatial mechanisms. Therefore, a kinematic model of the structure is developed to identify admissible kinematic paths between the initial, planar configuration and the folded state. It is shown that, under certain circumstances, this kinematic path is unique, therefore allowing for a predictable folding sequence. The interaction between multiple square loops in the structure is also considered, to develop a folding procedure for a space structure with a general number of strips.

The second part of the chapter addresses the problem of coiling the structure from the star shape to its fully-packaged cylindrical state. A concept of pressure stabilization is proposed to support and constrain the structure during packaging, launch, and deployment. The concepts presented herein are demonstrated on a 1.7 m $\times$ 1.7 m space structure, which is folded according to the proposed procedure, and coiled with a deployment mechanism prototype based on the pressure stabilization concept.

Finally, a staged deployment scheme is demonstrated, in which the structure unfolds from the star shape to its deployed planar state by dynamically deploying between intermediate, known configurations. Such configurations are achieved by imposing folds at desired locations using releasable constraints, to help the structure follow a set kinematic path. By breaking down the deployment process in multiple small steps, this approach can reduce the uncertainty associated with the dynamic deployment of large structures composed of many thin-shell components, and mitigate the risk of incomplete deployment.

3.4 Kinematic Model Formulation

This section focuses on the design of a packaging procedure to fold a space structure consisting of multiple, interconnected, thin-shell strips. The approach developed herein exploits the nonlinear mechanical behavior of thin-shell components, in particular their propensity to form elastic folds, to package the structure in a safe and predictable way. Specifically, by imposing elastic folds at opportune locations, the structure can be modeled as a kinematic chain consisting of rigid links connected by revolute joints. This allows us to extend the use of established mathematical tools for rigid spatial mechanisms to thin-shell space structures. In particular, this section

derives a kinematic model for closed-loop kinematic chains, for which loop closure conditions are formulated to identify compatible kinematic paths. This method has been previously proposed by Gan and Pellegrino [25] to model one degree-of-freedom mechanisms and identify bifurcation points along their kinematic path. In this section, it is used to model a square loop consisting of 4 strips, each containing two elastic folds, and it is applied to cases with single and multiple degrees of freedom.

3.4.1 Loop-Closure Equations

Let us consider a linkage consisting of rigid, straight links connected by revolute joints. A local reference frame can be assigned to each link (see Fig. 3.6a), with the origin at one of its ends, the z-axis aligned with the axis of the hinge, the x-axis lying in the plane defined by the z-axis and the axis of the link, and the y-axis chosen to form a right-handed reference frame. Transformations between frames can be expressed in terms of a translation vector v and a rotation matrix R, with can be combined in a compact form using the Denavit-Hartenberg notation, often used in standard textbooks [104]:

$$T_i = \begin{bmatrix} R_i & v_i \\ 0_{1\times 3} & 1 \end{bmatrix} \tag{3.1}$$

In this notation, the 3D coordinates of a generic point $\tilde{P}$ are written as a 4×1 extended vector:

$$P = \begin{bmatrix} \tilde{P} \\ 1 \end{bmatrix} \tag{3.2}$$

Its coordinates P_{i+1} in the $(i+1)$-th frame can be expressed in the i-th frame by means of the following expression:

$$P_i = T_i P_{i+1} \tag{3.3}$$

The rotation matrices are defined in terms of 3 Euler angles, obtained from a sequence of elementary transformations to align the i-th reference frames with the $(i+1)$-th frame. The convention used in this model is the following:

1. translation v_i of the coordinate system from O_i to O_{i+1} (Fig. 3.6b);
2. rotation about the y_i axis by ϕ_i, until the rotated z_i'-axis is contained in the $y_i - z_{i+1}$ plane (Fig. 3.6c);
3. rotation about the new x_i' axis by ξ_i, until the rotated z_i'' axis is aligned with z_{i+1} (Fig. 3.6d);

4. rotation about the $z_i'' = z_{i+1}$ axis by β_i, until x_i''' is aligned with x_{i+1} (Fig. 3.6e).

With this convention, ϕ is the angle between the hinge axis and the normal to the link axis; ξ is the twisting angle between the ends of the rod, and β is the fold angle, i.e. the rotation about the hinge axis.

By combining the 3 elementary rotations (R_x, R_y, R_z), the full rotation matrix can be obtained:

$$R = R_y R_x R_z = \begin{bmatrix} \cos\phi & 0 & -\sin\phi \\ 0 & 1 & 0 \\ \sin\phi & 0 & \cos\phi \end{bmatrix} \begin{bmatrix} 1 & 0 & 0 \\ 0 & \cos\xi & -\sin\xi \\ 0 & \sin\xi & \cos\xi \end{bmatrix} \begin{bmatrix} \cos\beta & -\sin\beta & 0 \\ \sin\beta & \cos\beta & 0 \\ 0 & 0 & 1 \end{bmatrix}$$
$$\begin{bmatrix} \cos\phi\cos\beta + \sin\beta\sin\phi\sin\xi & \cos\beta\sin\phi\sin\xi - \cos\phi\sin\beta & \cos\xi\sin\phi \\ \cos\xi\sin\beta & \cos\xi\cos\beta & -\sin\xi \\ \cos\phi\sin\xi\cos\beta - \cos\beta\sin\phi & \cos\phi\cos\beta\sin\xi + \sin\phi\sin\beta & \cos\phi\cos\xi \end{bmatrix} \tag{3.4}$$

Coordinate transformations between non-consecutive links can be obtained by multiplying the transformation matrices of all the links between the first and last joint in the sequence, as follows:

$$T_1^n = T_1 T_2 ... T_{n-1} \tag{3.5}$$

For a closed-loop kinematic chain, the initial and final frames must coincide. Hence, the corresponding transformation becomes:

$$T_1\ T_2 ... T_{n-1} T_n = I_{4\times4} \tag{3.6}$$

This matrix equation formulates the loop-closure constraints. Although it contains 16 scalar equations, only 6 of them are linearly independent (corresponding to 3 rotations and 3 translations, necessary to fully define a coordinate transformation).

By solving this system of trigonometric equations, it is possible to identify compatible kinematic paths for a structure. Closed-form solutions are possible for simple cases, but their complexity rapidly increases with the number of elements in the linkage, requiring a numerical approach. Even so, due to the existence of multiple kinematically-compatible configurations, nonlinear numerical solvers are highly sensitive to the initial guess, and do not provide any information as to whether two different admissible configurations belong to the same kinematic path or are disconnected. To address these challenges, Gan and Pellegrino [25] proposed an incremental solution capable of following the kinematics of one degree-of-freedom mechanisms and identifying bifurcation points along this path.

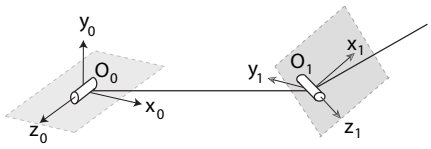

(a) Local reference frames for two adjacent rods in a linkage

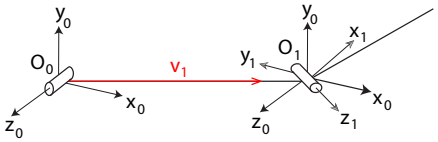

(b) Translation v_1 of the frame $x_0y_0z_0$ to the origin of the frame $x_1y_1z_1$

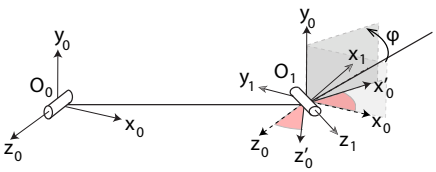

(c) Rotation ϕ about the y_0-axis, such that z_0' lies in the $y_0 - z_1$ plane

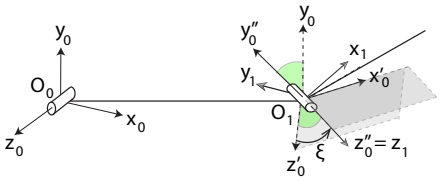

(d) Rotation ξ about x_0' to align z_0'' with z_1

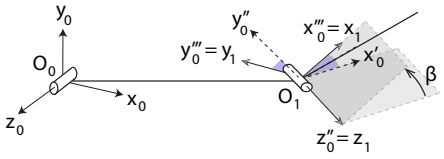

(e) Rotation β about z_0'' to align x_0''' with x_1

Figure 3.6: Elementary coordinate transformations between local reference frames on adjacent links connected by an hinge.

3.4.2 Linearized Kinematics

The incremental solution is based on a two-step algorithm: in the predictor step, the loop-closure equations are linearized to find kinematically-admissible directions and compute an increment of the solution; in the corrector step, corrections to the linear prediction are computed iteratively until the error resulting from the linearization of the nonlinear equations becomes smaller than a threshold. These steps are described in detail in the next subsections.

3.4.2.1 Predictor Step

The predictor step requires a starting configuration x_i, for which the loop-closure equation is satisfied:

$$T_1(x_i)\, T_2(x_i)..T_{n-1}(x_i)\, T_n(x_i) = I_{4\times4} \tag{3.7}$$

Adding a small increment Δx changes the transformation matrices, each of which can be expanded as a Taylor series:

$$T_k(x_i + \Delta x) = T_k(x_i) + T_{k,j}\big|_{x=x_i} \Delta x_j + O(\Delta x^2) \tag{3.8}$$

Here, the index i refers to increments of the solution, j to components of the state vector x, and k to joints in the kinematic chain. Note that the Einstein summation convention is used, and partial derivatives are expressed as $T_{i,j} = \frac{\partial T_i}{\partial x_j}$, for brevity of notation. Substituting the Taylor expansions of the transformation matrices in the loop-closure equation and keeping only the linear terms in Δx_j, the following result holds:

$$\begin{aligned}
&T_1(x_i)\ T_2(x_i)..T_{n-1}(x_i)\ T_n(x_i)+ \\
&\quad + \left(T_{1,j}\big|_{x=x_i}\ T_2(x_i)...T_{n-1}(x_i)\ T_n(x_i)+\right. \\
&\quad + T_1(x_i)\ \ T_{2,j}\big|_{x=x_i} ...T_{n-1}(x_i)\ T_n(x_i)+ \\
&\quad + T_1(x_i)\ T_2(x_i)...\ T_{n-1,j}\big|_{x=x_i}\ T_n(x_i)+ \\
&\quad + T_1(x_i)\ T_2(x_i)...T_{n-1}(x_i)\ \ T_{n,j}\ \left.\big|_{x=x_i}\right)\Delta x_j = I_{4\times4}
\end{aligned} \tag{3.9}$$

The first term on the left hand side of the equation equals the identity matrix, as the starting configuration x_i satisfies the loop-closure equation (Eq. 3.8) by hypothesis. Therefore, this term can be simplified with the first term on the right hand side of the equation. The remaining terms can be rearranged as follows:

$$A_1\Delta x_1 + A_2\Delta x_2 + ... + A_{m-1}\Delta x_{m-1} + A_m\Delta x_m = 0_{4\times4} \tag{3.10}$$

where each of the coefficients A_j is a 4×4 matrix, expressed as:

$$A_j = T_{1,j}\big|_{x=x_i} ...T_n(x_i)) + ... + (T_1(x_i)... \, T_{n,j}\big|_{x=x_i} \tag{3.11}$$

This matrix equation can have up to 6 linearly independent scalar equations, corresponding to the 3 components of the translation vector and 3 terms from the rotation matrix. These equations can be extracted and written as an homogeneous system of linear equations (where the off-diagonal terms of the rotation matrix have been chosen):

$$\begin{bmatrix} A_1^{(1,2)} & A_2^{(1,2)} \dots A_{m-1}^{(1,2)} & A_m^{(1,2)} \\ A_1^{(1,3)} & A_2^{(1,3)} \dots A_{m-1}^{(1,3)} & A_m^{(1,3)} \\ A_1^{(2,3)} & A_2^{(2,3)} \dots A_{m-1}^{(2,3)} & A_m^{(2,3)} \\ A_1^{(1,4)} & A_2^{(1,4)} \dots A_{m-1}^{(1,4)} & A_m^{(1,4)} \\ A_1^{(2,4)} & A_2^{(2,4)} \dots A_{m-1}^{(2,4)} & A_m^{(2,4)} \\ A_1^{(3,4)} & A_2^{(4,4)} \dots A_{m-1}^{(3,4)} & A_m^{(3,4)} \end{bmatrix} \begin{bmatrix} \Delta x_1 \\ \Delta x_2 \\ \vdots \\ \Delta x_{m-1} \\ \Delta x_m \end{bmatrix} = \begin{bmatrix} 0 \\ 0 \\ \vdots \\ 0 \\ 0 \end{bmatrix} \tag{3.12}$$

The system can be written in compact form as

$$N_p \Delta x = 0 \tag{3.13}$$

where N_p is the Jacobian of the system. Non-trivial solutions to this equation belong to the null space of N_p, which can be obtained by standard methods, such as the Singular Value Decomposition (SVD) [30]. This technique computes 3 matrices U, V and S such that $N_p = USV^T$. U and V are orthogonal matrices, containing left and right singular vectors of N_p, with $U \in \mathbb{R}^{6\times6}$ and $V \in \mathbb{R}^{\mathrm{m}\times\mathrm{m}}$, whereas S is a $6 \times m$ matrix containing the singular values of N_p. Pellegrino [80] showed that the columns of V corresponding to null singular values of S constitute a basis for the space of internal mechanisms of a pin-jointed structure. Analogously, in the present study, those columns identify a basis of the space of displacements that do not violate the loop-closure equation.

If the null space has dimension 1, the mechanism has a single degree of freedom. Otherwise, any linear combination of the basis vectors of the null space is a kinematically-admissible solution, and the coefficients of the linear combination can be chosen arbitrarily. A physics-based approach to choose these coefficients for the multi-degree of freedom case is presented later in this chapter.

Once the direction of the increment x_m has been found, the new predicted configuration of the mechanism is:

$$x_p = x_i + \delta x_m \tag{3.14}$$

with δ being a scaling parameter setting the size of the increment.

3.4.2.2 Corrector Step

Linearizing the kinematics results in a small error in the loop-closure equation, which is no longer equal to the identity matrix:

$$T_1(x_p)\ T_2(x_p)...T_{n-1}(x_p)T_n(x_p) = I_{4\times4} + E \tag{3.15}$$

Similarly to what was done in the predictor step, an increment to the state vector can be introduced to correct the error matrix E, so that the following equation is satisfied:

$$T_1(x_p + \Delta x)T_2(x_p + \Delta x)...T_{n-1}(x_p + \Delta x)T_n(x_p + \Delta x) = I_{4\times4} \tag{3.16}$$

Expanding each transformation matrix to the first order, keeping only the linear terms in the products, and substituting Eq. 3.15, we obtain:

$$\begin{aligned}(T_{1,j}\big|_{x=x_p}\ T_2(x_p)...T_{n-1}(x_p)\ T_n(x_p)+ \\ + T_1(x_p)\ \ T_{2,j}\big|_{x=x_p}\ ...T_{n-1}(x_p)\ T_n(x_p)+ \\ + T_1(x_p)\ T_2(x_p)...\ T_{n-1,j}\big|_{x=x_p}\ \ T_n(x_p)+ \\ + T_1(x_p)\ T_2(x_p)...T_{n-1}(x_p)\ \ T_{n,j}\ \big|_{x=x_p})\Delta x_j = -E\end{aligned} \tag{3.17}$$

This matrix equation can be written as a system of non-homogeneous linear equations, by extracting 6 components from the matrix (3 off-diagonal terms in the rotation matrix and the translation components):

$$N_c\Delta x = -e \tag{3.18}$$

where $e = [E(1,2), E(1,3), E(2,3), E(1,4), E(2,4), E(3,4)]^T$.

A least square solution to this equation can be obtained by using the SVD of N_c [80][54]:

$$\Delta x^* = -\sum_{k=1}^{\text{rank(S)}} \frac{u_k^T \cdot e}{s_{kk}} v_k \tag{3.19}$$

where u_i and v_i are the left and right singular vectors of N_c, respectively. The predicted state of the structure can be updated with the correction $x_c = x_p + \Delta x^*$, and the correction step can be iterated until the L2 norm of the error E (or any other metric of choice) becomes lower than a set tolerance.

3.5 Folding Kinematics of 4 Strips Connected in a Square Loop

In this section, a kinematic model of a square loop composed of 4 thin-shell strips is presented. The geometry of the strips, shown in Fig. 3.7, is defined by the length $2L$ of their mid-line and the width $2w$. Each strip has two localized folds at known, fixed locations that, for simplicity, are chosen to be symmetric with respect to the symmetry plane of the strip. A non-dimensional parameter λ defines the distance between the folds, such that $\lambda = 0$ corresponds to having a single fold at the center of the strip, and $\lambda = 1$ describes two folds at the end of the mid-line. Although λ is defined in the range $[0, 1]$, not all of its values result in valid fold locations, as it is shown in Fig. 3.7. In particular, the maximum admissible distance between folds corresponds to the length of the shortest longeron: this prevents having folds on the diagonal battens, which could be potentially damaged. Therefore, the non-dimensional fold location is constrained in the range $\lambda \in [0, \lambda_{max}]$, where

$$\lambda_{max} = 1 - \frac{w}{L} \tag{3.20}$$

depends on the aspect ratio of the strip. The strips are connected to each other by hinges, aligned with their diagonal edges.

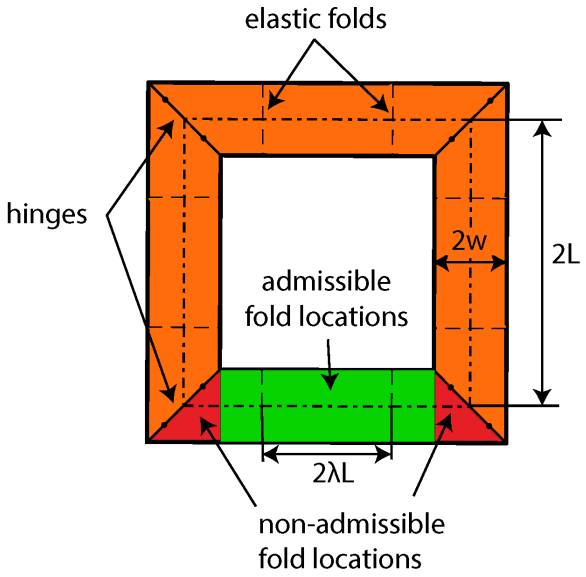

Figure 3.7: Geometry of a square loop composed of 4 trapezoidal strips connected by hinges. Each strip has two elastic folds, spaced by $2\lambda L$ and symmetric about the mid-plane of the strip. Folds on the diagonal edges of the strips are not permitted.

Fig. 3.8 shows the kinematic chain describing the kinematics of the square loop. Flat portions of the strips are idealized as rigid links, and both the hinges between

strips and the elastic folds within each strip are modeled as joints. The joints have 2 rotational degrees of freedom about perpendicular axes, as shown in Fig. 3.8b, and can be thought of as hinges with a rotating axis. This allows to model both bending β and torsion ξ of an actual strip. The resulting kinematic chain for the square loop structure contains 12 links and 24 degrees of freedom. A local coordinate frame is assigned to each link, according to the convention defined in Sec. 3.4.1. To write the loop-closure equation for the kinematic chain, it is necessary to define the coordinate transformation matrices from each link to the next one, traveling the chain in counter-clockwise direction. In the following, the notation T_{ij} describes the transformation from the $(i+1)$-th frame to the i-th frame on on the j-th strip. Since the transformation matrices on each strip share the same structure, they are derived only for a generic strip j, shown in Fig. 3.8b. They are fully defined by 6 parameters (3 translations and 3 rotations), through the sequence of elementary transformations described in Fig. 3.6. Note that β_{ij} and ξ_{ij} are free parameters, corresponding to the degrees of freedom of the joints. The remaining parameters are fixed and are reported in Tab. 3.1. The angle ϕ accounts for the hinges between strips being oriented at 45° from the axes of the elastic folds. Also, v_y is always zero, as the y-axis is perpendicular to the axis of the link, by construction. The distances in the model are non-dimensionalized by the length $2L$, so that the results are valid for strips of any size.

	ϕ	v_x	v_y	v_z
T_{1j}	$\frac{\pi}{4}$	$\frac{1-\lambda}{2\sqrt{2}}$	0	$-\frac{1-\lambda}{2\sqrt{2}}$
T_{2j}	0	λ	0	0
T_{3j}	$\frac{\pi}{4}$	$\frac{1-\lambda}{2}$	0	0

Table 3.1: Denavit-Hartenberg parameters for the transformation matrices between each link of a strip.

Once the transformation matrices have been defined, the loop-closure equation for the square loop can be written as:

$$\prod_{j=1}^{4}\left(\prod_{i=1}^{3} T_{ij}\right) = I_{4\times 4} \tag{3.21}$$

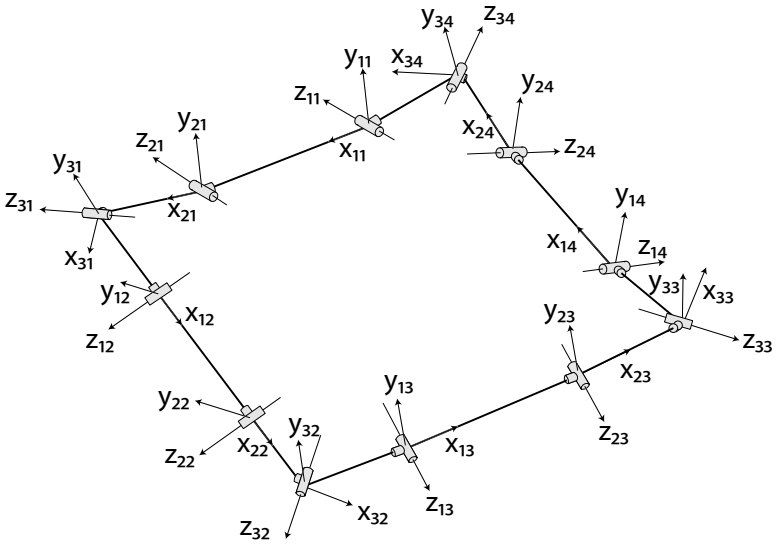

(a) Kinematic model of a square loop. The links correspond to the mid-line of each flat portion of the strips; elastic folds and hinges between strips are modeled as 2 degree-of-freedom joints. A local coordinate frame is assigned to each link

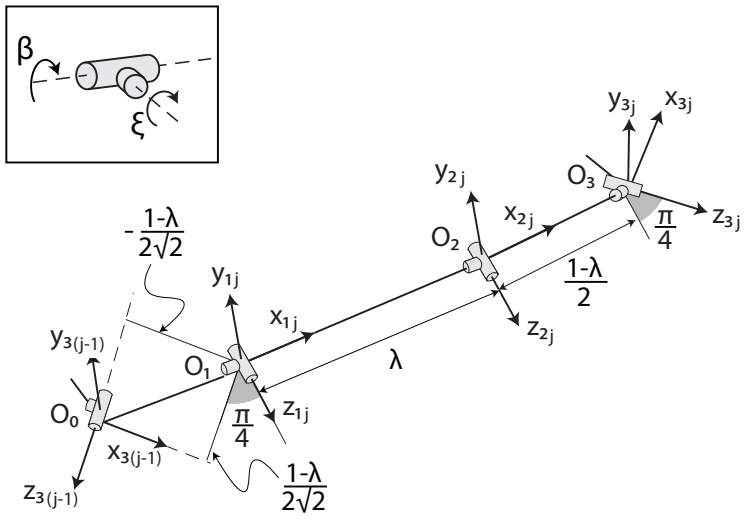

(b) Detail of the kinematic model for a strip, with its relevant dimensions. The box in the top left defines the two degrees of freedom of the joints in the model

Figure 3.8: Degrees of freedom and local reference frames for a square loop, composed of 4 trapezoidal strips hinged together at their ends. Each strip has two elastic folds equally spaced from its symmetry plane.

To solve this equation, the incremental approach presented in Sec. 3.4.1 is used. To this end, the degrees of freedom of the system are collected in the vector $x \in \mathbb{R}^{24\times1}$, to be used in the linearized form of the loop-closure equation.

$$x = \begin{bmatrix} \beta_{11} & \beta_{21} & \beta_{31} & \beta_{12} & \dots & \beta_{34} & \xi_{11} & \xi_{21} & \xi_{31} & \dots & \xi_{34} \end{bmatrix}^T \tag{3.22}$$

Next, a 4-fold symmetric solution to this equation is presented. A mirror symmetric case is also considered as a more general example of a mechanism with more than 1 degree of freedom.

3.5.1 4-Fold Symmetric Kinematics

Given that the square loop is 4-fold symmetric, it appears natural to seek a kinematic solution that preserves such symmetry. This assumption greatly reduces the number of independent variables, as all strips deform in the same way, so $\beta_{ij} = \beta_{i1}$ and $\xi_{ij} = \xi_{i1}\ \forall j \in [1, 4]$. Symmetry also requires the elastic folds to have the same angle ($\beta_{21} = \beta_{11}$) and prevents torsion between the elastic folds ($\xi_{21} = 0$). However, torsion is allowed between hinges and elastic folds, under the constraint $\xi_{31} = -\xi_{11}$. Therefore, only 3 independent variables are left:

- β_{11}, i.e. the angle of the elastic folds;
- β_{31}, i.e. the hinge angle;
- ξ_{11}, i.e. the torsion between hinges and elastic folds.

The original 24 parameters can be defined in terms of these independent variables through the following relation:

$$x = C_r x_r + \overline{x} \tag{3.23}$$

where $C_r \in \mathbb{R}^{24\times3}$ is a reduction matrix expressing the variables in x as a function of the independent variables x_r, and $\overline{x} \in \mathbb{R}^{24\times1}$ contains the degrees of freedom that have been set to a fixed value. For brevity, the full matrix C_r for the 4-fold symmetric case is not reported here, but it can be easily constructed by writing in matrix form the constraints listed at the beginning of this paragraph. Using Eq. 3.23, increments of the configuration x due to increments of the state vector x_r can be written as:

$$\Delta x = C_r \Delta x_r \tag{3.24}$$

Substituting Eq. 3.24 in the linearized form of the loop-closure equation (Eq. 3.4.2.1):

$$N_p \Delta x = 0_{6\times1} \qquad \Longrightarrow \qquad N_p C_r \Delta x_r = N_r \Delta x_r = 0_{6\times1} \tag{3.25}$$

it is possible to define a reduced Jacobian $N_r = N_p C_r \in \mathbb{R}^{6\times3}$ for the system.

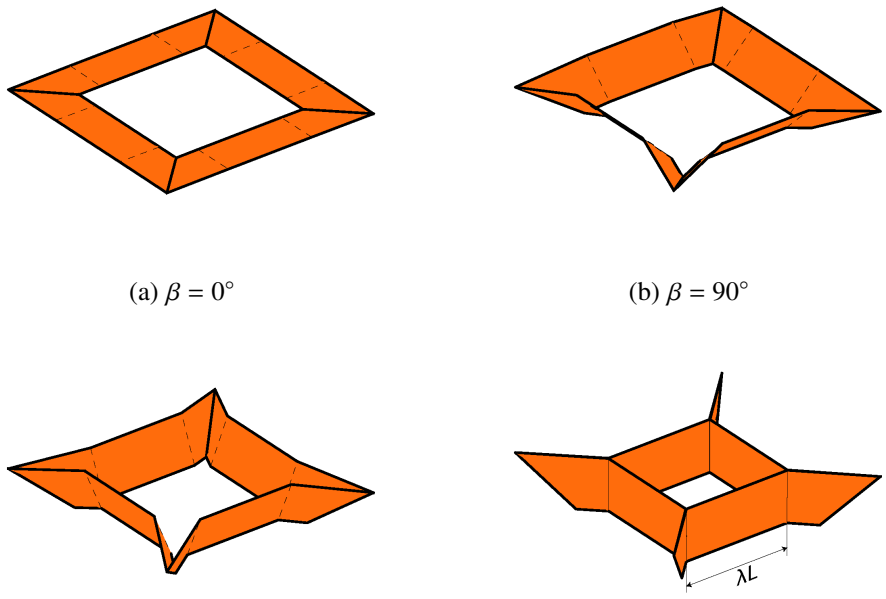

(a) $\beta = 0°$ (b) $\beta = 90°$

(c) $\beta = 135°$ (d) $\beta = 180°$

Figure 3.9: 4-fold symmetric folding sequence for a square with $\lambda = 0.5$.

Applying the incremental solution approach to the reduced model, it was found that N_r has rank 2 throughout the folding process, so that there is only one kinematically-admissible path between planar and folded configuration. Snapshots of the solution for different values of the hinge angle β_{31} are shown in Fig. 3.9. Fig. 3.10a shows the evolution of the fold angle β_{11} and strip torsion ξ_{11} as a function of the hinge angle β_{31}. The plot shows that β_{11} monotonically decreases from 0° to -45° when the hinge angle is increased from 0° to 180°. Also, it can be observed that this kinematic path does not require any torsion of the strip, which is ideal as it reduces the stress on the structural components. Fig. 3.10b plots the evolution of the singular values for the Jacobian N_r as a function of the hinge angle β_{31}. The plot shows that one of the singular values is always equal to zero, corresponding to the compatible kinematic path. The other 2 singular values are greater than zero for all values of β_{31}, except for the initial point $\beta_{31} = 0$, where the rank of N_r drops to 1. This indicates a bifurcation

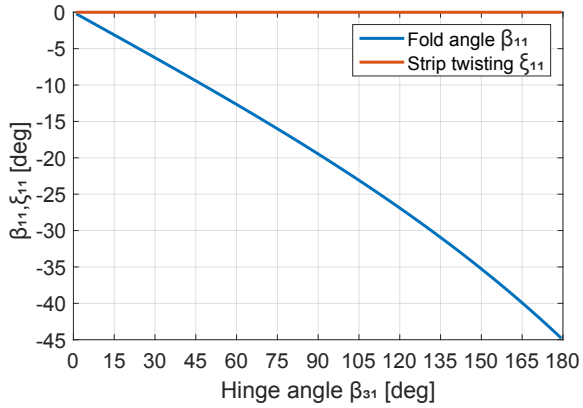

(a) Kinematics of the square along its 4-fold symmetric folding path

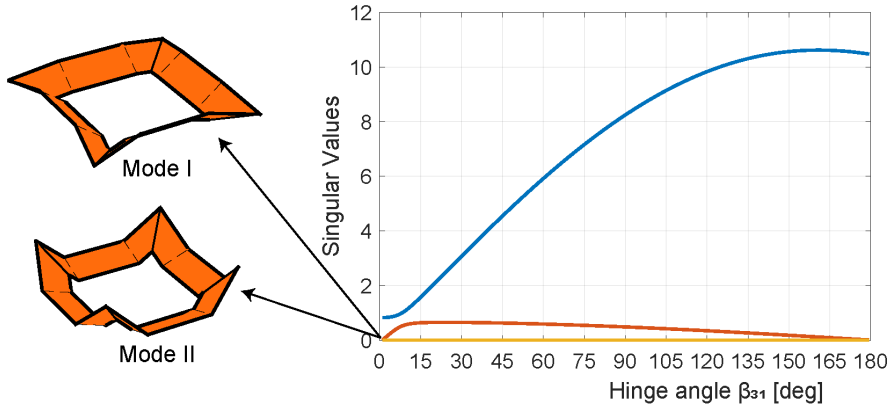

(b) Singular values along the 4-fold symmetric path. The two configurations on the left hand side correspond to different kinematic paths at the bifurcation point

Figure 3.10: 4-fold symmetric folding path for 4 strips arranged in a square loop. The results are independent of the spacing λ between the elastic folds.

point, where two different kinematic paths meet. The alternative path consists of the ends of the strips folding inwards, towards the center of the square (lower figure in Fig. 3.10b). To avoid the bifurcation, a small perturbation, of the order of 10^{-3} rad, was applied to the initial configuration of the kinematic simulation. Note that the results shown in Fig. 3.10 were derived for a fold spacing $\lambda = 0.5$. However, it was observed that the results were identical for any other value of λ. This means that, although different λ's correspond to different geometric configurations of the structure, the relationship between the hinge angle and fold angle is not affected.

3.5.2 Kinematics with Mirror Symmetry

While a 4-fold symmetric path offers a single degree-of-freedom mechanism for the structure, implementing it requires simultaneous control over the 4 corners of the square loop, to make sure that symmetry is indeed preserved. In some instances, it might be acceptable to sacrifice the predictability of this process for a simpler folding procedure, to reduce the number of people required to fold the structure. For example, a mirror symmetric folding scheme could be devised, in which a square loop is folded in two steps, controlling two corners at a time. The folding sequence for this process is shown in Fig. 3.11.

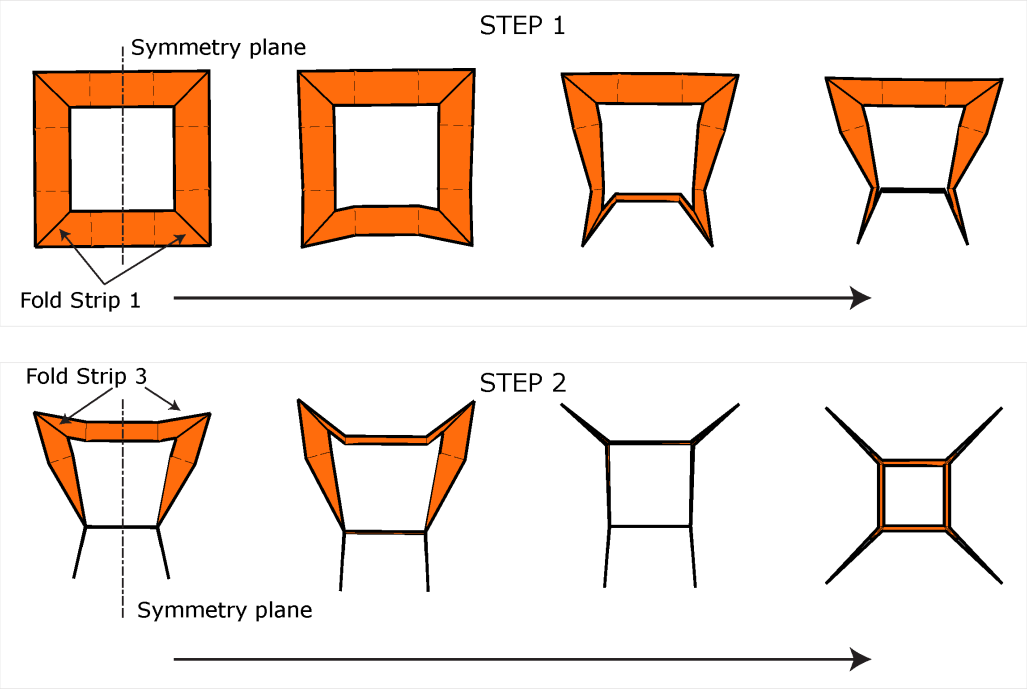

Figure 3.11: Mirror symmetric folding sequence for a square loop: corners C1 and C2 are folded first (strip 1), followed by corners (C3 and C4).

One of the strips is folded first, by rotating its ends by 180° in a symmetric fashion; then the opposite strip is folded in a similar way. To model the kinematics of this process, the general model of the square loop was reduced by means of the following transformation:

$$\begin{bmatrix} \beta \\ \xi \end{bmatrix} = \begin{bmatrix} C^{\beta} & 0_{12\times5} \\ 0_{12\times6} & C^{\xi} \end{bmatrix} \begin{bmatrix} \beta^{r} \\ \xi^{r} \end{bmatrix} \Longrightarrow x = C^{r}x^{r} \tag{3.26}$$

which reduces the original 24 degrees of freedom mechanism to only 11 (6 bending rotations β_j and 5 torsional rotations ξ_j). The full transformation matrices C^{β} and

C^{ξ} are reported below.

$$\begin{bmatrix} \beta_{11} \\ \beta_{21} \\ \beta_{31} \\ \beta_{12} \\ \beta_{22} \\ \beta_{32} \\ \beta_{13} \\ \beta_{23} \\ \beta_{33} \\ \beta_{14} \\ \beta_{24} \\ \beta_{34} \end{bmatrix} = \begin{bmatrix} 1 & 0 & 0 & 0 & 0 & 0 \\ 1 & 0 & 0 & 0 & 0 & 0 \\ 0 & 1 & 0 & 0 & 0 & 0 \\ 0 & 0 & 1 & 0 & 0 & 0 \\ 0 & 0 & 0 & 1 & 0 & 0 \\ 0 & 0 & 0 & 0 & 1 & 0 \\ 0 & 0 & 0 & 0 & 0 & 1 \\ 0 & 0 & 0 & 0 & 0 & 1 \\ 0 & 0 & 0 & 0 & 1 & 0 \\ 0 & 0 & 0 & 1 & 0 & 0 \\ 0 & 0 & 1 & 0 & 0 & 0 \\ 0 & 1 & 0 & 0 & 0 & 0 \end{bmatrix} \begin{bmatrix} \beta_{11} \\ \beta_{31} \\ \beta_{12} \\ \beta_{22} \\ \beta_{32} \\ \beta_{13} \end{bmatrix} \Longrightarrow \beta = C_r^{\beta} \beta^r \tag{3.27}$$

$$\begin{bmatrix} \xi_{11} \\ \xi_{21} \\ \xi_{31} \\ \xi_{12} \\ \xi_{22} \\ \xi_{32} \\ \xi_{13} \\ \xi_{23} \\ \xi_{33} \\ \xi_{14} \\ \xi_{24} \\ \xi_{34} \end{bmatrix} = \begin{bmatrix} 1 & 0 & 0 & 0 & 0 \\ 0 & 0 & 0 & 0 & 0 \\ -1 & 0 & 0 & 0 & 0 \\ 0 & 1 & 0 & 0 & 0 \\ 0 & 0 & 1 & 0 & 0 \\ 0 & 0 & 0 & 1 & 0 \\ 0 & 0 & 0 & 0 & 1 \\ 0 & 0 & 0 & 0 & 0 \\ 0 & 0 & 0 & 0 & -1 \\ 0 & 0 & 0 & -1 & 0 \\ 0 & 0 & -1 & 0 & 0 \\ 0 & -1 & 0 & 0 & 0 \end{bmatrix} \begin{bmatrix} \xi_{11} \\ \xi_{12} \\ \xi_{22} \\ \xi_{32} \\ \xi_{13} \end{bmatrix} \Longrightarrow \xi = C_r^{\xi} \xi^r \tag{3.28}$$

During the second folding step, the rows of the matrices corresponding to β_{31} and ξ_{11} were set to zero to fix the folded corners of the square loop.

Under the assumption of mirror symmetry, the linearized kinematics in Eq. 3.25 becomes underdetermined, as it has 6 equations and 11 unknowns. The singular value decomposition of the Jacobian N_p shows that the system has rank 6, hence the null space of the matrix has dimension 5. Therefore, the choice of the increment of displacement during the predictor step is not unique, and additional conditions are required. A intuitive solution would be to assign arbitrary values to 4 of the free

variables to obtain a single D.o.F. system. However, it was found that this approach can lead to unrealistic kinematic paths for the structure, characterized by very large rotations of some of the joints to accommodate for the locked degrees of freedom.

The alternative solution proposed here consists of adding "soft" constraints to the system, by keeping its 11 degrees of freedom and choosing a suitable direction of the solution increment from the null space of the Jacobian N_p. In particular, recalling that, for a system with m degrees of freedom, the m right-most columns of the matrix of right singular vectors V constitute a basis V_m for the null space of the system, the solution increment x_m can be written as a linear combination of these vectors:

$$x_m = V_m c \tag{3.29}$$

where c is a vector of coefficients. The coefficients are computed by solving the following optimization problem

$$c^* = \arg\min_c J \tag{3.30}$$

in which the cost function J is defined according to the following physical and practical considerations:

1. During folding, the structure lies on a planar surface, and it tends to stay in contact with it due to gravity;
2. The largest displacements (rotations) should occur on the degrees of freedom being controlled;
3. Torsional rotations should be as small as possible, to minimize the stress on the structure.

Each of these criteria is expressed mathematically by a function J_i, and the cost function J for the optimization is defined by linear scalarization of its components, using weights W_i that were manually tuned:

$$J = \sum_{i=1}^{3} W_i J_i \tag{3.31}$$

The planarity condition (1) is defined as follows:

- First, the coordinates of the lower longerons of the strip are evaluated at the joint locations, and expressed in their local frames ($P_i = [0, 0, -w, 1]^T$ at

the elastic fold locations, $P_i = [0, 0, -\sqrt{2}w, 1]^T$ at the location of the hinges between strips).

- The coordinates P_i are converted to the same coordinate frame using compound transformation matrices $P_i^{(0)} = T_0^i P_i$;
- A global frame is defined, with the origin at the centroid O of the points $P_i^{(0)}$ and the axes aligned with the 0-th local frame. The global coordinates of the points were computed as $\overline{P}_i = P_i^{(0)} - O$;
- The global coordinates of the points are fitted with a plane. This can be done using the Principal Component Analysis (PCA) on the matrix of coordinates X. The PCA returns the eigenvectors of the covariance matrix $X^T X$; the eigenvector corresponding to the smallest eigenvalue of $X^T X$ defines the normal n to the fitting plane.
- The cost function contribution J_1 is defined as: $J_1 = \sum_i \left| \frac{\overline{P}_i}{\|\overline{P}_i\|} \cdot n \right|$.

The second condition, i.e. that the displacement of the controlled D.o.F.'s should be larger than any other component, is expressed as:

$$J_2 = 1 - \|x_c\| \tag{3.32}$$

where x_c is a vector containing the components of x_m associated with the control variables. The last criterion, i.e. minimizing torsion, is defined as:

$$J_3 = \|\xi\| \tag{3.33}$$

where $\xi = [\xi_{11}, ...\xi_{34}]^T$ contains all the torsional components of the state vector. The optimization problem was solved using a quasi-Newton algorithm in MATLAB. Fig. 3.12 shows the evolution of the bending and torsional degrees of freedom for the 2-step mirror symmetric folding path, on a strip with $\lambda = 0.5$. In the first step, the control variable is β_{31}, and it increases monotonically from 0° to 180°, while the fold angle β_{11} on strip 1 decreases to approximately -90°. The other bending angles experience a small variation, to approximately 30°. Torsion is generally small, with the largest contribution coming from ξ_{22}, i.e. the twisting between the fold angles associated with strips 2 and 4.

The results from this subsection show that it is possible to star-fold a square loop structure by controlling only 2 degrees of freedom. This can be advantageous

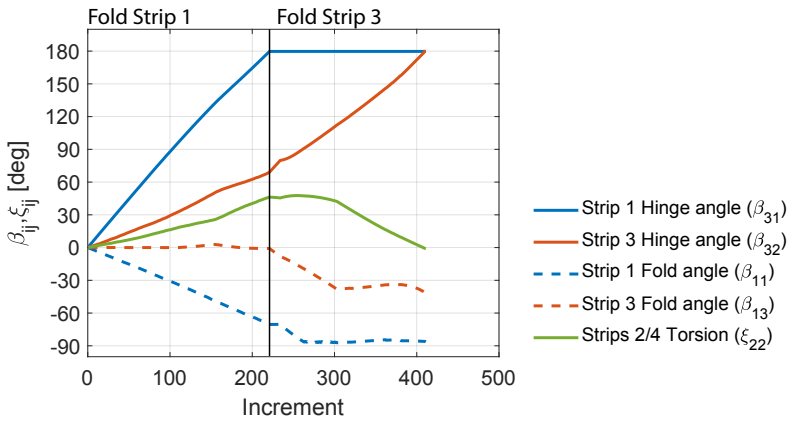

Figure 3.12: 2-step folding kinematics: strip 1 is folded first, followed by strip 3.

in some cases, especially for small scale structures, as it reduces the number of people involved in the packaging process. However, this comes at the cost of a less deterministic kinematics, as there are multiple degrees of freedom. While the results in Fig. 3.11 show a desirable sequence of configurations of the structure during packaging, this is not the only possible path. Therefore, in the rest of this chapter, a 4-fold symmetric packaging scheme is assumed for the structure, as it guarantees a unique kinematic path.

3.6 Folding a Space Structure with Multiple Squares

In the previous section, a kinematic model for a single square loop was presented, and it was shown that a 4-fold symmetric folding process would result in a single degree of freedom kinematic path. This implies that, even when multiple square loops are connected to each other in a more complex space structure, each of them evolves essentially as an independent unit. However, the sequence by which the square loops are folded and their relative position during this process must be chosen such that their kinematics is compatible with the boundary conditions.

In this section, a space structure consisting of 3 square loops connected by diagonal cords(see Fig. 3.4) is considered. The geometry of the structure, shown in Fig. 3.13, can be described in terms of 2 non-dimensional geometric parameters, i.e. the aspect ratio of the inner strip $\hat{w} = w/L$ and the non-dimensional joint spacing $\hat{\eta} = \eta/\sqrt{2}w$. The gap between strips $\hat{g} = g/w$ is also defined as a third parameter, but it is less critical and will be neglected for the purpose of this discussion. Unless otherwise specified, the results in this section assume $\hat{w} = 0.55$ and $\hat{\eta} = 0.53$, corresponding to the design point of the physical prototype presented later in this chapter. The goal

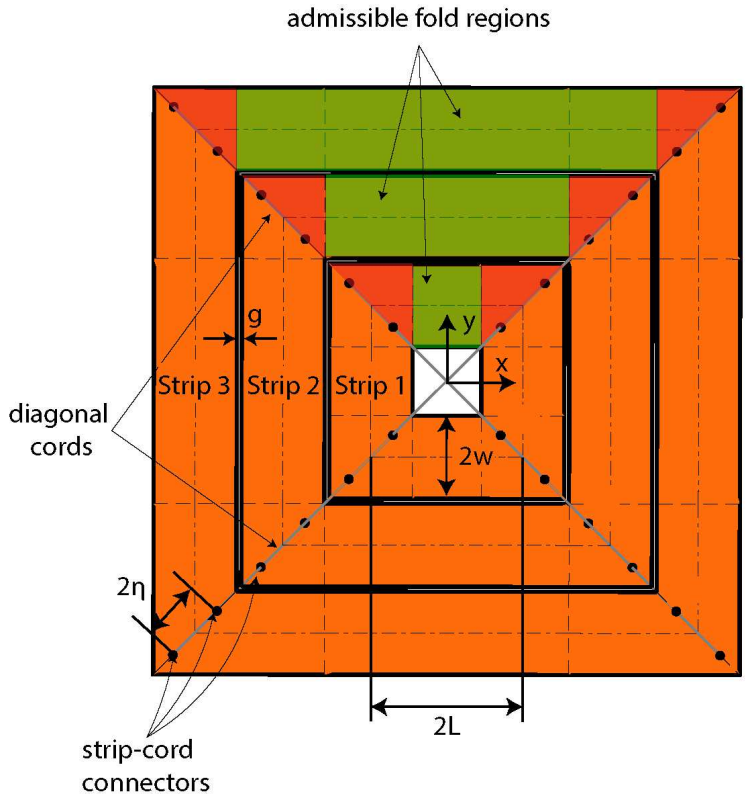

Figure 3.13: Geometry of a space structure with 3 square loops. Each strip has 2 elastic folds, symmetric with respect to its mid-plane.

of this section is to design a folding sequence for which the structure can be folded in a simple and predictable way.

3.6.1 Folding Square Loops in Sequence

An intuitive solution would be to fold one square loop at the time, starting from the outermost one and proceeding inwards. Each of the squares can be folded using the 4-fold symmetric path presented in Figs. 3.9 and 3.10a.

For independent square loops, the elastic folds could be ideally placed anywhere in the admissible region of the strips (green area in Fig. 3.13), as previously mentioned. However, the presence of multiple concentric square loops constrains the location of the folds, as the square loop being folded cannot geometrically interfere with the other squares inside. This is important as, during star folding, the minimum distance between opposite strips of the i-th square loop gradually reduces from its original value of $2(L_i - w)$ to $2\lambda_i L_i$, as shown in Fig. 3.9. In the presence of a smaller square inside, this distance cannot be smaller than the outer size of the inner square, hence:

$$\lambda_i L_i \geq L_{i-1} + w \tag{3.34}$$

The two half-lengths L_i and L_{i-1} are related by the following geometric relationship:

$$L_{i-1} = L_i - 2w - q \tag{3.35}$$

Substituting in Eq. 3.34, the inequality can be solved in terms of λ_i:

$$\lambda_i \geq \frac{L_i - w - q}{L_i} = 1 - \frac{w}{L_i} - \frac{q}{L_i} \tag{3.36}$$

In practice, the last term on the right-hand side of the inequality is very small (typically in the order of 10^{-2}) and therefore can be neglected. Recalling the geometric constraint for λ_{max} in Eq. 3.20 ($\lambda_i \leq \lambda_{i,max} = 1 - \frac{w}{L_i}$), it can be concluded that sequential folding is only possible if the elastic folds are placed at the edges of their admissible region in Fig. 3.13, i.e. at the ends of the shortest longeron in the square. Using this approach, the folding sequence in Fig. 3.14 is obtained. At each step of the process, a square loop folds according to the 4-fold symmetric path derived in Sec. 3.5, while the inner squares remain planar. The outer squares are already folded, but they have to undergo a second folding phase (as shown in Fig. 3.15) in order to follow the displacements of the active square. This is necessary to satisfy the constraint imposed by the cords connecting the strips. Indeed, as previously mentioned, the inner dimension of the folded squares equals the distance between elastic folds on the same strip. As the fold spacing changes between square loops, the final structure would end up forming concentric squares of different sizes, rather than the star shape shown in Fig. 3.14.

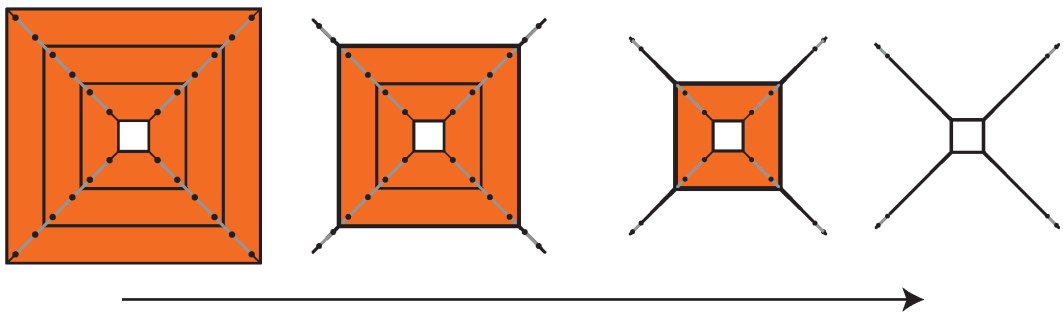

Figure 3.14: Folding sequence for a space structure with 3 square loops, being folded one at a time (top view).

To avoid this problem, the location of the folds on the folded squares must be changed to match the fold spacing on the active square loop. This can be done by adding

two localized folds at the desired spacing, and folding them until the angle of the existing folds becomes zero. Fig. 3.15a shows a snapshot of this process, where B indicates the initial fold location, and A the new fold location. The kinematics of this process can be described in 2 dimensions, as it does not involve any out-of-plane displacements of the strip, and it is shown in Fig. 3.15b, where only half of the mid-line of the outer strip is drawn, for clarity. In the plot, points B and C lie on the diagonal symmetry plane $x = y$, and their coordinates are related by the geometric relation:

$$x_C = x_B + \frac{L_i - b}{\sqrt{2}} \tag{3.37}$$

The location of B can be, in turn, computed by imposing $AB = b - a$, which can be expanded as:

$$2x_B^2 - 2(x_A + a)x_B + x_A^2 + a^2 - (b - a)^2 = 0 \tag{3.38}$$

The two solutions to this equation correspond to having B on either side of A on the line $x = y$. Therefore, only its positive root can be accepted. Note that a and b correspond to the distance between the symmetry plane of the strip and the two folds, measured along the strip mid-line. Equation 3.38 has a single free parameter x_A, which controls the folding process. Initially, $x_A = b$, corresponding to $\beta_B = 45°$ and $\beta_A = 0°$; at the end of this step, $x_A = a$, so that $\beta_B = 0°$ and $\beta_A = 45°$. In a kinematic simulation of multiple square loops, x_A can be chosen to match the corresponding point on the adjacent square loop, in order to minimize their distance.

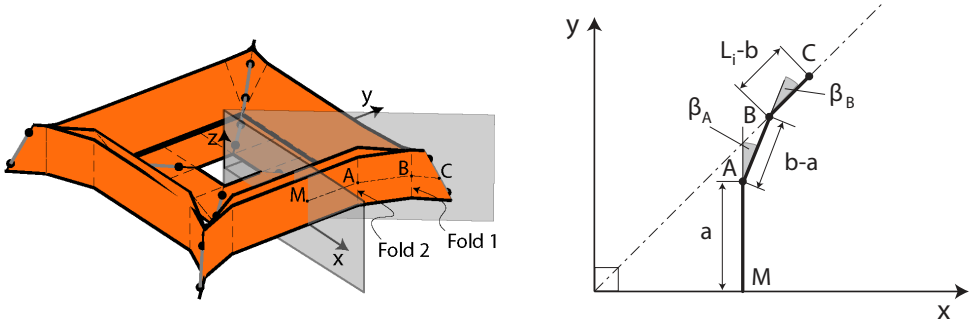

(a) (b)

Figure 3.15: Kinematics of a folded square loop during formation of a secondary elastic fold.

In addition to imposing constraints to the kinematics of the square loops in the $x - y$ plane, the cords between strips significantly affect their out-of-plane displacements too. These additional constraints can be used to locate the strips with respect to

each other in the z-direction, throughout the folding process. Here, it is assumed that the structure sits on a flat surface, e.g. a table, during packaging. This is not strictly necessary (one could also lift the structure by offloading it), but it is certainly the simplest and most practical solution. Because of gravity, each square loop tends to sit on the base surface (located at $z = 0$) at any time; however, in some configurations, the cord length constraints do not allow it, resulting in an offset Δz_i from this plane. Fig. 3.16 shows a section view of the structure at an intermediate step of the folding process, and it defines the offsets Δz_2 and Δz_1 for the middle square (being folded) and the inner square (still planar), respectively. In this case, the lower longeron of the outermost square is located at $z = 0$.

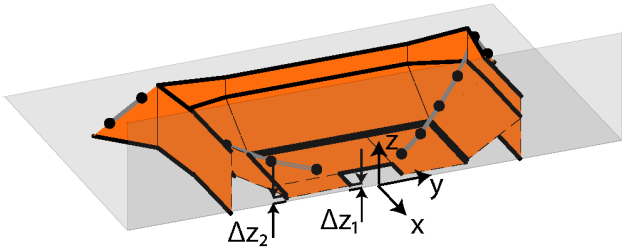

Figure 3.16: Vertical displacement of the strips from the plane $z = 0$.

The vertical offsets are computed through the following algorithm, formulated for a structure with N strips:

- Compute the configuration of the outermost square in the structure, and set its lowest point to $z = 0$;
- Solve the kinematics of the $(N - 1)$-square loop to reconstruct its shape;
- For any offset $\Delta z_{N-1} \in [\Delta z_{min}, \Delta z_{max}]$, compute the distance between the inner strip-cord connector Q_N^- of the N-th strip and the outer strip-cord connector Q_{N-1}^+ of the $(N - 1)$-th strip;
- From the vector of distances $d_{N-1,N}$, exclude the values for which the distance exceeds the length of the cords ($L_c = 2\sqrt{2}w(1 - \hat{\eta})$, with $\eta \in [0, 1]$);
- Pick the smallest, non-negative Δz_{N-1} for which the cord length constraint is satisfied;

- If there are no suitable non-negative offsets, choose the smallest (in absolute value) Δz_{N-1}, and shift all the square loops so that the lowest point in the structure is located at $z = 0$;
- Repeat for the remaining square loops.

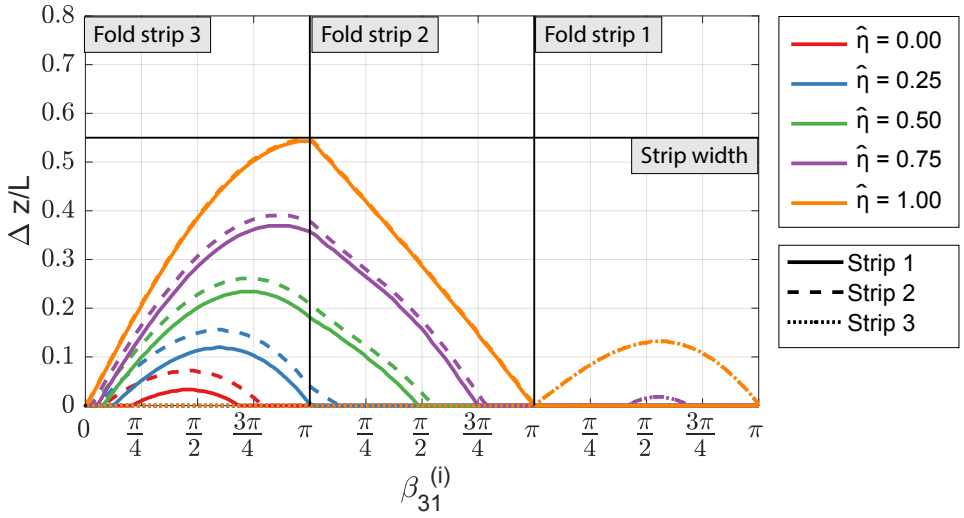

Figure 3.17: Vertical displacement of the strips required to folding one square loop at a time, for a space structure with 3 square loops. Results are shown for different joint spacing $\hat{\eta}$.

The range of offsets is chosen to be large enough to include all the configurations of practical interest ($\Delta z_{max} = 2w = -\Delta z_{min}$). Figure 3.17 shows the required vertical offset for a structure with 3 square loops and $\hat{w} = 0.55$, packaged by folding one square loop at a time. Solid, dashed and dotted lines correspond to different square loops, and the results are computed for different values of the parameter $\hat{\eta}$. The plot shows that, during the first folding step, the middle and inner square loops need to be lifted from the ground. The amplitude of the vertical displacement increases as the spacing between strip-cord connectors increases, and it becomes as high as the entire width of the strip for $\hat{\eta} = 1$. A non-zero offset remains at the end of the first step, and it decrease to zero during the second folding step. In the final step, the middle and outer square loops (already folded) need to be lifted for $\hat{\eta} > 0.75$.

3.6.2 Folding Square Loops in Pairs

In the previous subsection, a folding scheme was proposed for which the square loops would be folded one at the time, starting from outermost one and proceeding inwards. Despite its conceptual simplicity, implementing this folding scheme is

challenging due to the significant vertical offsets involved, as shown in Fig. 3.17. The kinematic analysis shows that, at the end of the first step, the middle and inner square loops need to be lifted from the ground, thus requiring some suspension system. Here, an alternative folding scheme is proposed, based on the idea of folding square loops in pairs rather than individually. It is shown that this scheme can dramatically reduce the vertical offset required during folding, and entirely solves the problem of having to support the structure in between folding steps.

The simple underlying argument is that Z-folding requires a sequence of mountain and valley folds. When folding one square loop at the time, the remaining flat portion of the structure needs to align with the mountain or valley folds, alternatively. However, if the square loops are folded in pairs, with a mountain fold in between them, the remaining square loops ideally are always aligned with the valley folds, therefore lying on the ground. For a 3-square-loop structure, the resulting folding scheme is shown in Fig. 3.18. The outer and middle square loops are folded first, followed by the inner square.

In this case, the elastic folds on the strips in the second and third square loops must have the elastic folds at the same locations. This guarantees that, in their folded configuration, they will have the same size of the inner square. The location of the folds is set by:

$$\lambda_2 = 1 - \frac{w}{L_2} \tag{3.39}$$

$$\lambda_3 = 1 - 3\frac{w}{L_3} \tag{3.40}$$

so that their actual distance is the same $d_f = 2\lambda_2 L_2 = 2\lambda_3 L_3$. Increasing the distance between folds would place them in the non-admissible region for the middle square (Fig. 3.13), while reducing it would result in geometric interference with the inner square.

Figure 3.19 shows the required vertical offset Δz from the kinematic analysis of the 2-step folding scheme, as a function of the non-dimensional joint spacing $\hat{\eta}$. Similar to the previous case, some offset is required on the inner and middle square loops (strips 1 and 2, respectively), during the initial folding step. However, the amplitude of the offset is about 50 % lower than in the previous case, with the maximum height reaching half of the strip width for $\hat{\eta} = 1$. More importantly, no offset is required at the end of the first folding step regardless of the value of $\hat{\eta}$. During the second folding step, the middle and outer strips require a vertical offset only for $\hat{\eta} > 0.75$, analogous to the previous folding concept.

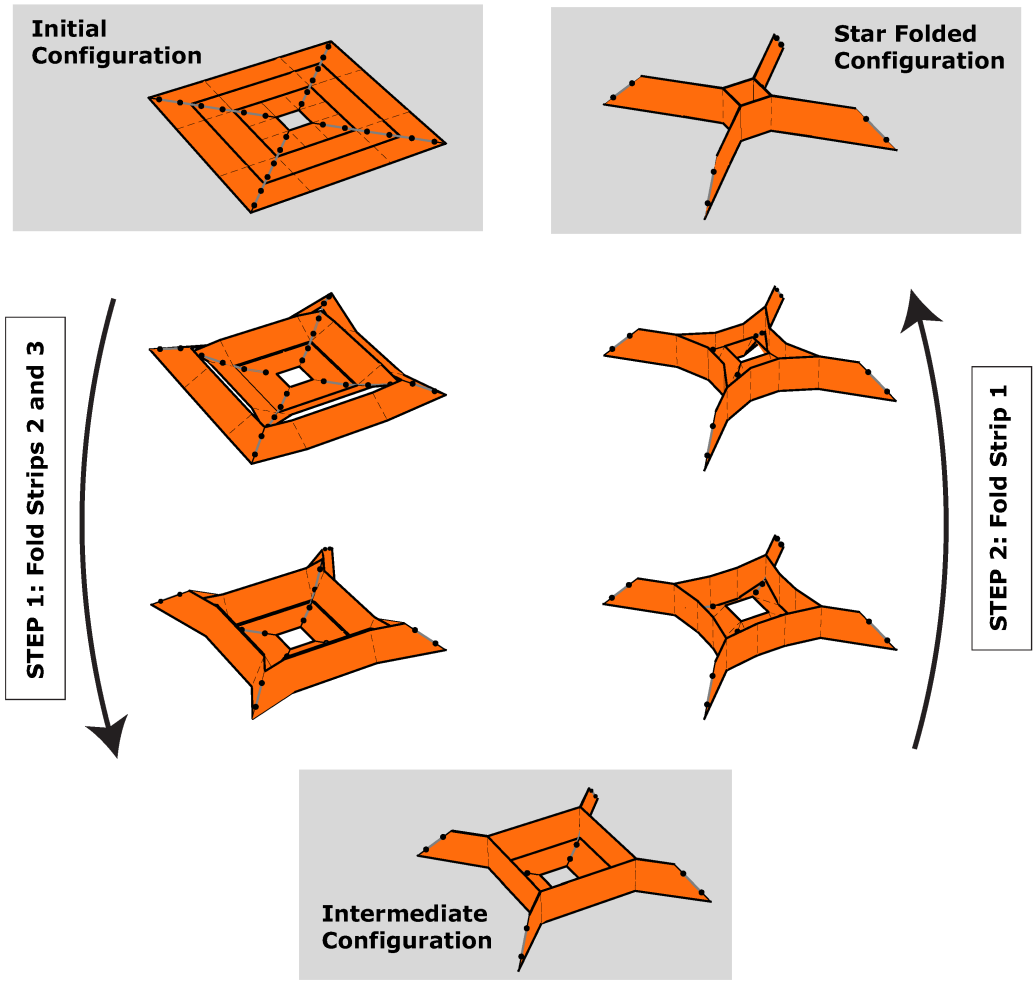

Figure 3.18: 2-step symmetric folding sequence for a space structure with 3 square loops.

To understand how the maximum offset changes with the size of the structure, the kinematic analysis was repeated for a space structure with 10 square loops, $\hat{w} = 0.55$ and $\hat{\eta} = 0.53$. In this case, the packaging process would require 5 steps, each folding a pair of square loops. The required offsets are shown in Fig. 3.20: pairs of square loops folded together are plotted with the same color. The figure shows that the maximum offset is the same for all the steps, and it amounts to about 13% of L. During the first step, strip 10 remains on the plane $z = 0$, while strip 9 experiences the largest vertical offset. The offset decreases as one moves inwards, with strips 1-4 not requiring any offset at all. A similar trend is observed for the other steps, in which the inner square of the pair being folded always records the same maximum Δz, and the 4 adjacent squares requiring a lower value. Additionally, the strips already folded need a small offset (with a maximum $\Delta z/L = 0.04$) too, when the

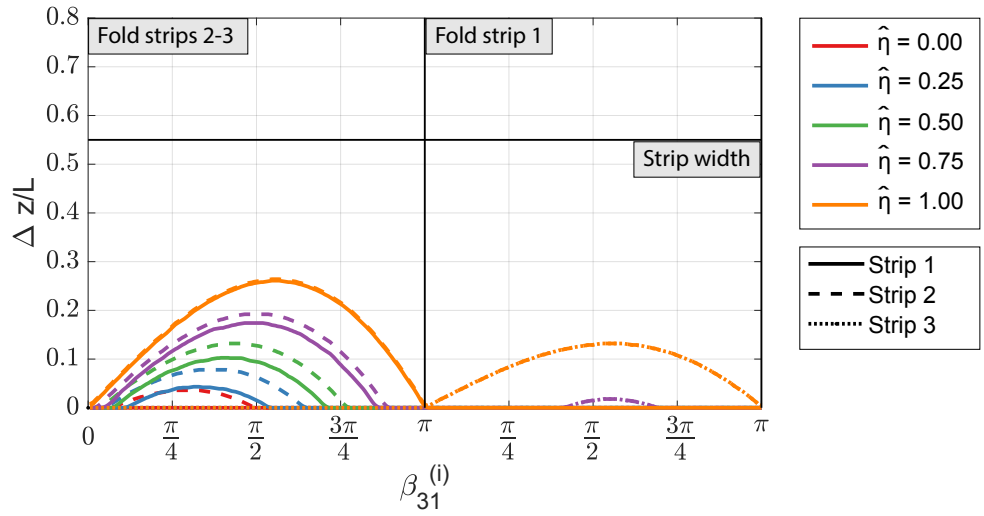

Figure 3.19: Vertical displacement of the strips required to fold the square loops in pairs, for a space structure with 3 square loops. Results are shown for different joint distance $\hat{\eta}$.

fold angle is in the range $\beta_{31}^{(i)} \in [\frac{3\pi}{8}, \frac{3\pi}{4}]$.

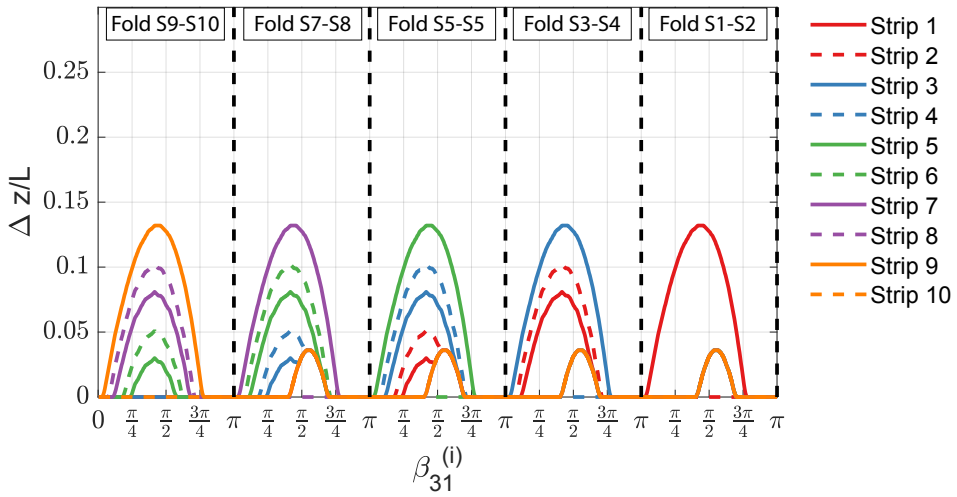

Figure 3.20: Vertical displacement of the strips to fold a space structure with 10 strips, folded in pairs. Results shown for $\hat{w} = 0.55$ and $\hat{\eta} = 0.53$.

Since the maximum Δz for a structure is independent of the number of square loops, it can only depend on the geometry of the strips, namely the parameters $\hat{w}$ and $\hat{\eta}$ defined in Fig. 3.13. Therefore, the design space was explored to find the maximum Δz as a function of those parameters, and the results are shown in Fig. 3.21. From the map, it can be concluded that the offset increases both with the width of the strip and the spacing between joints. In the worst case scenario, $\hat{w} = 1$ and $\hat{\eta} = 1$, Δz_{max}

becomes about 42% of the inner strip half-length L. The map also shows the design point for the structural prototype introduced in the next subsection.

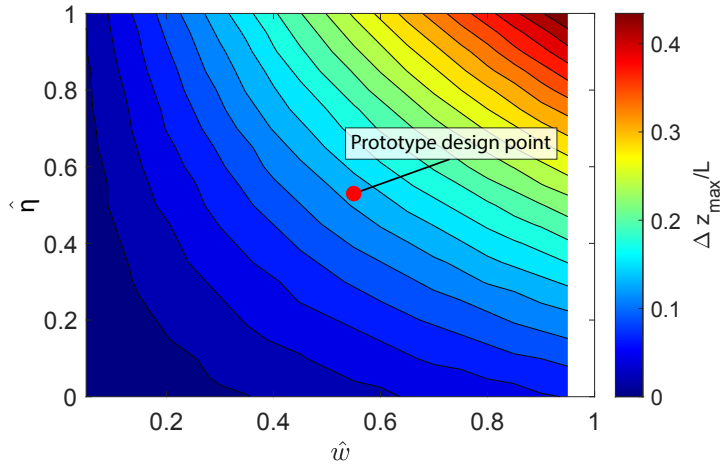

Figure 3.21: Maximum vertical displacement of the strips to fold the square loops in pairs, as a function of the non-dimensional strip width $\hat{w}$ and joint spacing $\hat{\eta}$.

3.6.3 Packaging of a 2-m-Scale Space Structure Prototype

The packaging scheme illustrated in Fig. 3.18 was demonstrated on a 1.7 m × 1.7 m space structure prototype, consisting of 3 strips, each about 250 mm wide (including both the membrane and the longerons). Elastic folds were imposed at the desired locations using hairpins to locally pinch each longeron in the strips. A 2-step process was implemented, with the middle and outer square loops being folded first, followed by the inner one. At the end of each folding step, additional hairpins were added to hold together the folded strips.

For a structure of this size, it was found that 2 people were sufficient to achieve symmetric folding. While the kinematic model assumed that the control variable for the packaging process would be the angle of the strips about the diagonal cords (β_{3i}), in practice it was easier to fold the structure using different control points. In particular, the first folding step was controlled by lifting the mountain fold between strips 2 and 3 at the location of the diagonal cords (red arrows in Fig. 3.22a), so that the strips would spontaneously rotate about the cord axes under the effect of gravity. In the second step, the shorter longeron of the inner strips was lifted, while the middle and outer strips, already folded, were pushed inwards until the structure achieved its star shape configuration.

Fig. 3.22 shows the sequence of intermediate configurations during the packaging

process, which were remarkably close to the predictions from the kinematic model (Fig. 3.18). The main deviation between model and implementation was in the location of the elastic folds for the first step. In particular, the model expected the distance between the folds to match the length of the short longeron on the second strip. In practice, this configuration resulted in geometric interference with the inner square loop, as the actual thickness of the longerons on the middle square reduced the available volume inside the folded squares. This was adjusted by increasing the distance between folds (by about 30 mm) until the inner square could fit in between the others. While this solution required some bending of the diagonal battens, they were flexible enough to tolerate such deformations.

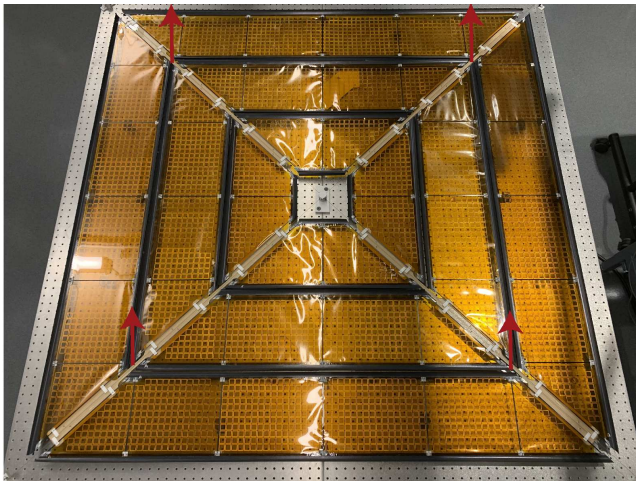

(a) Deployed configuration

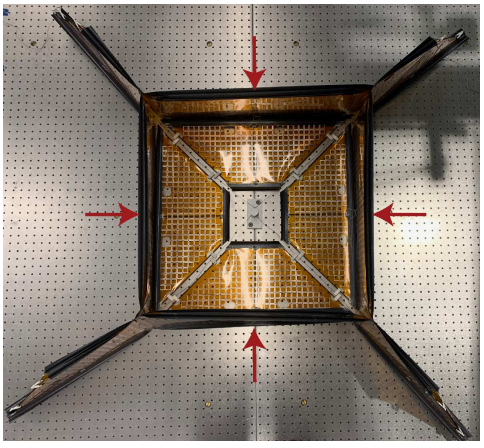

(b) Strips 2 and 3 folded

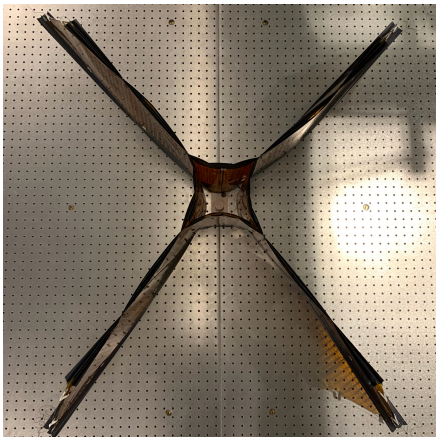

(c) Fully-folded configuration

Figure 3.22: Packaging sequence for a 1.7m×1.7m space structure prototype with 12 strips arranged in 3 square loops.

3.7 Coiling Concept

At the end of the folding process, the structure reaches its star shape and is ready for the coiling step, which brings it to its final cylindrical configuration. A sequence of snapshots from a kinematic model of this process is shown in Fig. 3.23. The derivation of this kinematic model is beyond the scope of the present work, as it is not instrumental in the present discussion. Instead, the objective of this section is to discuss the implementation of this coiling scheme, and to present a novel deployment mechanism concept capable of achieving controlled, robust, and predictable coiling/uncoiling of the structure.

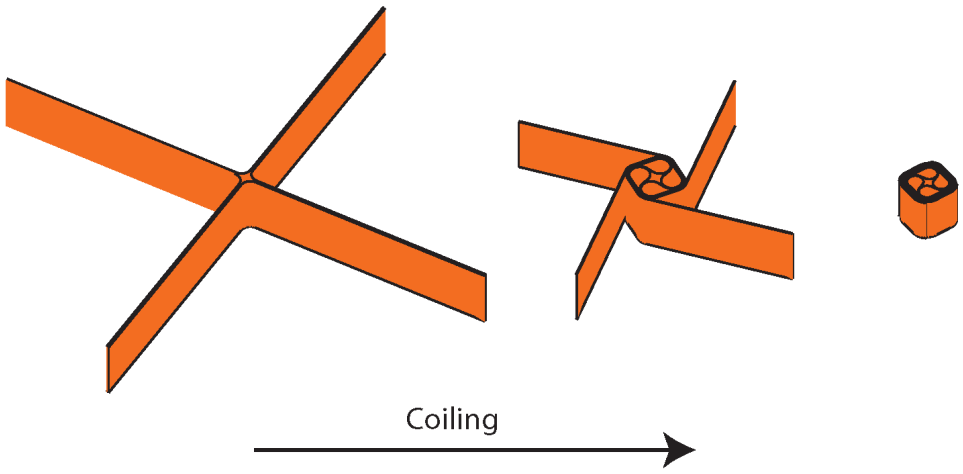

Figure 3.23: Coiling sequence for a 4-fold symmetric structure.

3.7.1 Challenges in Coilable Thin-Shell Structures

Most thin-shell deployable structures used in aerospace applications are packaged by coiling. The main advantage of this process is its high packaging efficiency and scalability to large structures. However, controlling their behavior is challenging: coiled shells tend to self-deploy to release their stored strain energy, and they typically do not spontaneously conform to the desired coiled radius. A number of studies have identified 2 types of instabilities in coiled thin-shell structures. Blossoming (Fig.3.24a) occurs when the coiled shell uniformly increases its coiling radius [39], whereas buckling (Fig. 3.24b) leads to the formation of uniformly spaced regions of high curvature, connected by straight portions of the shell [43][20][79] [76].

Wilson et al. [105] showed that the type of instabiity that occurs depends on the ratio between the coiling radius R and the natural radius of curvature of the shell r,

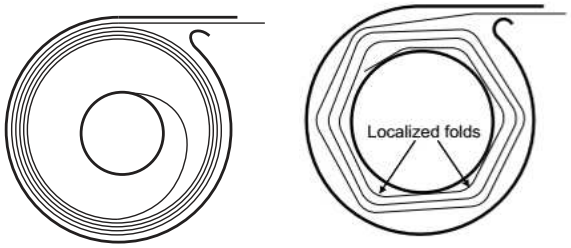

(a) Blossoming

(b) Buckling (adapted from [105])

Figure 3.24: Instabilities of a coiled shell.

i.e. the radius of its elastic folds. In particular, when $R/r < 1$ blossoming occurs, whereas $R/r \gg 1$ leads to buckling. The natural radius of a shell depends on its bending stiffness and geometry of the cross-section. For an isotropic tape spring, it corresponds to the radius of its circular arc cross-section [11].

These instabilities not only reduce the packaging efficiency of a coiled shell, but more importantly lead to severe loading conditions for the structure, which experiences regions of higher curvature than expected, and potentially jam the deployment mechanism. Therefore, a wide range of solutions has been proposed and demonstrated in recent years. In the simplest case, radial forces can be applied at discrete locations around the coiled shell, e.g. by using spring-loaded rollers [16][21]. This solution has been demonstrated on the deployment mechanism of the 4 diagonal booms of the LightSail-1 solar sail demonstrator [8], and it is often referred to as a "pusher" mechanism, as the uncoiling process is driven by a central motor that pushes the deployable boom out of the deployment mechanism.

Greschik [32] demonstrated an alternative approach to apply radial forces to a wrapped array, by using pairs of rollers on opposite sides of the portion of the array emerging from the coil. This generated a state of bending, with the root reaction applying the required stabilization force.

Others have explored the concept of tension stabilization, consisting of applying a tension at the free end of a coiled boom [105], as shown in Fig. 3.25b. The advantage of this method is to generate a uniform state of stress in the structure, which is more effective at suppressing buckling, compared to the previous concept. An implementation of the tension stabilization approach was developed by DLR [99][98], and is based on pairs of rollers "squeezing" the portion of a deployable

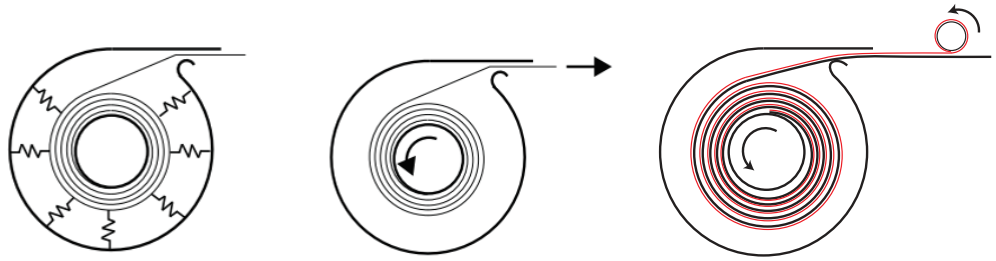

(a) Radial force stabilization (b) Tension stabilization (c) Pressure stabilization

Figure 3.25: Stabilization concepts for a coiled boom (Figs. (a) and (b) adapted from [105]).

boom emerging from the coiled region. One of rollers is driven by a motor, and its motion is transferred to the boom through friction, which causes a state of tension in the boom. An alternative approach to implement a "puller" mechanism consists of co-coiling the deployable boom with a narrow metal or Kapton strip [100] [69][21]. The strip is connected to the central hub at one end, and to a roller at the other end. The roller is driven by a motor, and a resisting torque is applied to the hub by a torsion spring or a power spring. As a result, the thin strip is under tension, forcing the deployable boom to conform to the hub. This concept, shown in Fig. 3.25c, has been demonstrated by DLR on the De-orbit Sail mission [95][89], and is currently being used by NASA [18] for NEA Scout and other upcoming solar sail missions.

3.7.2 Early Concepts of Deployment Mechanisms for Thin-Shell Space Structures

The first concept of a deployment mechanism for the space structure architecture considered in this chapter was proposed in 2016 by Arya et al. [4]. The concept, shown in Fig. 3.26a, was an extension of the radial force stabilization scheme in Fig. 3.25a to a 4-fold symmetric structure. In this concept, the structure was enclosed in a cage consisting of 8 rollers, which constrained it by applying radial forces. In some implementations, the rollers were spring loaded to maintain contact with the structure as it uncoiled. Coiling was performed manually, and uncoiling was driven by 4 linear actuators that pulled the ends of the structure along the diagonals.

While this concept was successfully demonstrated on a small-scale structure, it was later abandoned in favor of a centralized approach, where the uncoiling was driven from the center rather than from the diagonals, in order to make the design more

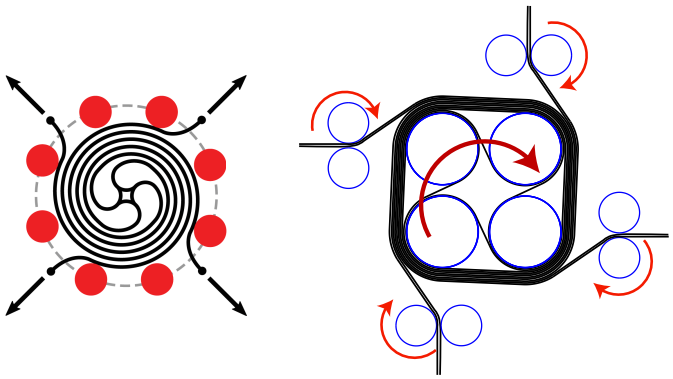

(a) Radial force stabilization concept (adapted from [3])

(b) Tension stabilization

Figure 3.26: Deployment mechanism concepts of a thin-shell space structure.

scalable. The radial force stabilization was also abandoned: its simple implementation came at the cost of non-uniform radial forces being applied to the structure, which could potentially harm fragile functional elements. Additionally, the radial force stabilization concept is effective at suppressing blossoming, but not necessarily buckling.

The second generation of deployment mechanisms was based on a tension stabilization scheme (see Fig. 3.26b), similar to the DLR implementation previously mentioned. In this case, each arm of the star shape was compressed between two rollers: one of them was idle, the other one was driven by an electric motor. The rotation of the driver roller applied tension to the structure through friction forces, controlling the uncoiling. Similar to the previous case, the coiling process was manual. This concept was very promising, as it could potentially solve the limitations of the first generation of mechanisms, but its implementation proved very challenging and unreliable, and it was only partially demonstrated on paper models and membranes. The main issue was that the stabilization constraints relied on friction between structure and rollers, which could greatly vary due to uncertainty in the friction coefficients, as well as to variations in the normal forces between rollers and structure, resulting from assembly and manufacturing tolerances. These challenges would often result in slipping between rollers and structure, with consequent loss of tension. These problems were exacerbated by the displacement control scheme used for the rollers: a single motor drove a central gear, which would then distribute the motion to the 4 driver rollers through a gear train. While this approach allowed to drive the mechanism with a single actuator, it was not able to compensate any

slipping between rollers and structure, which would gradually become more and more asymmetric during uncoiling, following a slipping event.

Informed by the lessons learned from the first two generations of mechanisms, a third concept was developed, and it is discussed in the next subsection.

3.7.3 Pressure Stabilization Concept

The deployment mechanism concept presented here is based on a pressure stabilization scheme. It is intended to apply uniform loading to the structure, similar to the tension stabilization approach, but using transverse forces like the first generation of mechanisms. This is achieved by co-coiling the structure with a thin membrane, subject to tension, similar to the "puller" mechanisms mentioned earlier on. Figure 3.27 shows a free-body diagram of this concept, in which the tension in the membrane is balanced by pressure loads on the deployable structure. This, in turn, is pushed on a rigid cylinder, conforming to its radius.

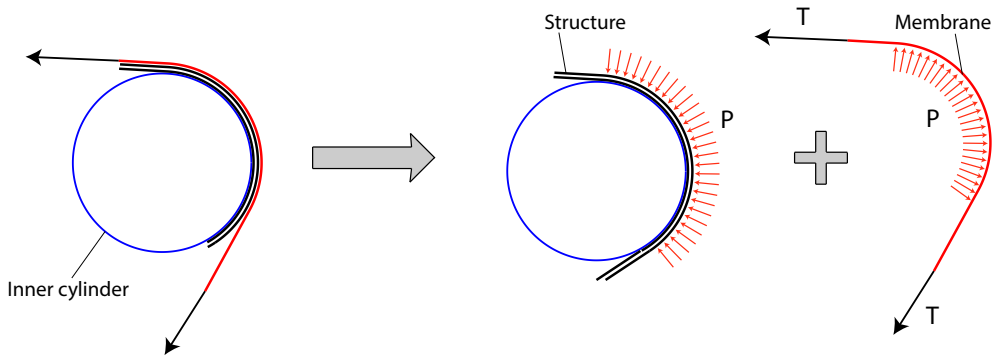

Figure 3.27: Free-body diagram of a portion of a structure co-coiled with a membrane under tension.

Figure 3.28 shows the concept of a deployment mechanism based on the pressure stabilization method. 4 inner cylinders support the structure, controlling the coiling/uncoiling process by rotating about a central shaft. Each inner cylinder is attached to a membrane, whose other end is connected to a fixed roller. Each roller applies a constant torque, which can be provided either by an electric motor or by a spring. This concept potentially solves some of the issues previously mentioned: by using force control rather than displacement control, each roller can independently adjust its speed such that the load on the membranes remains constant. This makes the mechanism insensitive to assembly imperfections (e.g. the membranes having different lengths) and capable of compensating external perturbations (e.g. a membrane becoming slack for any reasons), resulting in a robust design. Additionally,

applying tension to the membrane rather than to the deployable structure is highly desirable, as it reduces the risk of damaging any brittle functional elements mounted on it.

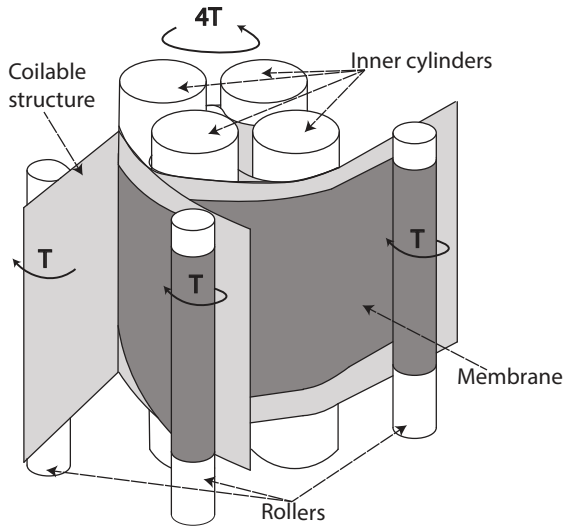

Figure 3.28: Pressure-stabilization concept to coil a 4-fold symmetric structure.

In order to allow the deployable structure to unfold to its deployed configuration, the deployment mechanism must open at the end of uncoiling, removing both the inner cylinders and the rollers. Various solutions had been devised for the previous versions of the mechanism: they all had the rollers hinged at their base, so that gravity would help their rotation after release, but they differed in the type of release mechanism. In the first generation, the rollers were held together by a thin string cut by hand, representing a burn-wire type of mechanism. In the second generation of the mechanism, the inner cylinders were pushed out of the inner cage by the deployable structure, at the end of uncoiling: this triggered a spring-loaded Hold-Down and Release Mechanism (HDRM), which would disengage the rollers from the top of the mechanism, allowing them to rotate about the hinges at their base.

In the concept proposed here, the mechanism would open in two steps, as shown in Fig. 3.29. During coiling, the inner cylinders are held in a inner cage, composed of a top and a bottom plate (orange in the figure), rotating with a central shaft. The plates have slots, which allow the inner cylinders to slide radially when they align with the rollers. When the structure is coiled, the inner cylinders are held in place by the membranes and the structure wrapped around them. At the end of uncoiling, though, the cylinders are free to move, and the tension in the membranes automatically extracts them out of the inner cage, once they are aligned with the

rollers (step 1 in Fig 3.29). In the second step, a release mechanism, placed at the top of the deployment mechanism, simultaneously releases 4 latches that hold the rollers in place. Upon release, the rollers rotate about their lower hinge, under the action of torsional springs.

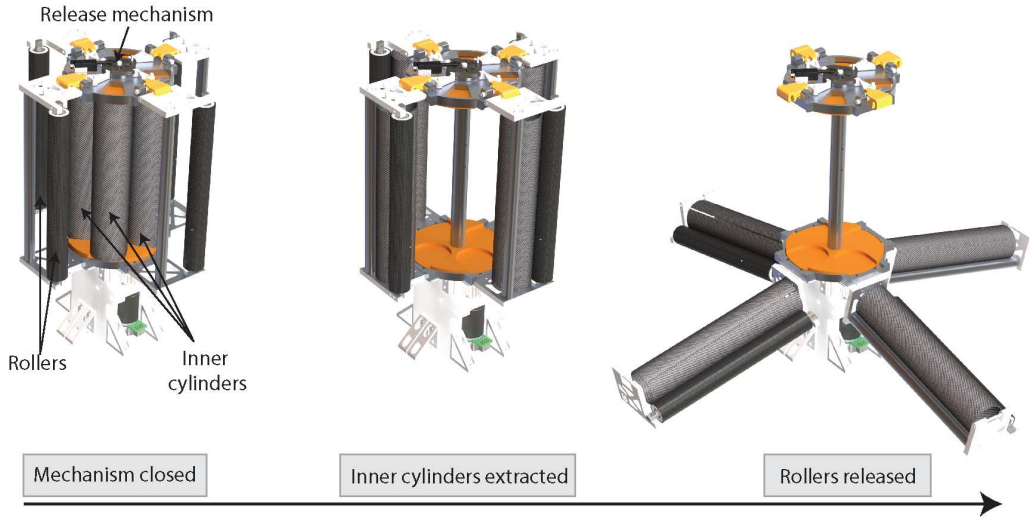

Figure 3.29: Design of the Mk IV deployment mechanism, based on the pressure stabilization approach (membranes are not shown here). The sequence shows the phases of the mechanism opening, at the end of uncoiling.

Figure 3.30 shows the implementation of the first deployment mechanism prototype based on the pressure stabilization approach. This prototype, named Mk IV, was the first full-scale active mechanism to coil a 1.7 m $\times$ 1.7 m thin-shell structural prototype (packageability had been previously demonstrated on a coiling apparatus turned by hand). The mechanism occupied a volume of 340 mm $\times$ 340 mm $\times$ 520 mm, and packaged the structure around 4 inner cylinders with a diameter of 63.5 mm, achieving a packaged cylindrical volume of 185 mm diameter $\times$ 250 mm height. The size of the inner cylinders was set by the maximum curvature that the longerons could tolerate, with a safety factor of 2.5.

The deployment mechanism prototype consisted of a 3D-printed plastic structure, reinforced by machined aluminum parts where needed, and off-the-shelf CFRP inner cylinders and rollers. The central stage was driven by a brushless DC motor, operating in closed-loop speed control. Each of the rollers was equipped with a brushed DC motor, controlled in closed-loop current control (as these motors have a linear relationship between current and torque). From a control standpoint, the central motor and the roller motors were decoupled: the former controlled the coiling/uncoiling process (both phases were automated), whereas the latter sensed

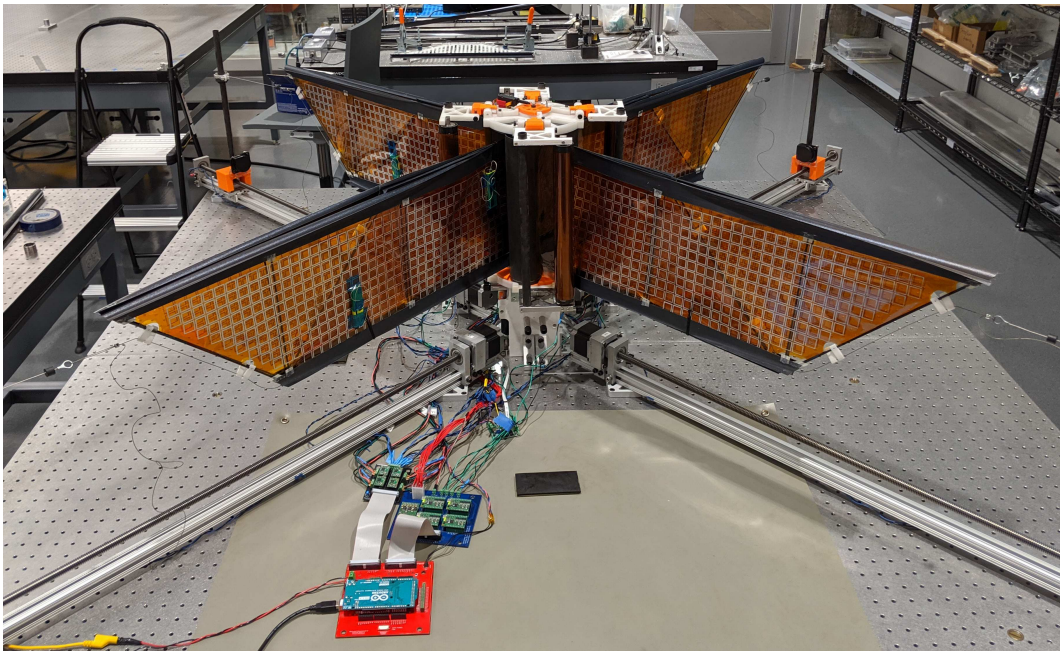

(a) Deployable structure in the star-folded configuration before coiling

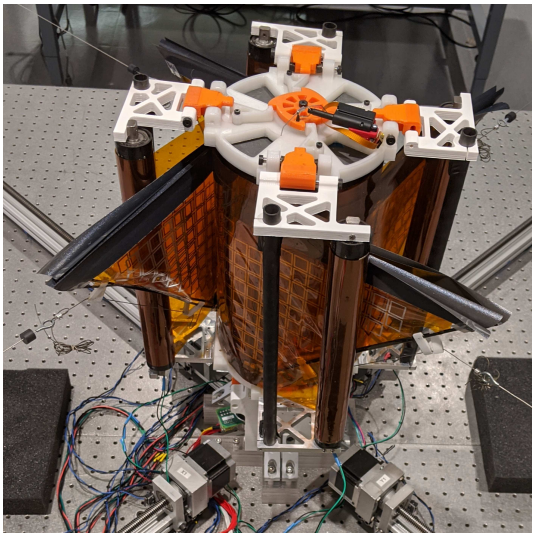

(b) Deployable structure partially coiled inside the deployment mechanism

Figure 3.30: Demonstration of a pressure-stabilized coiling mechanism with a 1.7m×1.7m space structure prototype.

the variations in the membrane tension due to the rotation of the central motor and automatically adjusted their speeds to return to their set value. The control loops for the central motor and the roller motors were built-in in the motor controllers, which were commanded through an Arduino MEGA. An additional linear actuator controlled the release mechanism to open the rollers.

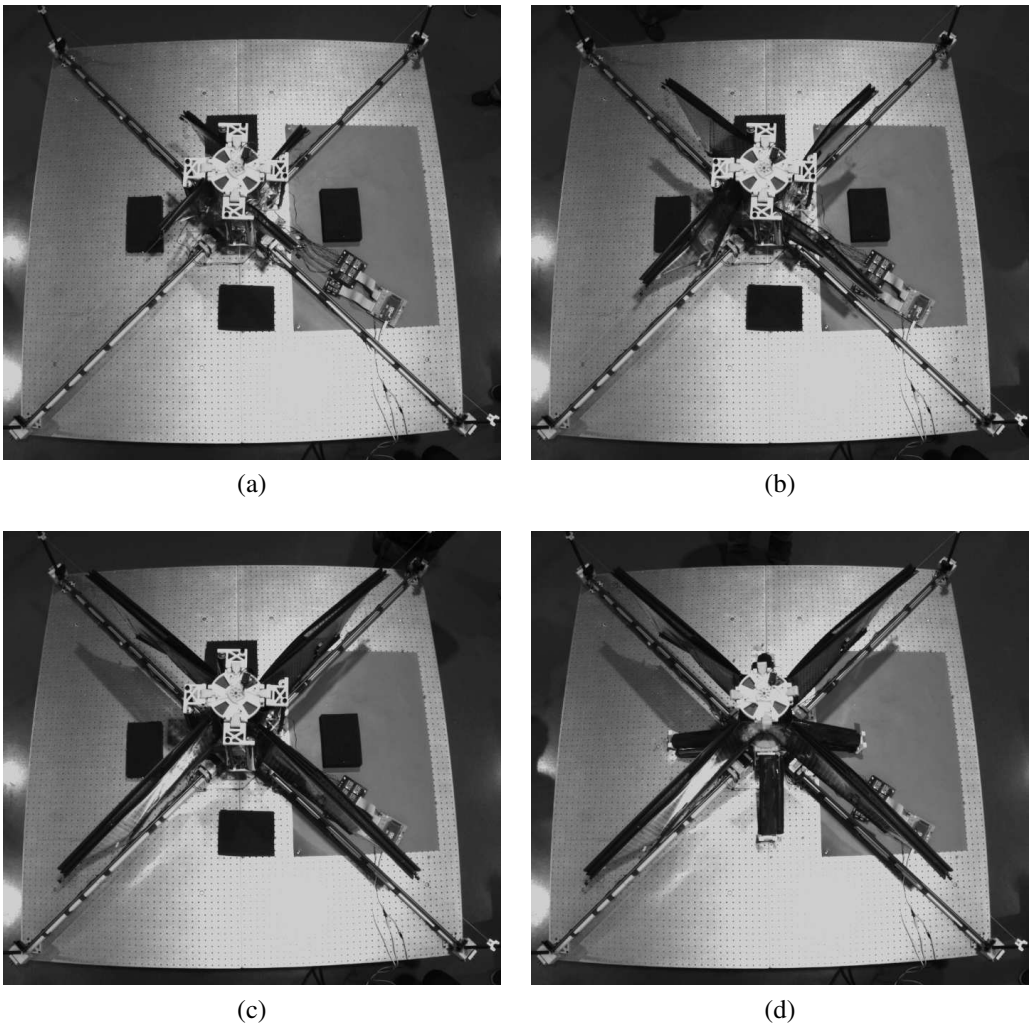

(a) (b)

(c) (d)

Figure 3.31: Snapshots of the uncoiling process for the structural prototype. From (a) to (c), the structure is uncoiled by the deployment mechanism; (d) shows the structure after the rollers and inner cylinders have been released. In this configuration, the structure is maintained in its star shape by hairpins.

It is worth highlighting that the choice of the actuation scheme represents a major difference between this mechanism and the "puller" mechanism concept developed for deployable booms. In the puller concept, the motor tensioning the membrane was also responsible for pulling the structure out of the coil, and the central hub would only apply a resisting torque. In our implementation, the structure is still pushed out of the coil by the central motor, and the driving and stabilization aspects are independent of each others. A key motivation behind this choice is that, if the 4 rollers were to drive the central hub in closed-loop torque control mode, variable torque would have to be provided to make sure that the mechanism would not stall

due to an increase in the resisting torque in the hub, requiring additional sensing and software complexity. If, on the other hand, closed-loop speed control was adopted, there would be no guarantee that the membranes had the same tension, falling in the same pitfall as the previous generation's mechanism.

Fig. 3.30 shows pictures of the deployable structure integrated with the deployment mechanism. The inner ends of the diagonal cords of the structure were attached to the central shaft of the mechanism; the other ends were attached to 4 tensioning systems, consisting of spring-loaded cord retractors. This allowed support to the structure at the end of deployment. Fig. 3.31 shows a sequence of snapshots from an uncoiling experiment. The structure, initially coiled, was quasi-statically extracted from the mechanism under the action of the central motor (the duration of this phase was about 5 minutes). When it reached the star shape (Fig. 3.31c), the inner cylinders were extracted, and the rollers were released on command (Fig. 3.31d).

Between 2019 and 2021, about 20 coiling/uncoiling experiments were successfully performed with this mechanism prototype, confirming the reliability of the pressure stabilization approach. A new iteration of the mechanism, based on the same principles of operation, but designed with launch survivability in mind, has been recently developed by the Space Solar Power Project team at Caltech, and it will be demonstrated in space in 2022 as part of the SSPD-1 mission, under the name of DOLCE (Deployment on-Orbit of an uLtralight Composite Experiment).

3.8 Staged Dynamic Deployment Concept

During the second phase of deployment, the deployable structure unfolds from the star shape to its planar configuration, driven by its stored strain energy. In its simplest implementation, the unfolding process is initiated by the release of the rollers in the coiling mechanism, and the square loops in the structure deploy at the same time. The dynamics of this process will be the main focus of the next chapter. Here, instead, we propose an alternative approach, consisting of a staged deployment scheme. In this case, the deployment path of the structure is broken down in smaller steps, so that the structure dynamically deploys between intermediate, known configurations. Such configurations are defined by releasable constraints that induce elastic folds at opportune locations, chosen from a desired kinematic path for the structure.

One of main advantages of this approach is that it provides some control over the deployment path of the structure, which is otherwise set by the direction of its steepest energy gradient. For large structures with many thin-shell components, multiple

energetically-similar paths are expected to exist, some of which might present local energy minima in which the structure can achieve static equilibrium without ever reaching its fully deployed state. Therefore, imposing intermediate checkpoints along the deployment process can mitigate the risk of incomplete deployment. Also, a staged deployment scheme would reduce the dynamics of the process, which could become excessively fast and chaotic for large structures, posing the risk of damaging any functional elements on it. Finally, a staged deployment reduces the deployment envelope of the structure, as it is shown below. This reduces the required clearance around the structure and the risk of contact with other components of the spacecraft during deployment, which can result in structural damage or incomplete deployment.

The effect of a staged deployment scheme on the deployment envelope can be investigated using the kinematic model of folding developed in Sec. 3.4.1. Here, we assume that each square loop follows the 4-fold symmetric path presented in Fig. 3.10a. Different square loops in the structure can be integrated as done for the folding case, but with different boundary conditions. In particular, during folding, it was assumed that the structure would lie on a flat surface, and that each square loop would sit on it if the length of the cords allowed it, or it would be lifted by an offset Δz otherwise. During deployment, the structure is suspended by diagonal cords, so that each strip is free to extend vertically in either direction. In this case, we assume that dynamic effects dominate over gravity, and that each portion of the cords between strips remains horizontal. Also, the outer strip-cord connector on the outermost strips are only allowed to slide horizontally, as shown in Fig. 3.32a, since they are aligned with the cord tensioning systems at the ends of the diagonals. Under these assumptions, the kinematics of the structure can be solved using the same framework implemented for the folding case, and its deployment envelope can be computed by tracking its highest and lowest points at each increment of the solution. Figure 3.32 suggests that the extreme points are located at the center of the two longest strips in the structure, which deflect upwards and downwards, respectively, as a result of Z-folding.

The example in Figure 3.32 plots the envelope of a structure with the 3 strips and $\hat{w} = 0.55$. For clarity, only the outermost 2 strips are plotted, as they contribute the most to the envelope. The trajectory of the 4 points at the center of the two strips is plotted in Fig. 3.32b. The difference between the maximum and minimum height of the structure during deployment can be used as a measure of the deployment

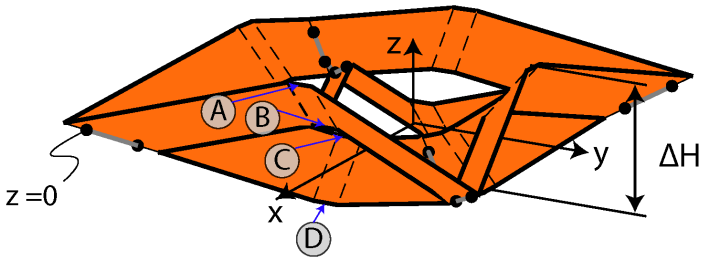

(a) Generic configuration of a structure during unfolding

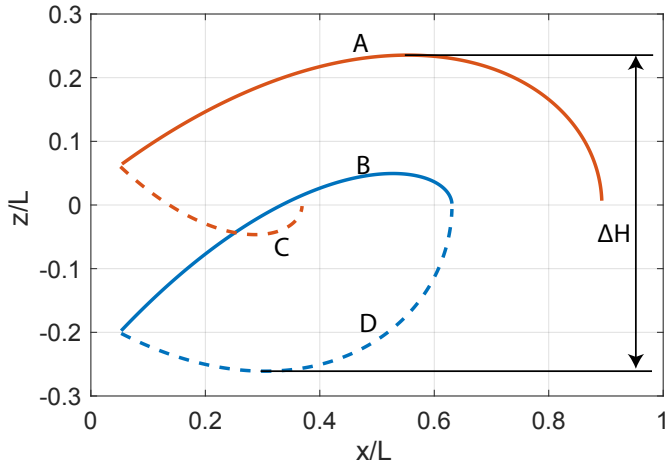

(b) Trajectory of the 4 points at the center of the outermost two strips

Figure 3.32: Example of deployment envelope for a structure with 2 strips deploying at the same time, and elastic folds located at $\lambda_1 = 0.1$.

envelope, and is defined here as ΔH. For given strip geometry, this distance is a function of the fold location λ. Figure 3.33 shows the envelope for structures of different sizes, as a function of λ. Each line was generated by adding strips to the same base design ($\hat{w} = 0.55$), so as to increase the overall size of the structure, and isolating the two outermost strips, which experience the largest height excursion. The plots show that the envelope is always greater than the width of the strips (black line), which is the theoretical minimum possible (as it corresponds to the space occupied by the strips in the star shape). Also, ΔH greatly increases as the folds approach the center of the strips. This effect is dramatically amplified as the structure gets bigger. For example, for a structure with 10 strips, having the folds at the center increases ΔH by almost a factor of 4, compared to having them at the ends. Also, it is interesting to note that, when $\lambda = \lambda_{max}$, the envelope is the same regardless of the number of strips.

These results have profound implications on the design of a deployment staging.

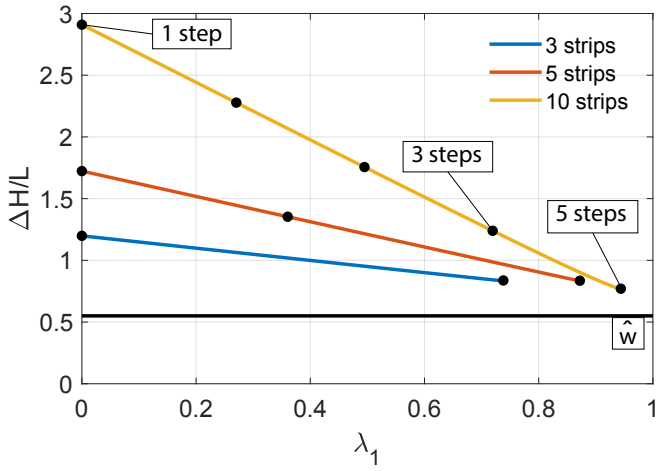

Figure 3.33: Maximum height of a structure with $\hat{w} = 0.55$ as a function of the fold location λ_1. Results are shown for different numbers of strips.

Indeed, we have previously shown that, in order to simultaneously fold/unfold several square loops, their elastic folds must have the same spacing. Therefore, the values of λ on the last 2 strips cannot be chosen arbitrarily, but only discrete values are possible, for which an integer number of strips is deployed at the same time. For each architecture, the admissible values of λ are indicated in Fig. 3.33 by the black circles. For example, a structure with 10 square loops can be deployed in 5 steps by releasing 2 square loops at a time, achieving the most compact deployment envelope. A 3-step process can also be conceived, by releasing 4 strips at each of the first 2 steps, and the remaining 2 strips in the final step. In general, increasing the number of strips being released in the first step increases the corresponding ΔH. Therefore, for large structures, a carefully designed staged deployment scheme can minimize the number of intermediate steps, while also achieving a sufficiently compact deployment.

Here, the concept of staged deployment is demonstrated on the 1.7 m$\times$ 1.7 m structural prototype, using the 2-step deployment sequence shown in Fig. 3.34. It can be noted that the sequence corresponds to the same kinematic path used for the folding process, but in opposite direction. Indeed, here the innermost strip is deployed in the first step, with the second and third strips deploying together afterwards.

To demonstrate this concept, the structural prototype was deployed starting from its star shape. The deployment mechanism consisted of a central shaft, to which the inner ends of the diagonal cords were attached, and 4 spring-loaded cord tensioning

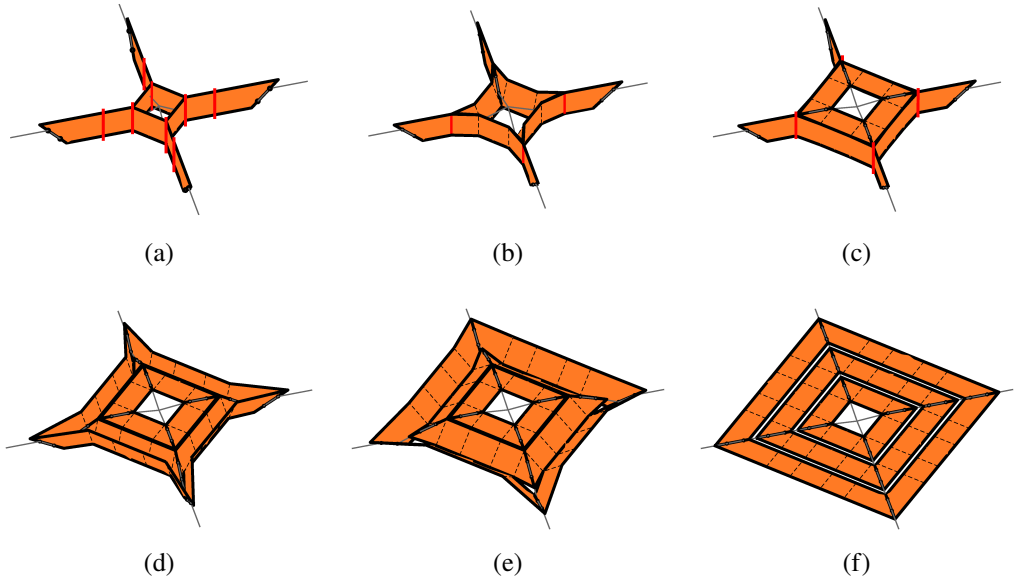

Figure 3.34: Deployment sequence from kinematic model for a 2-step deployment scheme with fixed folds. The red lines represent the localized constraints, which are simultaneously removed on the 4 arms of the star-shape. Dashed lines correspond to fixed localized folds. (a) to (c) shows the release of the first set of constraints, resulting in the deployment of the inner square. (d) to (f) shows the deployment of the middle and outer squares, following the release of the second set of constraints.

systems, placed outside the structure and aligned with the diagonals. Early deployment experiments used hairpins as releasable constraints, which were manually removed in a synchronized fashion. Later on, more sophisticated releasable devices were developed by the Space Solar Power Project team at Caltech. For the scope of this discussion, it will suffice mentioning that the devices were miniaturized burn-wire mechanisms, battery-powered and wirelessly controlled; they weighed about 5 g each and they were only 8-mm-thick, so as to be compatible with the coiling process. The devices were attached to the Kapton membrane of the outer strips, and holes were added to all the membrane at the location of the constraints to allow for a wire loop to run around the longerons on each arm of the star shape, holding them together.

Figure 3.35 shows the sequence of intermediate configurations during staged deployment of the structural prototype. In Fig. 3.35b, the structure is in its intermediate configuration, in which the inner square is fully deployed. The structure was mostly symmetric, although the spacing between folds on the upper longeron of the folded strips varied along each square loop.

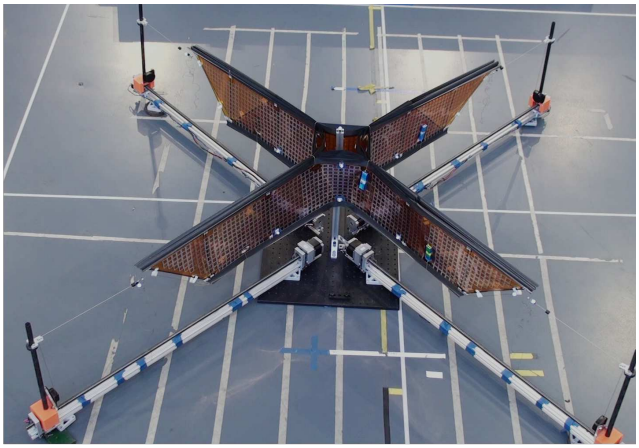

(a)

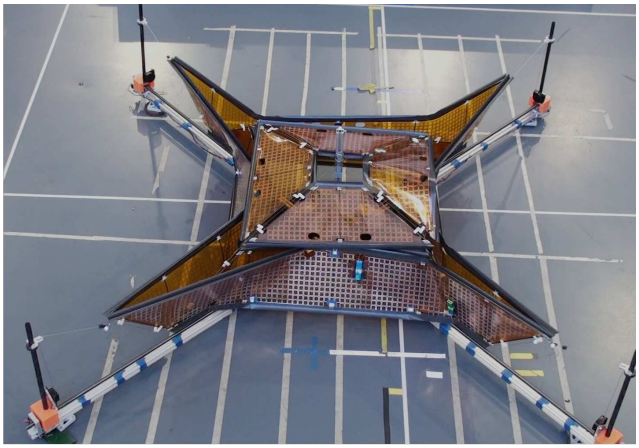

(b)

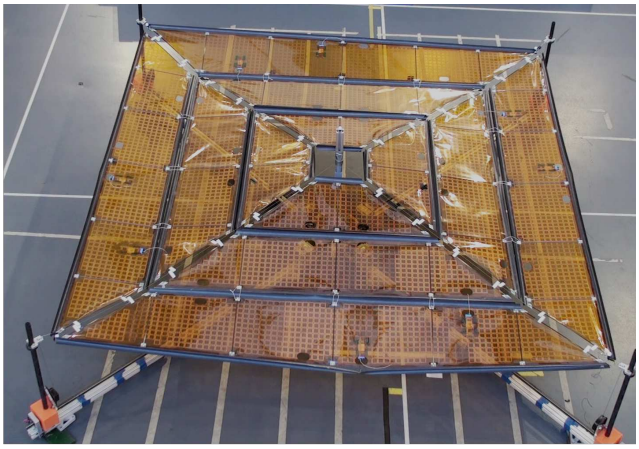

(c)

Figure 3.35: Demonstration of a staged deployment sequence on a 1.7 m $\times$ 1.7 m space structure prototype.

This resulted from the constraints being applied only to one of the longerons in each strip. It can be noticed that the distance between elastic folds on the remaining strips, still folded, varied across quadrants. This resulted from the constraints being applied only on one of the longerons at each location, therefore allowing propagation of the elastic folds on the other longeron. In the second step of deployment (Fig. 3.35c), the middle and outer squares successfully deployed, although gravity effects led to a sagged configuration of the structure, with some buckling in the longest strip (at the bottom of the picture).

Several experiments were performed using this approach, showing excellent repeatability of the intermediate configurations of the structure. The main challenge encountered had to do with the implementation of the release actuators not being sufficiently mature to guarantee reliable release of the constraints. Occasional failure to release caused incomplete deployment of the structure, highlighting the risk of introducing single points of failure in the deployment. Additionally, the release of the constraints on the 4 arms of the star shape at each step of deployment occurred in a sequential way, with a delay between each actuator of about 100 ms. While this delay did not appear to pose any risk for the deployment, it resulted in a non-symmetric deployment dynamics in between steps, making the process harder to quantify and predict using simulations.

Despite these challenges, the experiments confirmed the feasibility of a staged deployment approach, opening a pathway for the controlled deployment of large space structures, for which the uncertainty of deploying many thin-shell components together exceeds the risk associated with the additional failure points in the system.

3.9 Conclusion

This chapter has presented a methodology to package and deploy a space structure consisting of multiple thin-shell strips arranged in a square architecture. While the packaging concept had been previously demonstrated on membranes and small-scale simplified structures, here we have developed a framework that can be applied to large structures, and we have demonstrated it on a 2 m-scale structural prototype.

By imposing elastic folds at opportune locations, we have shown that the kinematics of the structure can be described by a kinematic chain consisting of rigid links connected by revolute joints. Using an algorithm previously developed for closed-loop mechanisms, a computational framework was implemented to define compatible kinematic paths for the structure, identifying a path for which a single-

degree-of-freedom mechanism can be achieved. This allows folding of the structure in a predictable and repeatable fashion and, most importantly, minimizes the internal stresses, reducing the risk of accidental damage to the structural components. An analysis of the boundary conditions of multiple, interconnected square loops revealed that the cords connecting adjacent strips impose constraints to the vertical motion of the strips during packaging. Folding the strips in pairs appears to be the best approach to package the structure in a sequence of simple steps, while minimizing the interaction between strips. It was also found that the design parameters of the space structure, i.e. the aspect ratio of the strips $\hat{w}$ and the spacing between strip-cord connectors $\hat{\eta}$, affect the kinematics of the structure, which should therefore be taken into consideration in the early stages of the design process. A mathematical foundation to studying kinematic paths with multiple degrees of freedom has been laid. This allows us to consider alternative folding schemes, in which a lower degree of symmetry and a less deterministic kinematics are accepted in exchange for a potentially easier-to-implement folding procedure. The case of mirror symmetry on a single square loop with 5 degrees of freedom has been presented as an example. More work has to be done to combine multi-degree-of-freedom folding schemes with structures composed of multiple square loops. Indeed, a 1 D.o.F. mechanism allows us to decouple the internal kinematics of the square loop (the relationship between its internal angles) and the external kinematics (its position with respect to the other parts of the structure), greatly simplifying the analysis. For the multi-degree-of-freedom case, the internal and external kinematics might have to be solved at the same time for the entire structure, as the cord length constraints would enter directly in the optimization algorithm for the direction of the solution increments.

A novel deployment mechanism concept to coil the space structure from a star shape to a cylindrical configuration was proposed and demonstrated. Inspired by existing concepts for deployable booms, a pressure stabilization approach was implemented to support the coiled structure during coiling, launch, and deployment, by co-coiling it with a thin Kapton membrane. Independent actuators for each membrane, operating at constant torque, provided reliable and robust operations, making the mechanism insensitive to misalignments and slipping in the membrane. Although the deployment mechanism prototype presented in this chapter used 6 actuators for maximum flexibility during operations, their number can be drastically reduced by switching to a passive roller design, in which pretensioning of the membranes is applied by spring-loaded rollers.

Finally, the concept of staged deployment was proposed to unfold the structure from the star shape to the deployed configuration. This idea offers a compromise between the simplicity of a strain-energy deployment approach and the reliability of an actively-controlled deployment. In fact, it allows us to guide the structure along a desirable deployment path using a small number of relatively simple release actuators. The advantage of this approach is two-fold: firstly, it reduces the uncertainty associated with the dynamic deployment of a large number of thin-shell components; secondly, it reduces the deployment envelope of the structure, allowing to integrate it with a spacecraft in a more compact package. While more work is required on engineering aspects of the implementation of the release devices, a staged deployment scheme might be the key to enabling the strain-energy deployment of large thin-shell structures for space applications.

Chapter 4

DEPLOYMENT DYNAMICS OF A THIN-SHELL SPACE STRUCTURE

4.1 Introduction

In the previous chapter, a thin-shell space structure architecture was presented, and its kinematics was investigated to design a safe and predictable packaging process. A staged deployment scheme was also demonstrated deploying the structure through a sequence of strain-energy deployment steps between intermediate, static configurations.

In this chapter, the unfolding process of the structure is investigated from a deployment dynamics perspective. Experiments and high-fidelity finite element simulations were used to characterize the evolution of the structure during a single-step deployment, initiated by the release of a deployment mechanism. For the purpose of this study, the Kapton membranes on the strips were omitted, reducing the space structure to its thin-shell skeleton.

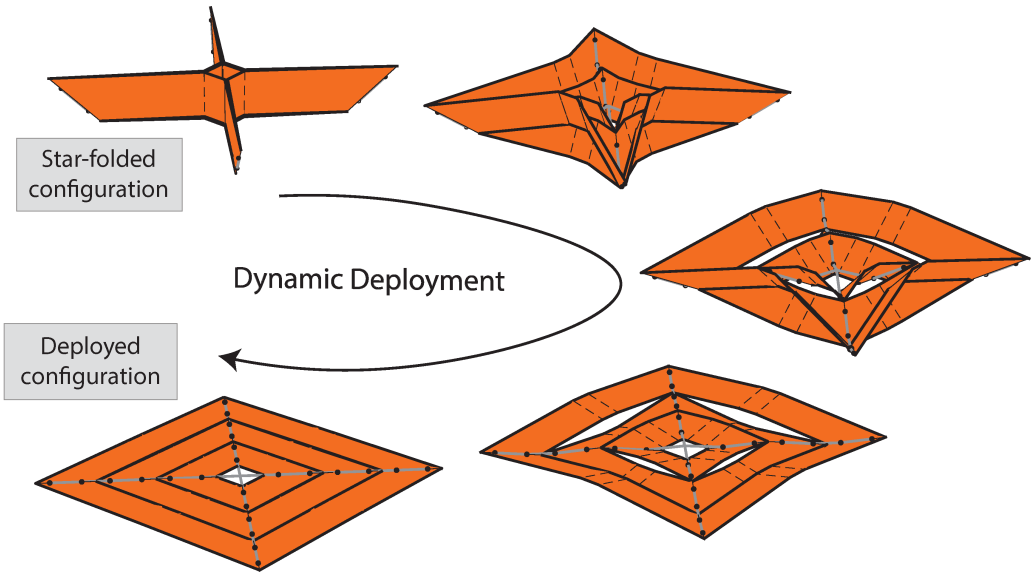

Figure 4.1: Concept of a single-step deployment process for a space structure with 3 strips per quadrant.

The chapter is organized as follows. In Section 2, the geometry of the space structure and the key features of the deployment mechanism are presented. Sections 3 and 4 describe the experimental setup and present the experimental results. In Section 5, the implementation of the finite element model is discussed. The results are compared with experiments in Section 6, where a typical behavior of the elastic folds on the structure is also presented. Finally, Section 7 discusses the results and concludes the chapter.

4.2 Problem Description

The space structure studied in this chapter is based on the architecture presented in Sec. 3.3, and it consists of 4 triangular quadrants, each composed by 3 trapezoidal strips. Its geometry is shown in Fig. 4.2, where its key geometric parameters are also defined. Their nominal values are reported in Tab. 4.1. The strips are based on the same design as the rectangular strip studied in Chapter 2; details about their components can be found in Sec. 2.3.1.

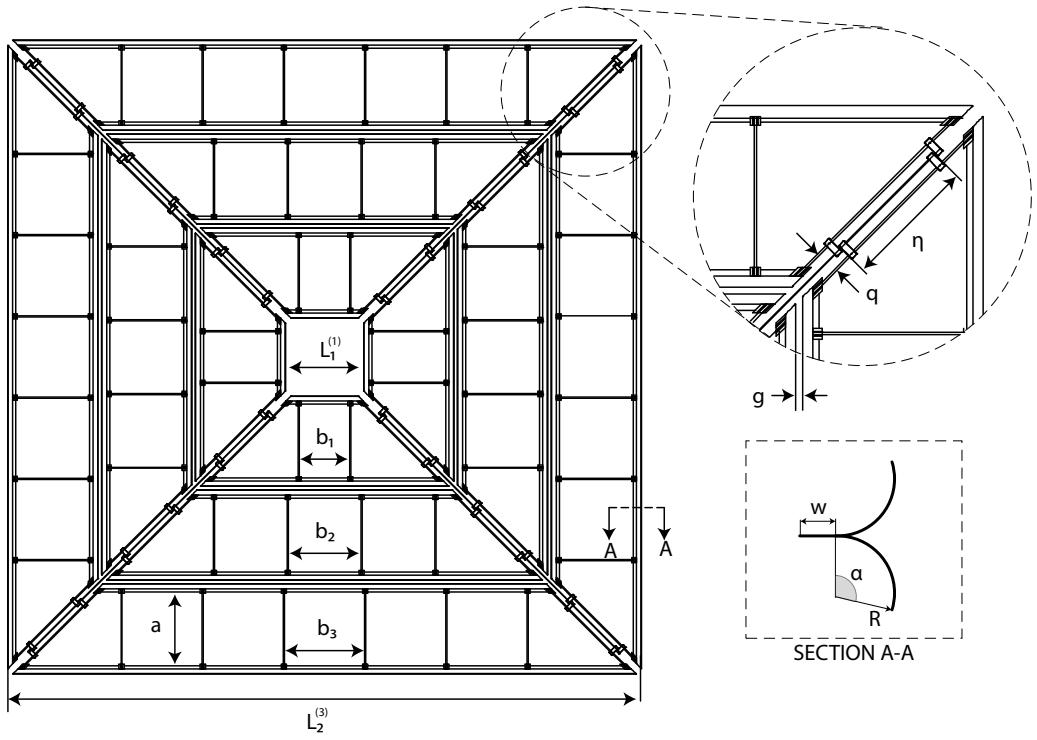

Figure 4.2: Geometry of the space structure prototype and main geometric parameters

Parameter	Value
TRAC flange radius	$R = 13.1$ mm
TRAC flange angle	$\alpha = 105°$
TRAC Web width	$w = 8.5$ mm
Inner length	$L_1^{(1)} = 217$ mm
Outer length	$L_2^{(3)} = 1677$ mm
Strip inner width	$a = 200$ mm
Batten spacing - Strip 1	$b_1 = 137$ mm
Batten spacing - Strip 2	$b_2 = 197$ mm
Batten spacing - Strip 3	$b_3 = 217$ mm
Strip-cord connector distance	$\eta = 180$ mm
Diagonal gap	$q = 20$ mm
Strip gap	$g = 10$ mm

Table 4.1: Geometric parameters of the space structure prototype

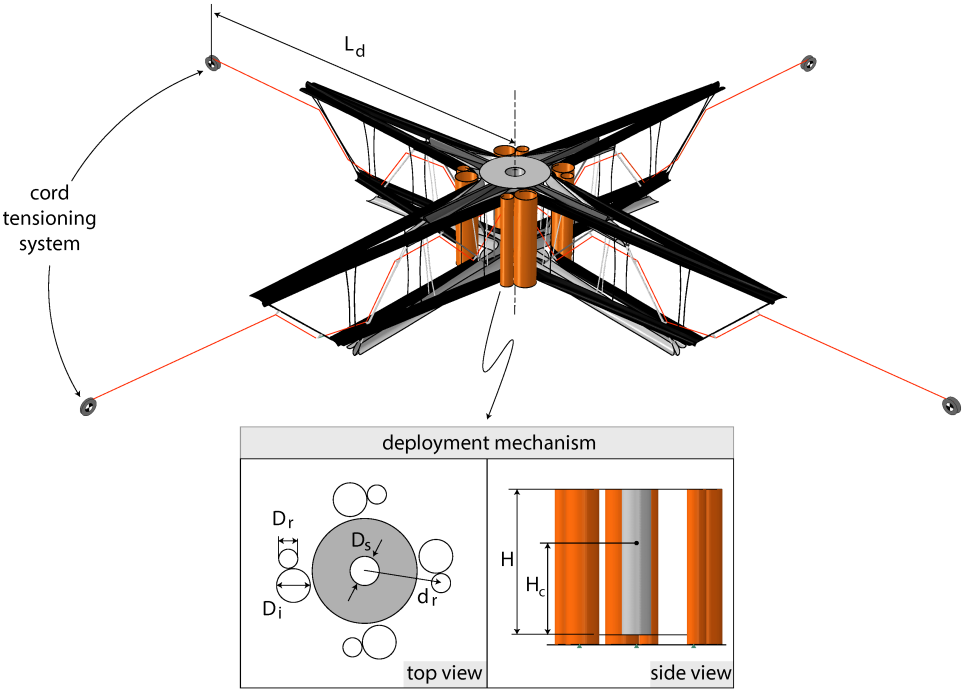

Figure 4.3: Schematics of the structure in its folded star shape, prior to deployment, and geometry of the deployment mechanism.

The space structure is initially folded in a star shape and is installed in a deployment mechanism, based on the architecture shown in Fig. 3.29. For the purpose of this study, the key features of the mechanism are its 4 roller arms, each containing a roller and the corresponding inner cylinder, to which it is connected through a Kapton membrane. Before deploying the structure, the inner cylinders are extracted from

their inner cage, and the roller arms are the only constraint preventing the structure from deploying. Each roller arm is connected to the top plate of the mechanism by a release actuator, and to the bottom plate by a hinge. Synchronized actuation of the release systems disengages the roller arms, allowing them to rotate about their hinge and initiating the deployment of the space structure. The diagonal cords of the structure are attached to the central shaft of the deployment mechanism on their inner ends, and to spring-loaded cord tensioning systems at the other end. This allows it to support the weight of the structure at the end of deployment. The key dimensions of the deployment mechanism are reported in Tab. 4.2.

Parameter	Value
Distance of cord tensioning system from central axis	L_d = 1400 mm
Central shaft diameter	D_s = 55 mm
Roller diameter	D_r = 36 mm
Inner cylinder diameter	D_i = 63.5 mm
Distance of the rollers from the central axis	d_r = 146 mm
Height of the mechanism	H = 275 mm
Height of cord attachment	H_c = 191 mm

Table 4.2: Geometric parameters of the deployment mechanism

4.3 Experimental Setup

The deployable structure for the experiment, shown in Fig. 4.4, was an implementation of the design in Fig. 4.2. The structure was first star-folded by hand, following a 2-step approach similar to the one presented in Chapter 3, and then integrated in the deployment mechanism prototype, shown in Fig. 4.5. The details of the deployment mechanism are outside the scope of this discussion; the main features for the deployment are the roller arms with their release mechanisms and the cord tensioning system.

The release of the roller arms was controlled by 4 TiNi^{TM} ML50 Micro Latches, shape memory alloy-based release actuators, powered in parallel to provide synchronous release of the rollers. Each cord tensioning system consisted of a ML4575-13 cable reel, manufactured by Almark Enterprises Inc.. The reels contained a power spring, retracting a 0.5 mm-diameter stainless steel cable. The cable spooling from the retractor passed through a miniature nylon pulley with a ball bearing (same model used for the suspension system of the strip in Chapter 2), before engaging with the outer end of a diagonal cord on the deployable structure. A carbon fiber rod supported the pulley, setting the height of the cord at the same height as the

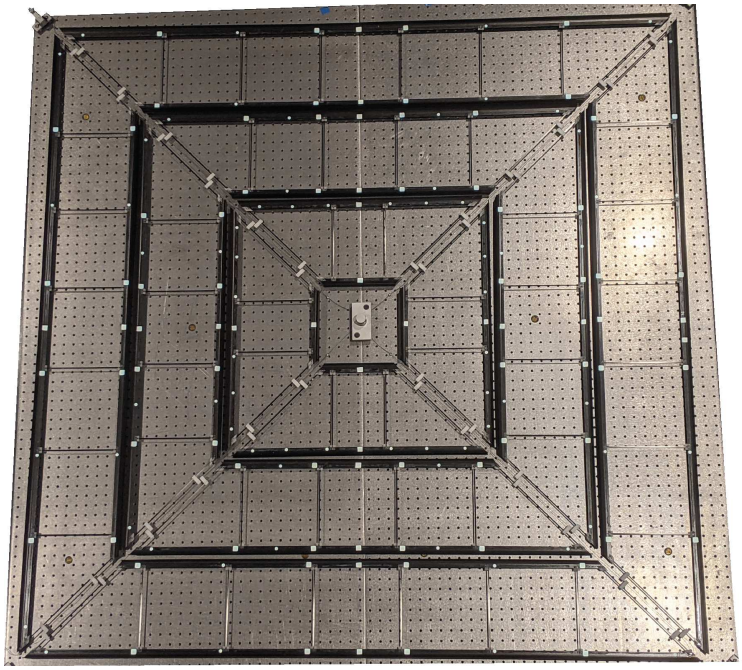

Figure 4.4: Space structure prototype.

cord attachment on the central shaft of the mechanism. The rod was mounted at the end of an 1.2 m-long T-slotted aluminum frame, oriented along the diagonal of the structure, and acted as a surrogate of a deployable boom for a flight mechanism.

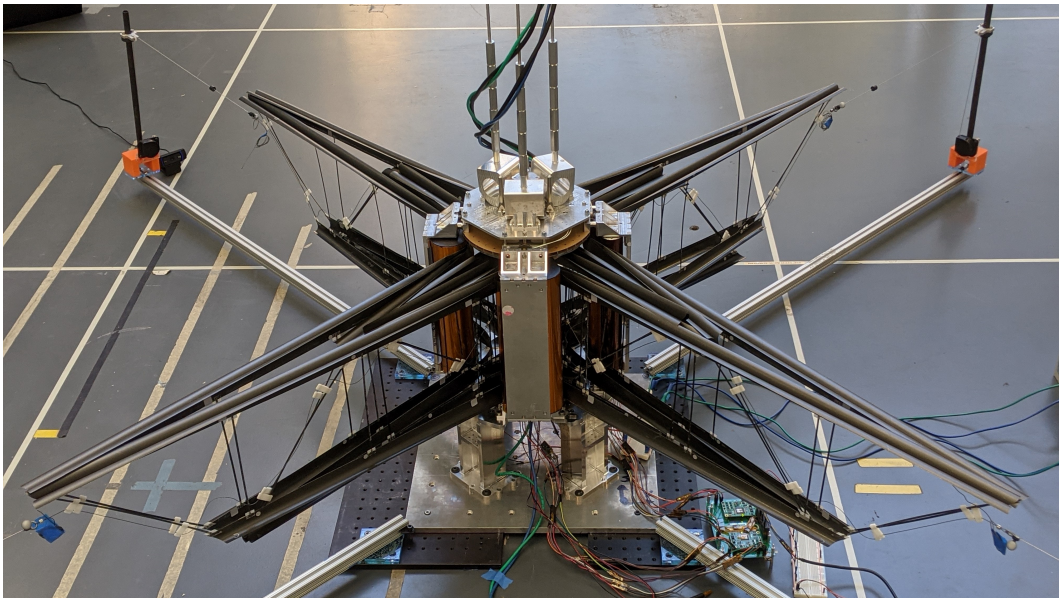

Figure 4.5: Folded space structure, integrated with the deployment mechanism prototype.

4.3.1 Metrology System

In Chapter 2, Digital Image Correlation (DIC) was proposed to extract full-field displacement data from deployment experiments of a single strip. This method, in combination with a dedicated shape reconstruction algorithm, allowed us to identify and track the elastic folds in the structure, accurately measuring their location and angle. Despite its undeniable advantages, preliminary deployment experiments, carried on an earlier prototype of the space structure, highlighted the limitations of DIC for this type of problems. For example, the large field of view (and consequent pixel size) required to capture the entire structure resulted in speckles approximately as large as the width of the longeron cross-section, leading to poor resolution in the transverse direction. The large 3D translations and rotations of the strips prevented following the speckle pattern for the majority of the deployment process, resulting in incomplete data, especially in the early phases of the deployment. Furthermore, DIC required significant preparation of the test structure, which was painted with a black background (to avoid glare from the glass fiber ply of the composite longerons) with hand-painted white speckles on it.

Therefore, a different metrology system was chosen for the deployment experiments presented in this chapter, using motion capture techniques. The experiments were carried out in the aerodrome of the Center for Autonomous Systems and Technologies (CAST) at Caltech, which is equipped with an OptiTrack motion capture system, consisting of 47 Prime^{X} 41 cameras, distributed along the perimeter of the test area. The cameras can track the position of retroflective markers, which reflect back at the source the infrared light emitted by each camera. This information is used to measure the 2D position of the markers on each camera sensor. Then, the data from all the cameras is combined, in real-time, by the Motive software, which reconstructs the 3D position of the markers.

Although motion capture only provided information at discrete points on the structure, offering lower spatial resolution compared to the full-field DIC measurements, it provided superior quality of the data. Indeed, the large number of cameras distributed around the structure allowed us to track points on all the strips at the same time, and the quality of the data did not suffer from out-of-plane displacements. Also, its real-time coordinate reconstruction capabilities drastically reduced the post-processing time required to extract the coordinates of the points, compared to photogrammetry, which tends to be a much more involved process.

For the deployment experiments, only 7 cameras were chosen, operating at 180

frames per second. 208 retroflective markers were distributed on both faces of the space stucture prototype, to provide sufficient spatial resolution. Although spherical markers provided, in general, better tracking performances, they would not allow the structure to be coiled; therefore, flat flexible markers were used, combining 6 mm-diameter circular markers and 8 mm × 8 mm square markers. The 3D coordinates of the markers provided by Motive were exported and processed in MATLAB, using the shape reconstruction algorithm described later in this chapter.

4.4 Characterization of the Experimental Setup

The dynamics of the roller release and the cord tensioning system were characterized experimentally to calibrate the numerical model. The experiments are presented in the following subsections.

4.4.1 Deployment Mechanism

The characterization of the deployment mechanism consisted of dry runs of the release of the roller arms, which were tracked by the motion capture system. The objective was to assess the synchronization of the release of the 4 roller arms, and to measure their rotation over time, in order to estimate the friction in the system. Figure 4.6 shows a schematic of the experiment, with the marker locations indicated by red and green circles. Two markers were placed on the hinge axis of each roller (green circles in Fig. 4.6) to identify the axis of rotation $t_i = A_iB_i/\|A_iB_i\|$ of the i-th roller. Several markers were placed at the top and on the sides of each roller assembly. Although a single marker per roller would have been sufficient to measure its rigid-body motion, the redundant markers provided more accurate data. The normal n_{ij} to the axis of rotation t_i passing through a point on the roller $P_j^{(i)}$ was computed as:

$$A_iP_j^{(i)}|_n = A_iP_j^{(i)} - (A_iP_j^{(i)} \cdot t_i)t_i \tag{4.1}$$

$$n_{ij} = \frac{A_iP_j^{(i)}|_n}{\|A_iP_j^{(i)}|_n\|} \tag{4.2}$$

Therefore, the rotation of the point about the hinge axis was computed as:

$$\phi_{ij}(t) = \cos^{-1}(n_{ij}(t) \cdot n_{ij}(t_0)) \tag{4.3}$$

At each time increment, the angle of each roller was obtained by averaging the computed angle on each of its markers.

To calibrate the system, a simple analytical model was derived to describe the dynamics of the roller, whose free-body diagram is shown in Fig. 4.6b. The equation

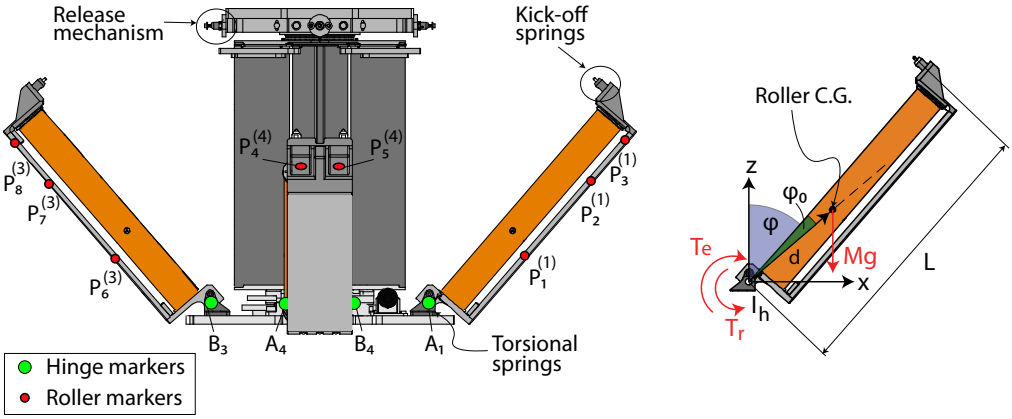

(a) Experimental setup (b) Free-body diagram of a roller

Figure 4.6: Experimental verification of the deployment mechanism. Retroflective markers are placed on the hinge lines (green circles) and on the rollers (red circles).

of motion for this 2D problem is the following:

$$Mgd\sin(\phi+\phi_0)+T_e-T_r=I_h\ddot{\phi} \tag{4.4}$$

where T_e and T_r are the elastic and friction torques, respectively, and ϕ_0 is the angle of the line between the hinge point and the C.G. location, measured from the z-axis when the roller is closed. The elastic torque accounts for the contributions from the torsional springs in the hinge, as well as from the kick-off springs at the top of the mechanism (converted in equivalent torsional springs). The nominal stiffness and initial torque of the springs was used for this calculation. Moreover, the mass properties of the roller (mass M, second moment of inertia about the hinge line I_h, and C.G. location) were extracted from its CAD model. The friction torque T_r was obtained from calibration, through a non-linear optimization algorithm (*fminunc* in MATLAB) that minimized the function

$$J=\sum_{i=0}^{N_t}(\phi_{an}(t_i)-\phi_{exp}(t_i))^2 \tag{4.5}$$

where ϕ_{an} and ϕ_{exp} are the analytical solution and the experimental measurements, respectively. The analytical solution was obtained from numerical integration of the equation of motion Eq. 4.4, using the *ode45* solver in MATLAB, for given friction torque T_r.

Figure 4.7 plots the results from the calibration. The solid black line corresponds to the average of the experimental results from 12 sets of data (4 rollers over 3

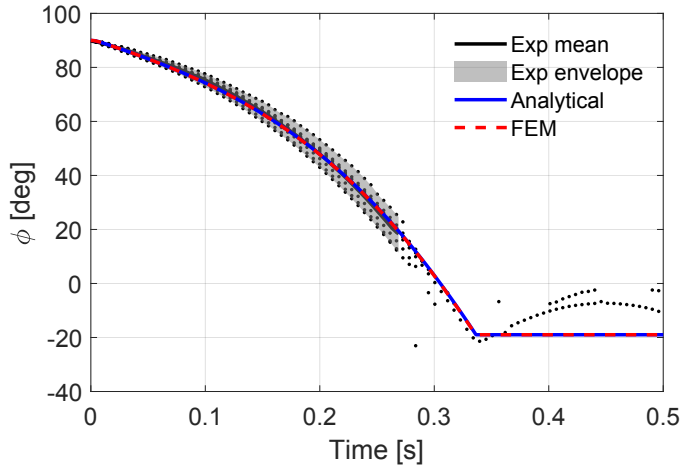

Figure 4.7: Comparison between experiments and simulation for the calibrated model of the mechanism.

experiments), shifted in time to remove the effect of delayed release of the rollers. The shaded grey region represents the envelope of the experimental results. The blue line is the result from the calibrated analytical model, using the optimal friction torque $T_r = 319.4$ Nmm. The same value was used in the finite element model of the roller (described in Sec. 4.7.3), showing exact agreement with the analytical solution). The results show that the rollers take about 320 ms to reach their final angle $\phi_{max} = -109°$. After this point, the analytical and numerical model assumes that the rollers lock at their maximum angle, whereas the experiments show that the rollers bounce back by about 15° before returning to their final position. The synchronization in the release of the rollers was also assessed: for the 3 experiments, the mean delay between rollers was 29 ms, with a maximum delay of 90 ms between the release of the first and last roller.

4.4.2 Suspension System

The suspension system was characterized through static tests (to measure the tension in the cables and the stiffness of the power spring) and dynamic tests (to quantify its friction). Fig. 4.8a shows the simple experimental setup for the static test: the tensioning system was clamped at its base, and the end of its cable was attached to a Mecmesin CFG$^+$50 digital force gauge, with a resolution of 0.05 N. The cable was initially extended to the maximum length of interest (about 900 mm) and the force was measured with 25 mm-increments, in the unloading direction (to simulate the conditions encountered during unfolding experiments). The results from the experiments on each cord retractor are reported in Fig. 4.8b, where circles

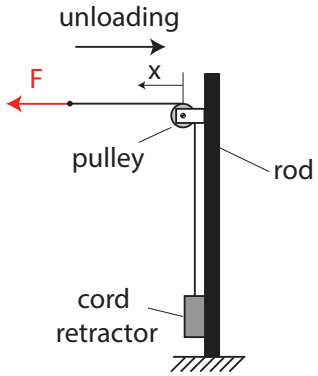

(a) Experimental setup

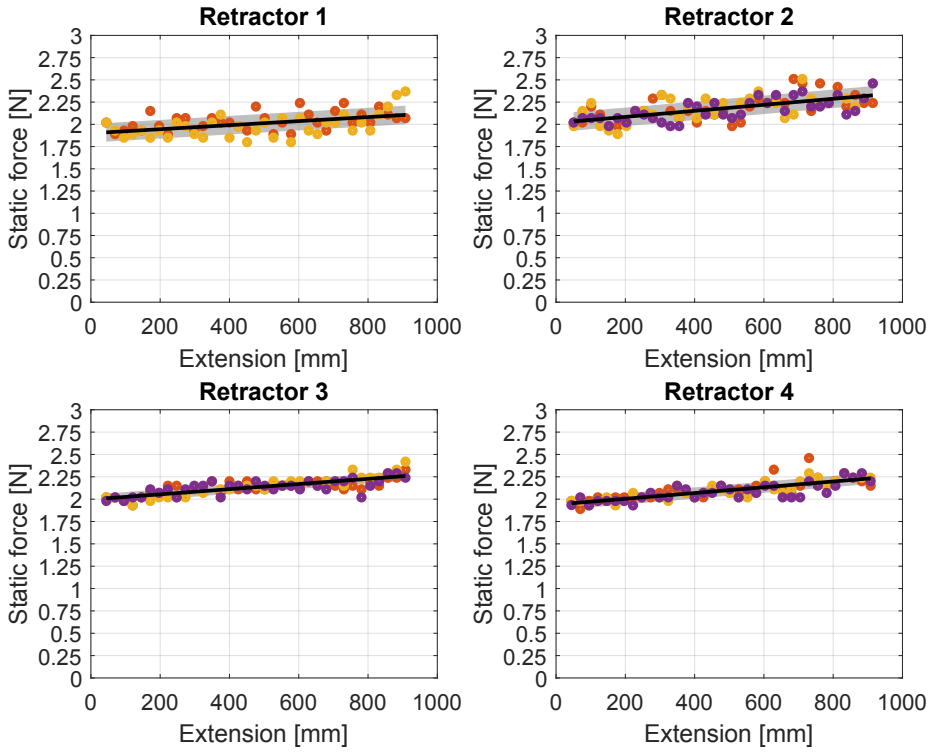

(b) Experimental results

Figure 4.8: Static characterization of the cord tensioning system.

of different colors correspond to different runs of the same experiment. The results showed consistently a repeatable behavior, consistent across different cord retractors. A linear fit was used to extract the initial force F_0 and the stiffness of the spring K for each retractor; the results are reported in Tab. 4.3.

Figure 4.9a shows the experimental setup for the dynamic characterization of the cord tensioning system. The base of the rod was clamped and a mass M was

Retractor ID	$K\ [N/m]$	$F_0\ [N]$	$\sigma\ [N]$
1	0.227	1.90	0.104
2	0.339	2.02	0.104
3	0.289	2.00	0.054
4	0.323	1.94	0.063

Table 4.3: Measured elastic properties of the 4 cord retractors.

attached to the end of the cable. The mass, initially held stationary by hand, was instantaneously released, accelerating upwards (along the z-axis) due to the tension in the cord. A circular target was placed on the mass, and a stereo high speed camera system (consisting of 2 Photron UX100 cameras) acquired monochrome images at a frequency of 1000 frames per second. The images were analyzed through photogrammetry, using the VIC3D software by Correlated Solutions, to extract the coordinates of the marker over time. The experiments were performed for 2 different masses (50 g and 100 g) and for each cord retractor, and repeated 3 times each. The friction in the system was estimated with the same approach used for the deployment mechanism, in the previous subsection. The equation of motion of the mass can be written as:

$$F_0 + K(H_0 - z) - Mg - \frac{T_f}{R_r} = \left(M + \frac{I_p}{R_p^2} + \frac{I_r}{R_r^2} \right) \ddot{z} \tag{4.6}$$

where F_0 and K are known from the static characterization, R_r and R_p are the radius of the power spring and the radius of the pulley, respectively, and T_f is the effective friction torque of the system, applied to the cord retractor.

Using the same approach previously described for the calibration of the deployment mechanism, a non-linear optimization algorithm was used to find the value of T_f^* that minimized the deviation of the analytical solution from the experiments, for both masses tested. The analytical model was solved with the *ode45* numerical solver in MATLAB, while the experimental data were represented by a third-order polynomial fit of the combined data from the experiments. Figure 4.9b reports the results for the two test cases, with the grey region containing the envelope of the experimental data, and the black solid line corresponding to its 3rd order polynominial fit. The red line corresponds to the analytical results, which is in very good agreement with the experiments for the 100 g-mass case, while it predicts a slightly faster dynamics for the 50 g case. This error shows that, in reality, the friction torque is not exactly constant. This is not surprising, as the largest source of dissipation is the friction between the spires of the power spring. The normal force between adjacent spires

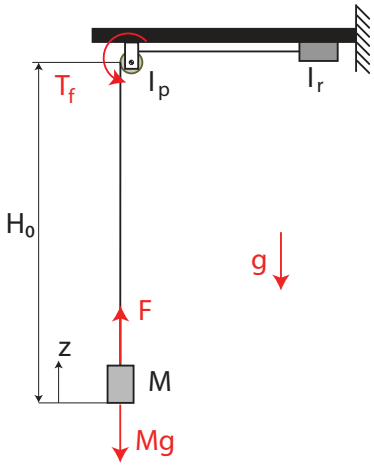

(a) Experimental setup

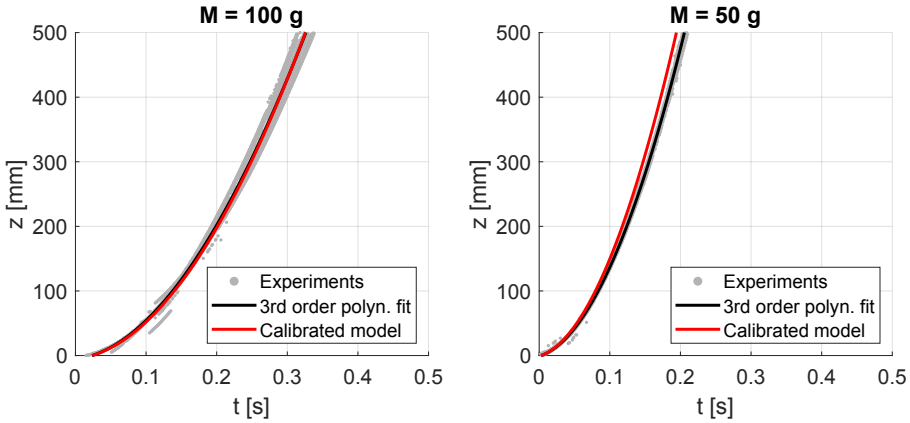

(b) Experimental results

Figure 4.9: Dynamic characterization of the cord tensioning system.

depends not only on the pre-stress in the spring, but also on the centrifugal forces resulting from its motion, therefore explaining the dependency of the friction torque on the velocity. For the purpose of the present study, a higher level of granularity in the description of the dynamics of the cord retractor was not deemed necessary, and therefore the assumption of constant friction torque was accepted, as a first order approximation of the physical system.

4.5 Shape Reconstruction Algorithm

The output from the motion capture system consisted of a point cloud containing, at each time frame, the coordinates of its points, identified by a unique ID. The point cloud was processed to reconstruct the shape of the strips and extract quantitative data from the deployment test. The algorithm consisted of the following steps:

1. Marker identification: the points in the point cloud were manually assigned to the corresponding marker on the structure. This process allowed identification of points with different IDs, but representing the same physical location on the structure. This happened, for example, when markers were placed on the two faces of a longeron, but at the same location, to extend the traceable range of motion of the point. Unassigned points were discarded to filter out ghosts, i.e. points generated by reflections or by uninteded bodies in the tracking volume.

2. Data stitching: data from points corresponding to the same physical location were combined. Averaging was performed when multiple data was available for the same time increment, and outliers were identified using a median filter and discarded. An example of this process is shown in Fig.4.11.

3. Angle calculation: for each strip, the markers on each longeron were classified in left and right markers, depending on their position relative to the center of the strip, as shown in Fig. 4.12. The tangent to each side was computed through the Principal Component Analysis (PCA), and was defined by the direction associated with the largest eigenvalue of the covariance matrix. The angle of the elastic fold in the strip was simply obtained from the dot product of the tangents to the two sides of the strip, as follows:

$$\theta_i = \text{sign}(n \cdot (t_i^R \times t_i^L)) \cos^{-1}(t_i^R \cdot t_i^L) \tag{4.7}$$

where the first term on the right-hand side is used to discern positive and negative angles of the folds. The inclination of the center of the strip α from the horizontal plane can also be computed as:

$$\alpha = \sin^{-1} n_z \tag{4.8}$$

where n_z is the z-component of the vector n.

4.6 Experimental Results

A sequence of configurations of the structure during a deployment experiment is shown in Fig. 4.13. The pictures show that, immediately after the release of the rollers, the outermost strips of the structure moved upwards through the gap between the rollers and the top plate of the mechanism (Fig. 4.13b). Contact between the middle strips and the lower edge of the rollers kept the rest of the structure constrained inside the mechanism until the rollers were fully deployed (Fig. 4.13e). Meanwhile,

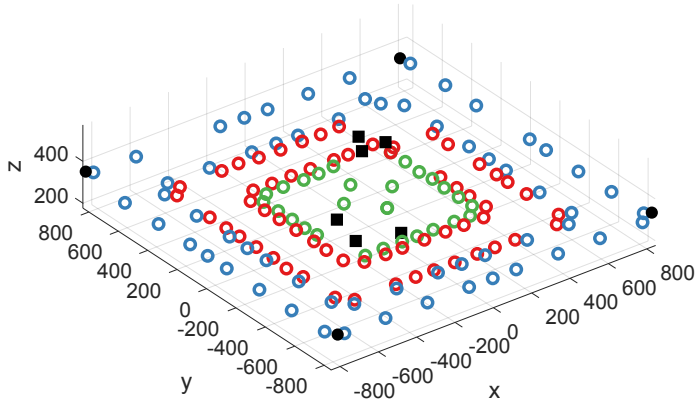

Figure 4.10: Point cloud at the end of deployment. Green, red, and blue circles correspond to points on the 3 strips. Black squares are points on the deployment mechanism.

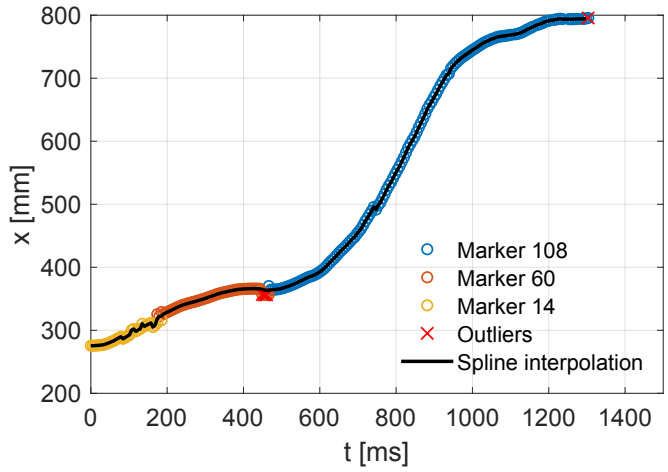

Figure 4.11: Example of data stitching for a marker on the structure, by combining different points in the point cloud.

the outer strips, constrained by the cords with the middle strips, rotated about their inner strip-cord connector, aligning their diagonal battens with the cords from the tensioning system (Fig. 4.13e). After that, the middle strips started sliding on the surface of the roller (Fig. 4.13e), while the outer strips continued their deployment, opening the angle of their folds. In Fig. 4.13g, the inner strips were fully deployed, while the middle and outer strips were still deploying, creating a peculiar diamond-shape. Finally, Fig. 4.13h shows the structure in its final, deployment configuration.

The distance of the corners of the strips from the center to the structure (R in

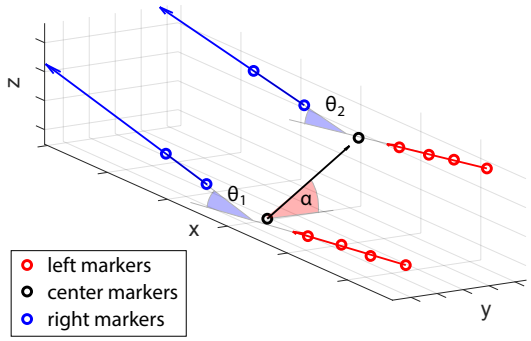

Figure 4.12: Calculation of the angle of the elastic folds on a strip.

Fig. 4.14) can be used to describe quantitatively the deployment process, as this distance is related to the maximum deployed size of the structure. Figure 4.15 plots the distance R for the 4 corners of the structure, measured by tracking the position of 6 mm-diameter spherical markers attached to the diagonal cords, at the end of the structure. The location of the central axis, from which R was computed, was set by fixed markers placed on the top plate of the deployment mechanism. At the time $t = 0$, defined as the time at which the first roller was released, the mean distance R was 929 mm, with a maximum variation of 24 mm between two corners. After release of the rollers, the distance monotonically increased over time in a symmetric fashion, reaching its final value $R = 1185$ mm after 690 ms.

Figure 4.16 shows the evolution of the mean angle of the elastic fold on the outermost strips for each longeron, indicated by θ_1 and θ_2 in Fig. 4.14. The angles were computed through the shape reconstruction algorithm presented in Sec. 4.5. No data was available at the beginning of deployment, when many of the markers were shaded by the deployment mechanism and the opening rollers (at least 4 markers per longeron are needed to compute the angle). The first available data point on longeron 2 was at $t = 95$ ms, when the angle of the fold was $\theta_2 = 82°$. The angle decreased monotonically until becoming zero for $t = 724$ ms. After this point, 3 of the 4 longerons latched in their deployed state, while one of them overshoot, buckling in the other direction before latching. The orange line shows the evolution of the mean angle of the fold on longeron 1: in this case, no data was available before $t = 410$ ms, since the markers on the outer face of the longeron were rotating downwards as the strip unfolded, whereas the markers on the inner face, located in the valley fold of the Z-folded quadrant, were not visible from the cameras until the quadrant had sufficiently opened. The available data, starting from $\theta_1 = 62°$ show a very similar trend as for the other longeron, with the deployment time being

(a) (b)

(c) (d)

(e) (f)

(g) (h)

Figure 4.13: Snapshots from deployment test.

approximately the same, and one of the elastic folds overshooting at $\theta_1 = 0$.

Another quantity of interest for the deployment process is the trajectory of the center of the strips, where the highest and lowest points during deployment were observed. Figure 4.17 shows both the distance from the central axis and the height of the markers at the center of each longeron, averaged over the 4 quadrants. At the

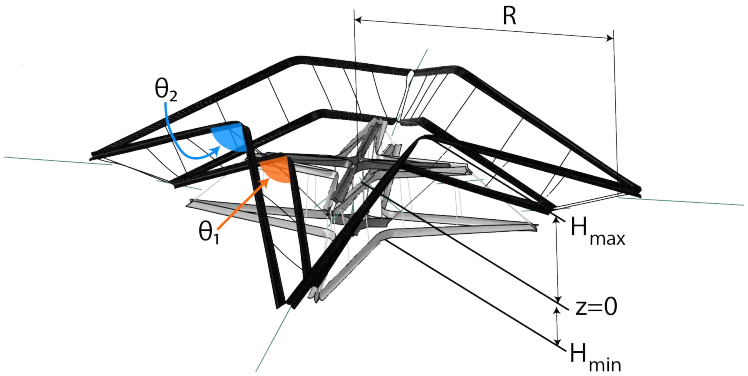

Figure 4.14: Definition of relevant metrics to describe the deployment of the space structure.

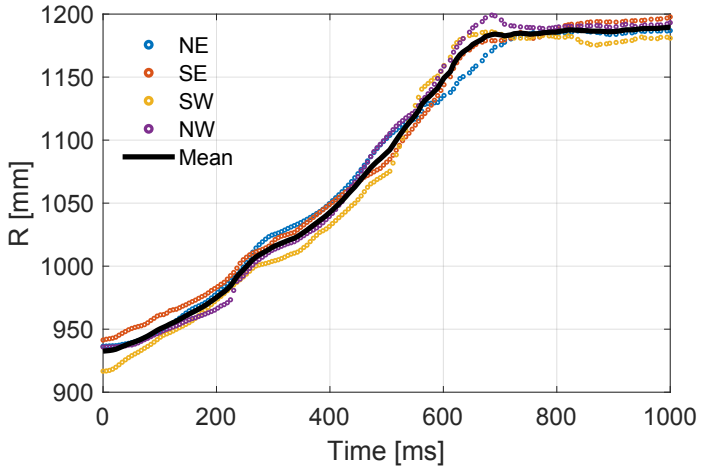

Figure 4.15: Distance of the corners from the central axis.

beginning of deployment, the only visible point was on longeron 2 of strip 3, i.e. the upper longeron on the outermost strip of the star-folded structure. The distance increased from the initial value of $R = 200$ mm to the deployed size of each strip. The deployment time of the longerons varied from $t = 584$ ms for the innermost longeron (longeron 1 - strip 1), to 702 ms for the outermost longeron (longeron 2 - strip 3).

Fig. 4.17b shows the mean height of the center of the longerons, as a function of time. The reference height $H = 0$ is the height of the ends of the diagonal cords, set by the position of the cord attachment to the central shaft of the deployment mechanism, and by the cord tensioning system. In the deployment mechanism, the structure was enclosed in the region -131 mm $\leq H \leq 91$ mm. At $t = 200$ ms, the outermost longeron (longeron 2 on strip 3) started moving upwards, reaching

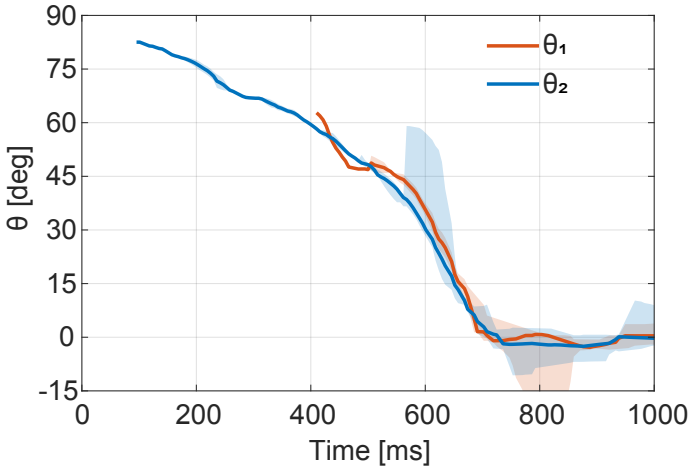

Figure 4.16: Mean fold angle on the outer strips.

a maximum height of 260 mm after 515 ms, before dropping to −50 mm at the end of deployment. The other longerons experienced a less pronounced vertical motion, with the ones on strips 1 and 3 moving upwards and the ones on strip 2 moving downwards, as a result of the kinematics of the star-folded structure. At the end of deployment, the longerons reached approximately the same final height. In micro-gravity, this height would be ideally zero; however, under the effect of gravity, the structure laid below the nominal height, so that the vertical component of the tension in the cords would support its weight.

Finally, Fig. 4.18 shows the deployment envelope of the center of the structure, reporting the maximum and minimum heights as a function of the distance from the central axis. This information has practical implications, as it defines the keep-out volume around the structure required for its deployment, thus affecting the size of the deployment mechanism and the arrangement of other subsystems in a spacecraft.

4.7 Numerical Model of Deployment

A finite element model of the deployment was developed using an explicit formulation in Simulia Abaqus 2020. 4-fold symmetry of the structure was assumed to reduce the computational cost of the simulations, by modeling a single quadrant as representative of the behavior of the whole structure. The resulting model is shown in Fig. 4.19: each strip consisted of two longerons, modeled with S4R reduced integration shell elements. Their material properties were assigned through direct specification of the ABD matrix for the flange and web laminates. The matrices were based on previous measurements by Leclerc and Pellegrino [57] on a similar

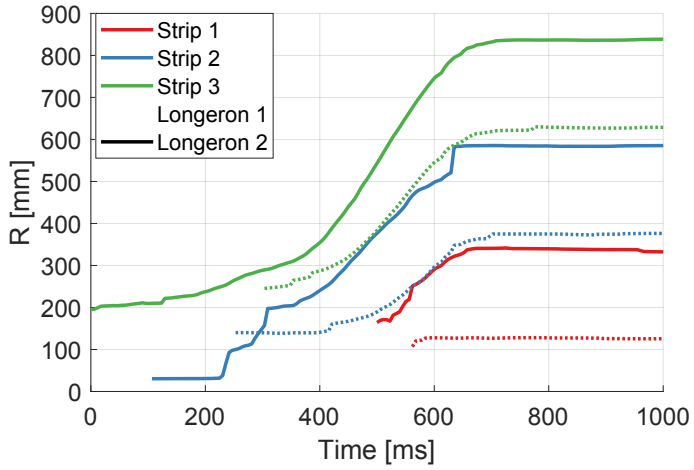

(a) Distance from the central axis vs. time

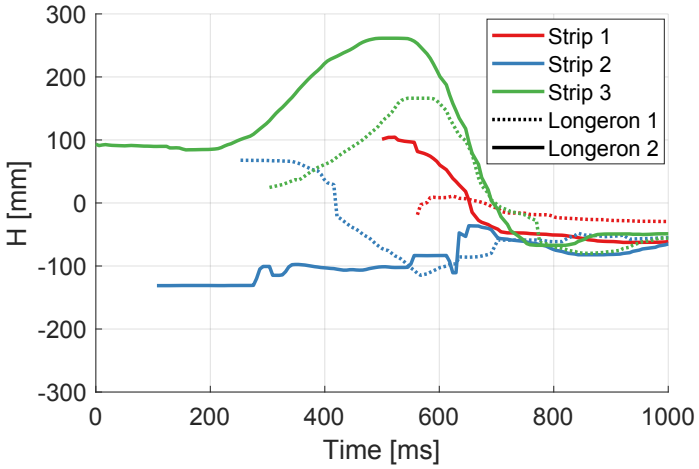

(b) Height vs. time

Figure 4.17: Mean envelope of the structure at the center of the strips.

laminate, and were validated through bending experiments of a rectangular strip presented in Chapter 2.

The battens were modeled using B31 linear beam elements, with a 3 mm $\times$ 0.6 mm rectangular cross-section. They were connected to the longerons using kinematic coupling constraints between a master node (the end node of the batten) and the nodes on the longeron web in a 14 mm $\times$ 14 mm region around the master node, as shown at the bottom right of Fig. 4.19. Although this modeling choice effectively assumes that the longeron-batten connectors are rigid, the simplification was deemed acceptable for this problem. At the ends of the strips, diagonal battens supported the strip-cord connectors, which were modeled as a multi-point constraint between

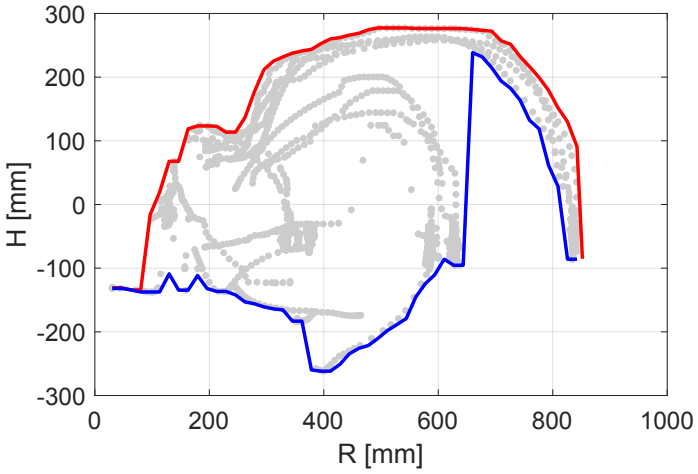

Figure 4.18: Deployment envelope of the structure, measured at the center of the strips.

a reference point, placed on the diagonal plane of the structure, and a 10-mm-long region of the batten, corresponding to the size of the actual strip-cord connectors. In this case, the hypothesis of rigid connector was accurate, as the actual ones were made out of solid 3D-printed plastics, and therefore were much stiffer than the battens.

4.7.1 Diagonal Cord Model

Consecutive strips in a quadrant were connected by diagonal cords at the location of their two strip-cord connectors, on each diagonal batten. In the physical prototype, only one of the two connectors was bonded to the cord, in order to suppress any rigid body motion between them, without over-constraining the system (which would result in the cords losing their tension). Since relative sliding is not allowed, the cord was modeled piece-wise, using 1D connector elements between the outer strip-cord connector of a strip and the inner strip-cord connector of the following strip. The resulting cord segments correspond to the red lines along the diagonals of the structure, in Fig. 4.19. The innermost connectors of the shortest strip were connected to a fixed point on the central shaft of the deployment mechanism. Likewise, the outermost connectors of the longest strip were connected to the cord tensioning system, whose model is described in detail later in this section. The mechanical response of the cords was described by a bi-linear elastic model, so that the cords would be very stiff in tension, approximating the stiffness of the steel cords used in physical prototypes, and very compliant in compression, approximating the slack behavior. The cords were "inactive" at the beginning of the simulation, and were

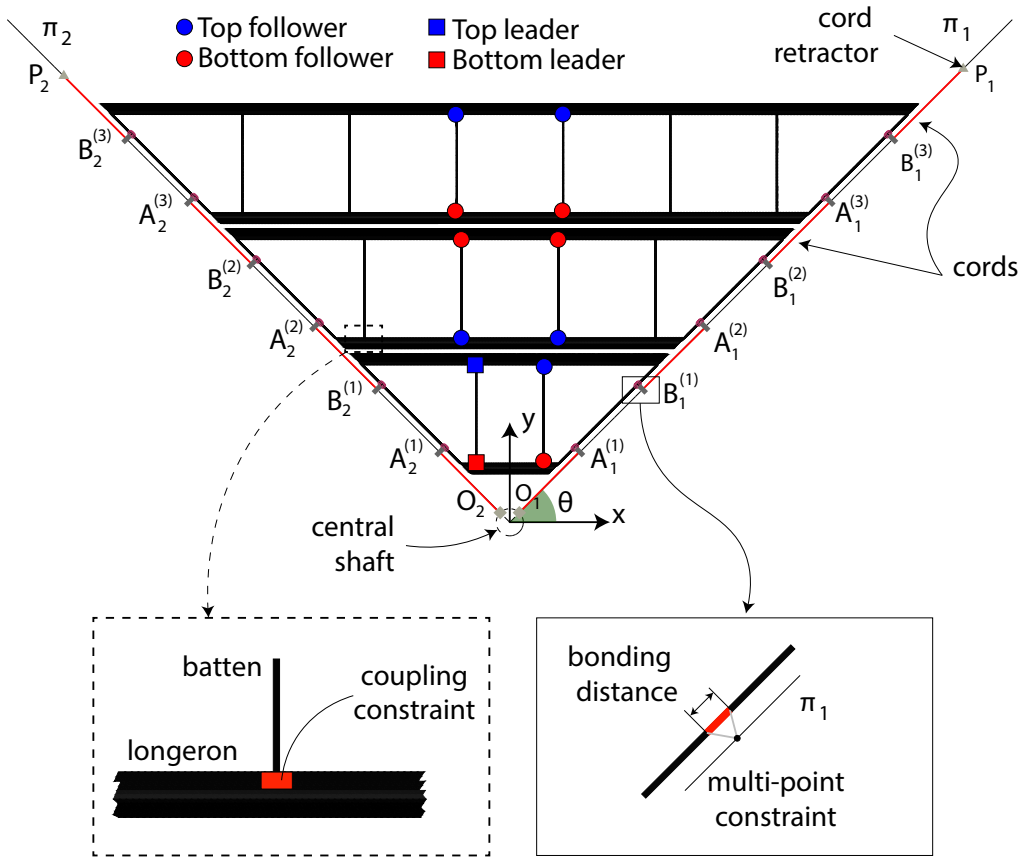

Figure 4.19: Finite element model of the space structure. 4-fold symmetry is assumed, allowing to model only one quadrant as representative of the entire structure.

activated only after the structure had reached its star-folded configuration. This choice was motivated by the fact that modeling an actual folding process compatible with the cord constraints would introduce unnecessary complications in the model; on the other hand, "disconnecting" the cords during folding would allow a simpler folding sequence, which can occasionally violate the cord length constraints along the folding path.

In practice, an internal variable f was defined on each cord (using *Predefined field variables* in Abaqus), and the constitutive model of the cords was expressed as a function of this variable. When $f = 0$, the cord was linear elastic, with a very low stiffness ($K_c = 10^{-3}$ N/mm); when $f = 1$, the bi-linear model previously mentioned was used, with stiffness $K_c = 10^{-3}$ N/mm in compression and $K_t = 10^3$ N/mm in tension. The internal variable f was set to 0 during the folding process, and

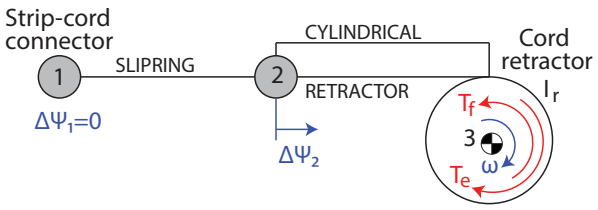

Figure 4.20: Finite element model of the cord tensioning system, using 1D connector elements. The model includes inertia, elasticity, and friction in the cord retractor assembly.

switched to 1 during the equilibrium step, when the structure was in the star-folded configuration.

4.7.2 Cord Tensioning System Model

The cord tensioning system was modeled using 1D connector elements, which capture its inertia, elasticity, and friction. A schematic of this model is shown in Fig. 4.20: it consists of 3 nodes, with node 1 corresponding to the outermost strip-cord connector of the structure, and nodes 2 and 3 sharing the same location, at the outer end of the diagonal cords. The model is based on the same approach used for the suspension system of the strip deployment in Chapter 2:

- a *slipring* connector ran between nodes 1 and 2, and allowed for a mass flow $\Delta\Phi_2$ to enter or exit the element at node 2, so that the cord could change its length as it spooled from the retractor, without undergoing elastic deformations; in addition to this, a bi-linear elastic model was defined, similar to the other cords, to prevent the slipring from transferring any compressive loads to the structure.

- a *retractor* element connected nodes 2 and 3, to convert the mass flow $\Delta\Psi_2$ into rotation ω of node 3, according to the relation: $\omega = \Delta\Psi_2/R_r$, where R_r is the radius of the cord retractor; the rotary inertia assigned to node 3 resulted in inertial effects to appear in the dynamics of the cord tensioning system.

- a *cylindrical* connector, in parallel with the retractor element, connected nodes 2 and 3. A linear elastic model of the form $T_e = T_e^0 + K_r\omega$ was assigned to this element, to account for the elasticity of the cord retractor. Additionally, a constant-amplitude friction torque of the form $T_f = \mu\ \mathrm{sign}(\omega)$ provided a first-order approximation of dissipative effects in the system.

4.7.3 Deployment Mechanism Model

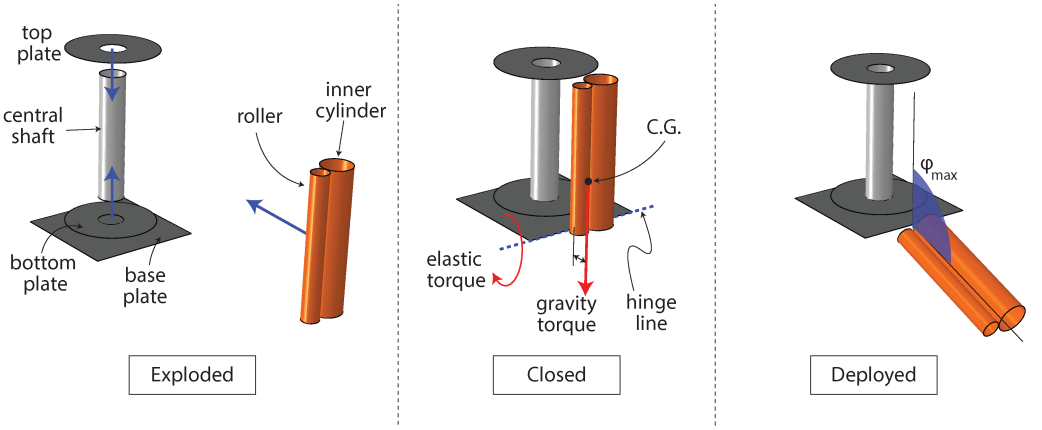

Figure 4.21: Finite element model of the deployment mechanism: exploded mechanism while folding the structure (left); closed mechanism when the structure is in the star shape (center); open configuration of the mechanism, after release of the rollers (right).

Figure 4.21 shows the finite element model of the deployment mechanism and illustrates its configurations during the deployment simulation. The model includes the central shaft, the top and bottom plates, a base plate, and the roller assembly (comprised of roller and inner cylinder). While folding the structure, the mechanism was in an exploded configuration to avoid any interference with the folding process. After the structure reached its star shape, the mechanism was closed by translating the top plate, bottom plate, and base plate along the vertical axis, and the roller assembly along the radial direction. A hinge-type connector element ran between the C.G. of the roller assembly and the location of the hinge axis. The roller was released by unlocking the rotational degree of freedom of the connector element. The rotation of the roller was driven by the elastic energy stored in pre-loaded torsional springs. In the physical prototype, two torsional springs were located on the hinge; additional kick-off compression springs were placed between the roller and the top plate of the mechanism to facilitate their separation. In the numerical model, the kick-off springs were converted into equivalent torsional springs by defining their elastic torque as $T_e = F_e d$ and their rotation as $\phi_e = \Delta x_e / d$, where d is the distance between the top of the roller and the hinge axis, and Δx_e is the compression of the springs. Since the kick-off springs only exerted a force on the roller assembly while they were in contact, their elastic force was set to zero for angles greater than their maximum contact angle. Three hinge-type connector elements were used in parallel, each adding the elastic contribution from a different set of springs. The values of the elastic constants for each set of springs are reported in the table below.

During ground experiments, the rotation of the rollers was also helped by gravity. While the effects of gravity could be automatically included by assigning the mass of the roller m_r to its center of gravity and defining a gravity field in the whole model, it was found that this resulted in excessive kinetic energy when closing the mechanism, as the mass of the roller amounted to about 10 times the mass of the entire quadrant. To address this challenge, gravity was included as a concentrated vertical force $F_r = m_r g$ applied directly to the C.G. of the roller, to which a very small mass (1 g) was assigned. A non-zero mass was essential to avoid mass mismatch between the nodes of the roller and longeron surfaces during contact; this mismatch would cause penetration of the surfaces, which would prevent separation afterwards. To capture the correct dynamics of the system, the total inertia of the roller about its hinge axis was assigned to the hinge reference point.

Friction in the roller mechanism was modeled as a constant-amplitude friction torque assigned to the main hinge element, using the same formulation described for the cord tensioning system. The amplitude of the friction torque was obtained through calibration from experiments, which are described later in this chapter. Finally, the rotation of the roller was locked once it reached a maximum value ϕ_{max}, as shown in Fig. 4.21. This accounted for the actual range of the rollers in the physical mechanism, which was limited by their height from the ground.

4.7.4 Symmetry Conditions

N-fold rotational symmetry of an object requires that the object remains the same after rotations by multiple of $2\pi/n$ about its symmetry axis. In simulation, this condition was imposed at the boundary points between adjacent quadrants, i.e. on the strip-cord connectors. This guaranteed that their displacements were compatible with a 4-fold symmetric structure so that, if the solution for a single quadrant was rotated by $k\pi/2$, with $k = 1, 2, 3$, the strips belonging to the same square loop would be hinged together at the location of the strip-cord connectors.

Defining by u, v, and w the displacement components along x, y, and z, with the pedices referring to the points at the two ends of the strips, symmetry of a quadrant can be defined as follows:

$$\begin{bmatrix} u_1 \\ v_1 \\ w_1 \end{bmatrix} = \begin{bmatrix} 0 & -1 & 0 \\ 1 & 0 & 0 \\ 0 & 0 & 1 \end{bmatrix} \begin{bmatrix} u_0 \\ v_0 \\ w_0 \end{bmatrix} \tag{4.9}$$

These conditions were imposed to each pair of strip cord-connectors at the two ends

of each strip, using 3 scalar linear equation constraints for each pair of points.

While Eq. 4.9 fully defines the symmetry conditions from a mathematical standpoint, it is not sufficient to model the physical problem. In particular, it does not prevent penetration between strips of adjacent quadrants. This becomes a problem when the structure is folded in its star shape, where contact occurs between adjacent strips. To address this challenge, two rigid diagonal planes were added (π_1 and π_2 in Fig. 4.19), in order to contain the strips in the region between the planes, through contacts. An additional linear equation constraint

$$u_0 = v_0 \tag{4.10}$$

was added to each strip-cord connector along one of the diagonals, in order to constrain the ends of the strip to lie on such planes. One of the consequences of the use of diagonal planes is that the 4 arms of the star shape are forced to be straight: although this is not a necessary condition (they could also deform in a curved shape), experiments revealed that the arms are straightened by the tension applied at the ends of the diagonal cords, thus justifying the approximation.

4.7.5 Simulation Technique

The simulation consisted of two main parts, folding and deployment, organized in several steps:

1. Z-folding the structure;
2. closing the mechanism;
3. applying external loads;
4. equilibrium;
5. deployment.

In the first step of the simulation (Fig. 4.22a), the quadrant was Z-folded by applying a vertical relative displacement $\Delta z = a$ to the two ends of the battens at the center of each strip, which acted as control points for this process. Fig. 4.19 shows the locations of the control points, which are classified in "top" (blue) and "bottom" (red), depending on whether they are located on a mountain or valley fold. For each of these groups, a leader node (square marker) was defined, whose out-of-plane displacement was imposed to its follower points (circular markers). This facilitated

the folding process, as it allowed folding the structure by controlling the relative displacement between a single set of nodes. These constraints were defined as linear equation constraints, similar to the ones used to impose symmetry. However, in this case, the constraints had to be removed later in the simulation, in order to allow each strip to move freely during deployment. To this extent, a dummy node was created for each equation constraint, which was written as:

$$w_f - w_l = w_d \tag{4.11}$$

where w_f, w_l, and w_d represent the out-of-plane displacement of a follower node, a leader node, and a dummy node, respectively. When $w_d = 0$, the equation reduces to imposing the same vertical displacement to the leader and follower node; if w_d is not set, the left-hand side of the equation can take any value, effectively deactivating the constraint. A small mass $m_d = 10^{-3}$ g was assigned to each dummy node to avoid singularities in the mass matrix, without introducing any appreciable effect on the dynamics of the model.

In the second step of the simulation (Fig. 4.22b), the out-of-plane displacements of the control points were locked, and the structure was pushed in its star shape by applying in-plane displacements (along the y-axis in Fig. 4.21) to the ends of the battens on the outermost strip of the quadrants. Meanwhile, the deployment mechanism was closed around the structure, by translating the top/bottom plates along the z-axis and the roller assembly along the y-axis.

In the following step (Fig. 4.22c), the external loads were applied to the structure: in particular, gravity was introduced, the cords between strips were activated (by changing the value of their internal variable), and the elastic torque was applied to the cord retractor system (similarly to the cords). The equation constraints between the control points were deactivated by freeing the displacements of the dummy nodes, as well as the vertical displacements of the leader nodes.

Viscous pressure was applied to the entire model to dissipate any residual kinetic energy in the system. It was observed that, in some instances, the longeron flanges could fold on themselves due to contacts between strips, especially at the ends of the longest longeron of each strip. To avoid such problems, the flanges were briefly flattened and slowly released at these critical locations, achieving a more predictable configuration of the longerons. In the equilibrium step, the viscous pressure was gradually reduced to zero, and the linear bulk viscosity was decreased from 10^{-4} to 10^{-6}, in order to minimize viscous effects on the deploying structure. Based on the

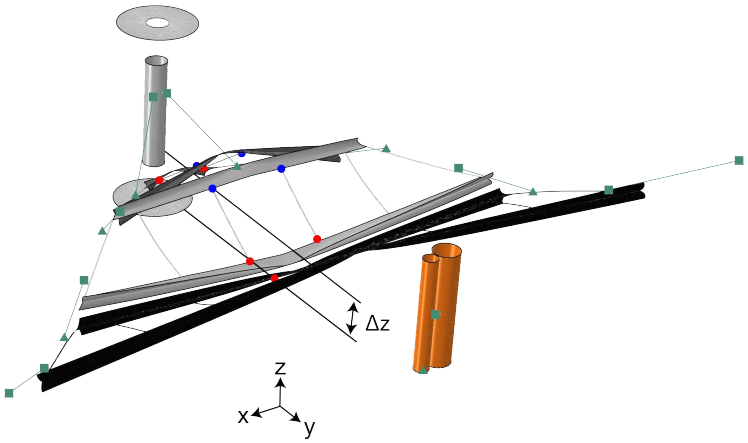

(a) Z-folding

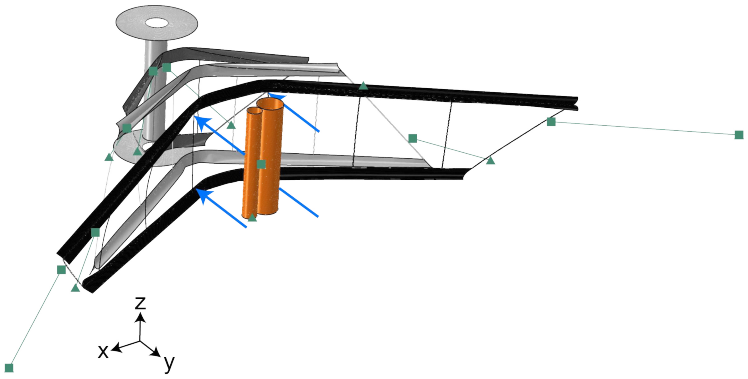

(b) Closing the mechanism

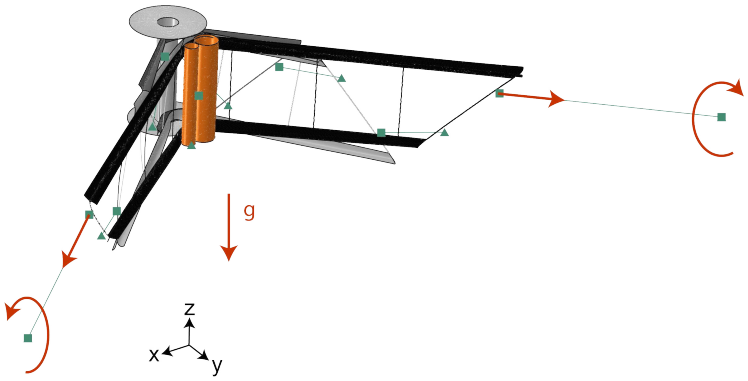

(c) Applying loads

Figure 4.22: Folding simulation of the space structure (diagonal planes not shown).

findings from the strip deployment study in Chapter 2, air effects are expected to be negligible for a structure without membranes, and therefore were not included in the simulation. Finally, the deployment simulation was initiated by simply releasing the rotation of the roller about its hinge axis.

It can be noticed that the deployment of the structure does not occur until the very

final step of the simulation, while all the previous steps were only intended to get the structure from its initial, undeformed configuration to the folded configuration, in the star shape. This is because deploying the structure only requires removal of any applied constraints and letting it follow its minimum energy path, whereas folding the structure requires actively controlling its many degrees of freedom to avoid undesired deformations and instabilities, achieving the correct folded configuration.

4.8 Numerical Results

4.8.1 Model Validation

The numerical model was validated by comparison with the experimental data presented earlier in this chapter. Three metrics were chosen for the comparison: the distance of the corners of the strips from the central axis, the evolution of the angle of the elastic folds on the outermost strips, and the maximum / minimum height of the center of the strips over time.

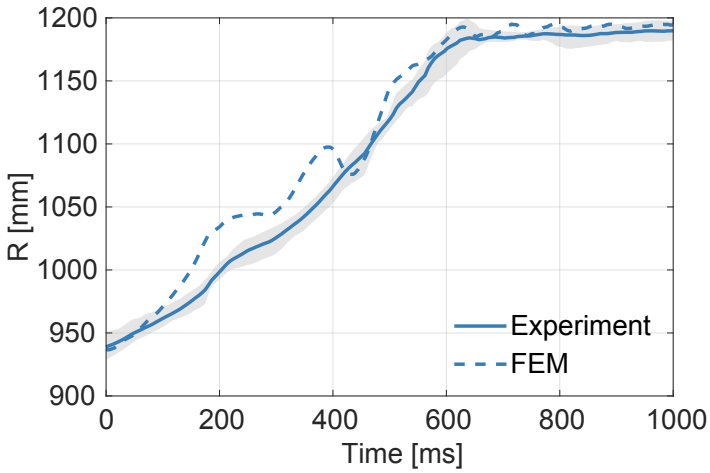

Figure 4.23: Position of the corners of the structure along the diagonal.

The first metric is plotted in Fig. 4.23: in the finite element model, synmmetry conditions impose the same distance from the central axis to each corner of the structure, hence a single curve is shown. For the experiments, the distance of the 4 corners was averaged (blue line), and the envelope of the experimental data is indicated by the shaded grey region. The numerical results capture very well the deployment time measured in experiments, with the corners of the structure reaching their maximum distance after 630 ms (about 5% faster than the experiment). However, some differences can be observed at the very beginning of deployment, in which the numerical model deploys faster than the experiment, with a maximum

error of about 50 mm, at any given time. The discrepancy is possibly due to the numerical model not accounting for the short delay (of the order of 50 ms) between release of the roller arms in the deployment mechanism, observed in experiment. Also, the simplified geometry of the roller arms in simulation removed some of the geometric features that protruded in the real mechanism (such as the Micro Latch of the release system), thus facilitating the extraction of the strips from the mechanism, compared to the experimental case.

At 400 ms, an oscillation of the distance R slows down the deployment simulation, resulting in a better matching with the experiment. This oscillation was due to contact between the edge of the deployed roller and the flange of a longeron on the middle strip. At the end of the deployment, the numerical model predicted small oscillations in the distance of the corners, due to elastic vibrations of the structure, showing a less dissipative behavior than observed in experiment.

Fig. 4.24 compares the angles of the elastic folds at the center of the outermost strips. Except for a more oscillating behavior, the finite element model follows quite closely the angles reconstructed from the experiment, with an RMS error of about 15% on the angle of longeron 1, and 12% on the angle of longeron 2.

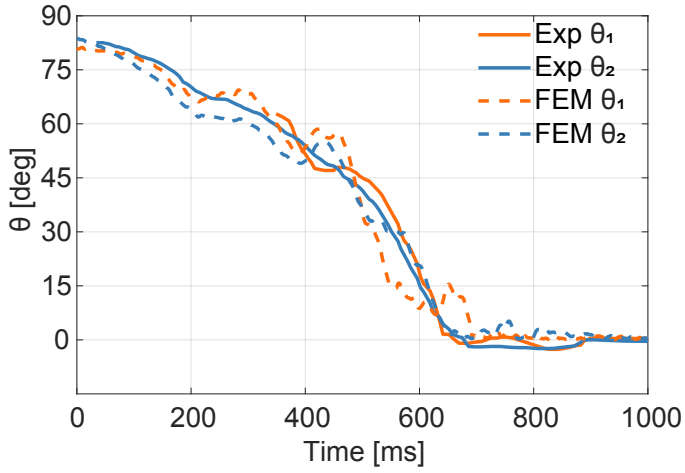

Figure 4.24: Angle of the elastic folds on the central strip.

Finally, Fig 4.25 compares the maximum and minimum height of the structure during deployment. The results in Sec. 4.6 showed that the extreme values occur at the center of the strips, with the maximum height being on the outermost strip, while the minimum height corresponds to the middle strip. Therefore, only these two strips were considered for the comparison. The plot confirms that, at the beginning of

deployment, the outer strip quickly moves upwards in simulation, sliding in the gap between the top plate of the mechanism and the roller arm, shortly after its release. In experiment, this vertical motion did not occur until about 200 ms after the roller release. Also, the deployment in simulation is more dynamic, with a maximum height of about 390 mm, vs 260 mm measured in experiment. However, after 400 ms, the simulation matches more closely the experiment. Regarding the height of the middle strip, its minimum value from simulation is 260 mm below the reference height, whereas, in experiments, the height remains mostly constant, varying from -130 mm and -60 mm during deployment. At the end of deployment, the structure overshoots in simulation, peaking at an height of about 45 mm above the reference height, before dropping to approximately the same final value as in experiment.

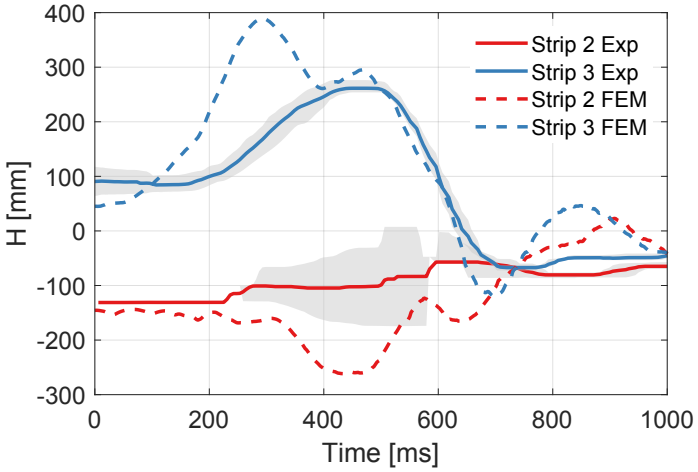

Figure 4.25: Evolution of maximum and minimum height of the structure, measured at the center of the strips.

4.8.2 Numerical Determination of the Deployment Envelope

Experimental determination of the deployment envelope of the structure can be challenging, as many points are not visible to the cameras, especially in the first phase of deployment. Figure 4.17 showed that this is often the case for the inner strips, as well as for the longerons at the bottom of the star-folded structure. A finite element model represents a powerful alternative, as it provides high spatial resolution data on the entire structure, throughout deployment. Fig. 4.26 shows the deployment envelope from the simulation presented in the previous subsection. The maps show the lowest and highest points on the structure, respectively.

Fig. 4.26a indicates that the highest point on the structure is located at the center of the strips, in accordance with the observations from experiments. Regarding

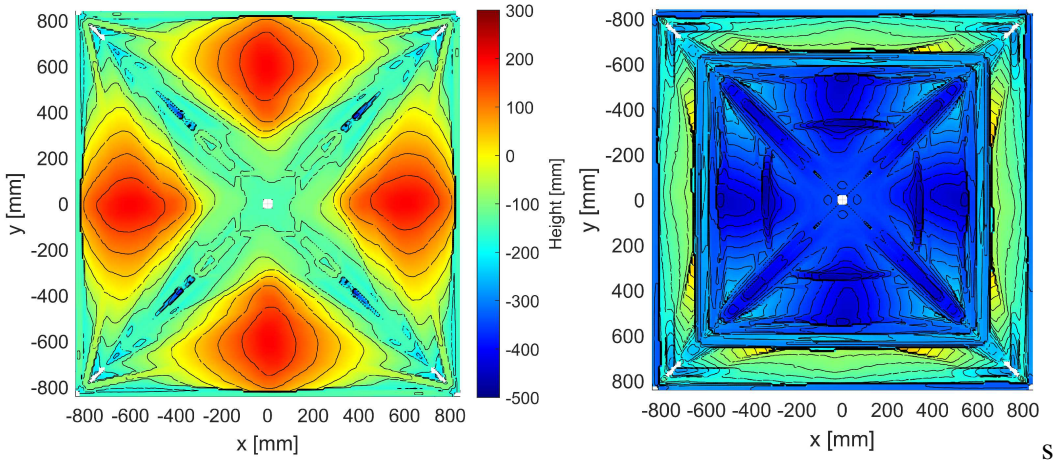

(a) Highest points on the structure

(b) Lowest points on the structure

Figure 4.26: Envelope of the structure during deployment.

its lowest point, Fig. 4.26b identifies two potential locations: the center of the strip and the diagonals of the structure, which reached $H^c_{min} = -471$ mm and $H^d_{min} = -440$ mm, respectively.

4.8.3 Behavior of the Elastic Folds

The finite element model constitutes an ideal tool to investigate the behavior of the elastic folds in the structure during deployment, providing access to deformation and energy data with high spatial resolution. In particular, the strain energy field in the longerons was found to be the most useful tool for this purpose. Fig. 4.27 provides an overview of the analysis scheme adopted.

1. First, the strain energy of each element was exported from Abaqus at each increment of the solution, along with the connectivity matrix, and the undeformed nodal coordinates, necessary to locate the element in the structure. This provides snapshots of the strain energy distribution in the structure, at each time increment (see Fig. 4.27, top right).

2. Then, the strain energy per unit length of each longeron was computed by summation of the energy in the elements along the cross-section, and accounting for the element size. This allows us to create maps of strain energy per unit length for the each longeron (Fig. 4.27, middle right), reporting the distribution of strain energy along the axial direction (y-axis) as a function of time (x-axis).

3. Finally, the strain energy history of the longeron can be computed by integrating the strain energy map along the length of the longeron (Fig. 4.27, bottom right).

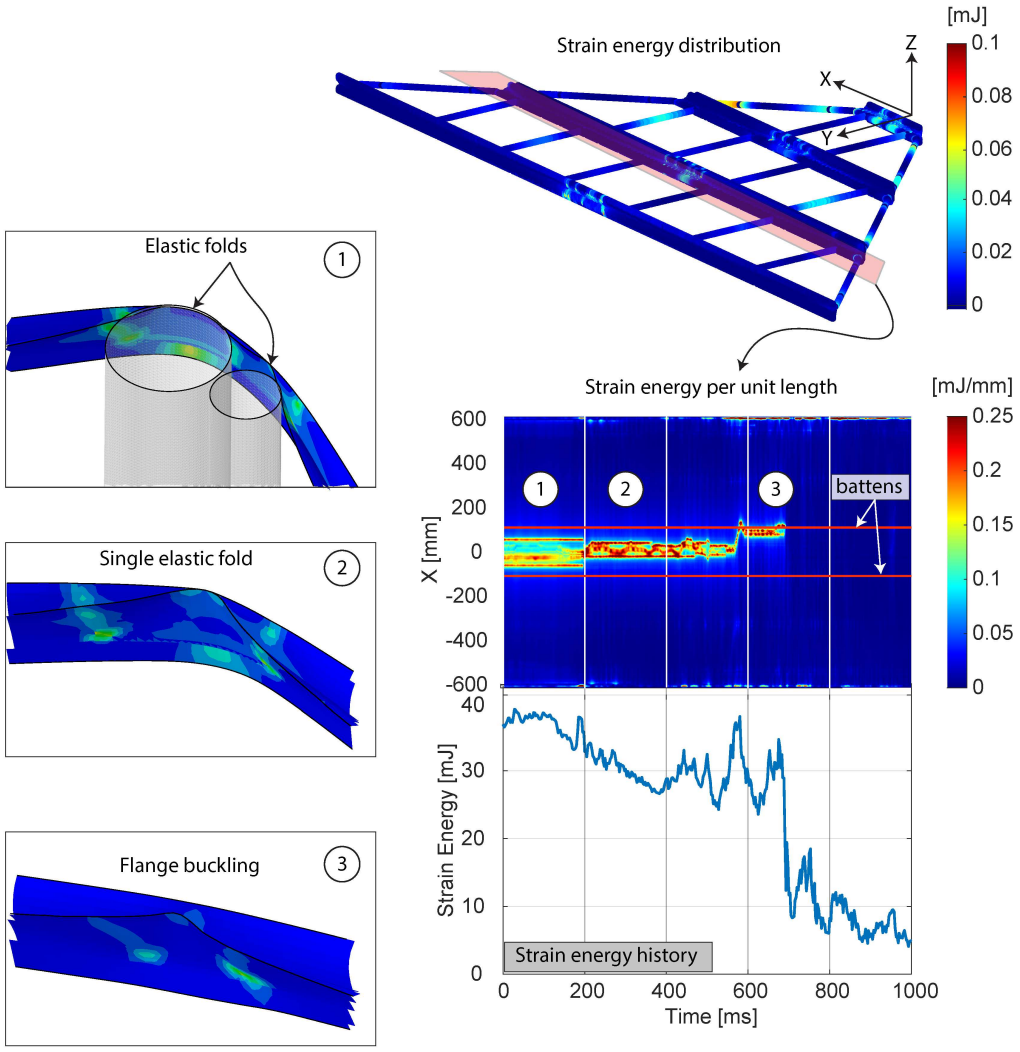

Figure 4.27: Behavior of the elastic folds during deployment of the structure. Top right: distribution of strain energy of the finite elements in the structure, at the beginning of deployment. Middle right: map of strain energy per unit length of a longeron (the example shows longeron 1 of strip 3). Bottom right: strain energy history of the longeron. Left: snapshots from the simulation, showing different configurations of the elastic folds during deployment: in (1), there are 2 separate folds; in (2), the folds have merged into one; in (3), inner flange buckling.

The map of strain energy per unit length allows us to clearly identify the locations of the elastic folds in the longeron, as they correspond to regions of high curvature and, therefore, high strain energy. The map in the example of Fig. 4.27 shows

a typical behavior of the elastic folds. At the beginning of deployment ($t = 0$), there are two separate elastic folds, induced by the roller and the inner cylinder (1). The strain energy in the two folds is slightly asymmetric, due to cylinders having different diameter and, therefore, imposing different curvatures. After 200 ms, the two folds merge into one (2): the strain energy map shows two sharp lines at the boundaries of elastic fold, corresponding to its transition regions, characterized by bending and torsional stresses. At $t = 550$ ms, the elastic fold turns into flange buckling on the compression side of the fold (3). In this configuration, the other flange and the web are essentially straight and with negligible strain energy. At this point, the strain energy map shows that the buckle propagates, until it reaches the closest batten (indicated by the line in the plot) and remains stationary until it disappears, at $t = 690$ ms. This finding suggests that the battens create an energy barrier for the propagation of instabilities, by locally increasing the stiffness of the longeron. This supports similar observations on the deployment on the deployment dynamics of a single strip, discussed in Chapter 2, for which it had been found that, whenever an elastic fold propagated, it would never cross a batten.

4.9 Discussion and Conclusion

In this chapter, we have presented an experimental and numerical framework to characterize the deployment dynamics of a novel class of thin-shell space structures. While the packaging and deployment scheme has been previously demonstrated on small-scale, idealized structures, and several space structure prototypes have been developed, based on this architecture, this work is the first attempt at capturing and predicting the complex dynamics of a structure consisting of a large number of thin-shell components, folded together and deploying in a 3-dimensional motion. The problem was studied with a dual approach: on one hand, deployment experiments on a 2-m-scale space structure prototype were performed to observe the behavior of a real system; on the other hand, a finite element model was implemented, offering high-resolution data and a prediction and design tool for these structures.

On the experimental side, we have shown that motion capture systems represent a powerful tool to easily track hundreds of points on the structure. Although spherical markers generally yield better performances and offer a wider range of motion, it was found that flat, flexible markers were sufficient to follow most of the points on the structure, without interfering with its packaging process (e.g. coiling). Unlike other optical measurements, such as Digital Image Correlation, motion capture systems do not require special preparation of the surfaces (e.g. painting or speckling), and

therefore offer a potential solution for large-scale applications and characterization of flight hardware. In order to characterize the dynamics of the structure, we have proposed an algorithm to reconstruct the shape of the longerons, measure the angle of their elastic folds, and follow the trajectory of critical points. This method offers an unprecedented level of detail on quantitative aspects of the deployment, allowing assessment of its symmetry, measurement of the deployment envelope of the structure, and verification of the repeatability of the experiments. Several features aiming at increasing the robustness of the algorithm have been implemented: data from different points in the cloud can be combined to increase the tracking range of each point, and redundant points are used to measure the angle of the elastic folds. However, the main limitation is that the algorithm relies on manual assignment of each point in the cloud to the corresponding physical point on the structure, for many time steps. Especially when the structure is still folded, the identification of the points might be challenging and can lead to false matching, which increases the noise in the measurements and deteriorates the quality of the data.

On the numerical side, we have developed a high-fidelity finite element model of the deployment dynamics of the space structure. The model uses a combination of established modeling techniques, such as equation constraints with dummy nodes, field-dependent material properties, and 1D connector elements, to correctly fold the structure into the star-shape in the least number of steps, and accurately model its interaction with the deployment mechanism.

Overall, the results show good agreement with the experiment, capturing the deployment time with less than 5% error. The evolution of the elastic folds on the outer strips is also captured with good accuracy. However, the model overpredicts the velocity of the structure in the early stage of deployment, showing higher inertial effects than observed in experiment. The results presented in this chapter were based on the assumption of 4-fold symmetry of the structure, in addition to having the ends of the strips lie on the diagonal planes. While the experiment has shown that the deployment is mostly symmetric, deviation from symmetry occurred both due to variability in the initial conditions and delays in the release of the rollers in the mechanism. As symmetry-breaking conditions can, sometimes, offer softer deformation modes of a structure, it would be interesting to evaluate the effect of small deviations from symmetry on the deployment dynamics of the structure. The comparison between experiments and simulations also highlighted that the interaction between the space structure and the deployment mechanism can greatly affect the

dynamics of the system. In particular, contacts and geometric interference between parts can change both the kinematics and dynamics of the structure. While the model currently uses an idealized geometry of the deployment mechanism, it might be necessary to use higher fidelity representations to better capture the geometric interaction between parts. Although more work is needed to refine and improve the model, the numerical results in this chapter offered invaluable insights into the deployment dynamics of the structure. On one hand, it complemented the experimental approach, especially for the regions of the structure that could not be tracked by the motion capture system. On the other hand, it provided detailed information about the behavior of the structure, allowing us to study the evolution of the elastic folds on the longerons.

The main limitation of this approach is its computational cost: as the current model requires about 4 days to complete a simulation on a server, modeling larger structures or including thin membranes on the strips would quickly result in prohibitive computational costs. In these cases, reduced-order models or adaptive meshing techniques might offer substantial advantages.

Chapter 5

CONCLUSIONS

5.1 Summary and Contributions

This thesis has presented the first comprehensive study of the packaging and deployment of large space structures consisting of multiple thin-shell components. The overall objective of this research was to demonstrate the feasibility of structural architectures that can be elastically packaged in small volumes, and yet maintain a planar shape once deployed, thanks to their bending stiffness. Existing spacecraft architectures are based either on rigid structures that provide high bending stiffness, but require complex and heavy mechanical articulations for packaging, or on thin membranes, which can be easily packaged in small volumes, but require external preloading to maintain their deployed shape. Thin-shell deployable structures combine the best of both worlds, offering high bending stiffness and elastic packageability, in addition to the potential for self-deployment, using their stored elastic energy.

While current applications employ thin shells as standalone deployable booms, combining multiple thin-shell components in a space frame can extend this technology to large-area applications, such as solar arrays and antennas. Not only can this lead to a new generation of deployable structures with superior stiffness-to-mass ratio and packaging efficiency, but it can also enable entirely new technologies, such as space solar power, so far limited by excessive cost, mass, and mechanical complexity. Despite their potential benefits, the feasibility of these structures depends on the ability to achieve reliable and predictable deployment, which requires understanding of their mechanical response. Previous studies on the dynamics of folded thin shells have highlighted the complexity of their dynamic behavior, dominated by the onset and evolution of elastic folds. These challenges are exacerbated when considering a space structure with many thin-shell components interacting with each other. Ground experiments provide vital information, but are affected by undesired environmental effects, such as air and gravity. On the other hand, numerical models can predict the behavior of the structure in space, but they often struggle with complex contact conditions and instabilities.

In this thesis, the following steps have been undertaken to address some of those

key challenges:

- **Study of the Deployment Dynamics of a Rectangular Strip**

  A strip architecture consisting of 2 thin-shell longerons, connected by transverse battens, was presented in Chapter 2. The strip was symmetrically folded with two elastic folds, and deployed under strain energy. A suspension system was designed to support the structure during deployment. Deployment experiments were performed both in air and in vacuum, to understand the interaction with air on the deployment dynamics of the structure; the results showed that air significantly affected the behavior of the structure if the surface of the strip was covered by a thin membrane, intended to support functional elements in a space application. In this case, the deployment in air was up to 70% slower than in vacuum. However, air effects were negligible in the absence of the membrane. We have also shown that, with this suspension system, the elastic folds do not propagate in typical conditions, thus behaving in a predictable way, as elastic hinges. A finite element model of deployment was implemented in Abaqus, and a simple method to model air effects was proposed, demonstrating excellent agreement with the experiments under various conditions and different types of structure. The deployment of an unconstrained strip in micro-gravity was predicted using simulations, and the result was used as a baseline to compare different suspension system architectures for ground testing. It was shown that the current implementation added significant inertia to the system, and that alternative concepts might yield results closer to the baseline.

  The main contributions from this work are:

  – an experimental framework to measure the dynamics of a thin-shell structure, based on high-speed imaging and Digital Image Correlation;

  – a robust algorithm to identify and track elastic folds on a structure from full-field displacement data;

  – a computationally efficient approach to include air effects in simulations, without requiring calibration with experiments. The model is based on geometric arguments to estimate the added air mass to the structure, and to identify a drag coefficient from values in literature;

  - a numerical framework to accurately predict the deployment dynamics of strips and capture the effects of air, gravity, suspension system, and a functional membrane covering the structure.

- **Analysis and Implementation of the Packaging and Deployment of a Thin-Shell Space Structure**

  Chapter 3 focused on the packaging and deployment of a space structure, composed of multiple thin-shell trapezoidal strips, arranged in a square architecture and connected by diagonal cords. This architecture and its packaging concept had been previously proposed for space solar power applications. In this thesis, we demonstrated, for the first time, the implementation of this concept on a 2-m-scale structural prototype, and we discussed its extension to larger scales. First, we proposed a systematic approach to folding the structure in a predictable way, by imposing elastic folds at opportune locations. A kinematic model was implemented to identify admissible kinematic paths for the structure, and to design a folding sequence that accounts for the kinematic constraints between interconnected strips.

  Then, we presented a novel deployment mechanism concept (patent pending) to coil and uncoil the structure in a cylindrical configuration. The mechanism relies on co-coiled membranes under tension to prevent packaging instabilities in the structure, by converting tension in the membranes into pressure on the structure. While the concept of pressure stabilization has already been used in the past for deployable booms, novel features have been proposed in this thesis: the use of force control in place of displacement control to tolerate deviations from symmetry during coiling; and the decoupling of the coiling actuation from the membrane tensioning system, which allowed for more controlled loads on the structure. These features contributed to increasing the robustness of the deployment mechanism, which was successfully demonstrated on 2-m-scale structural prototypes.

  Finally, a staged deployment scheme was proposed to deploy the folded structure. The concept consists of a sequence of dynamic deployment steps between intermediate, known configurations, defined by releasable constraints that impose elastic folds at opportune locations. This approach reduces the uncertainty associated with strain-energy deployment of the structure, as well as inertial effects during the process, making it well-suited for large-scale applications.

The outcome of this research has enabled DOLCE (Deployment On-orbit of an uLtralight Composite Experiment), the first flight demonstration of the space solar power architecture studied in this thesis, set to launch in 2022. The packaging scheme for the flight structure is based on the folding sequence presented in Chapter 3, and the deployment mechanism is an implementation of the concept proposed in the same chapter. The experimental framework presented in Chapter 4 is also being used for the characterization of the deployment dynamics of the space structure, throughout its launch qualification process. Furthermore, a variant of the deployment mechanism concept has been implemented to coil/uncoil individual thin-shell strips for the JPL/Caltech LADeR (Large-Area Deployable Reflectarray) project [6].

- **Investigation of the Deployment Dynamics of a Thin-Shell Space Structure**

  The work on the deployment dynamics of a single strip, presented in Chapter 2, was extended to the space structure introduced in Chapter 3, to quantitatively characterize its behavior, both experimentally and numerically. The unique challenges associated with measuring the deformation of a large number of thin-shell components that deploy in a complex 3-dimensional motion were addressed. A motion capture system tracked the location of discrete points on the structure, and an algorithm was implemented to measure the deployment time, reconstruct the angle of the elastic folds, and compute the deployment envelope of the structure.

  A high-fidelity finite element model of deployment, based on the assumption of 4-fold symmetry, was implemented in Abaqus. The simulations captured the measured deployment time within 5% error, and showed good agreement with the experiments on other metrics too. The numerical data provided invaluable insights into the deployment process and the evolution of the elastic folds on the longerons.

  The main contributions from this work are:

  – the first quantitative characterization of the deployment dynamics of a thin-shell space frame;

  – an experimental framework, based on motion capture technologies, to track hundreds of points on a flexible structure, and extract key information about the deployment from the point clouds;

– a technique to simulate, in a finite element environment, the complex folding process of a space structure, and capture its interaction with the deployment mechanism during unfolding.

5.2 Future Work

This thesis demonstrated that thin-shell space structures can be packaged and deployed in a controlled and predictable way, paving the way for the development of novel shell-based structural architectures and their application in space. However, we believe that this initial research can be expanded and improved in the following areas:

- **Investigation of the structural vibrations after deployment**. Deployment experiments on the structural prototypes studied in this thesis have shown the vibrations after deployment to be quickly dissipated without producing any major effects. Therefore, this research has only focused on the deployment process until latching of the elastic folds. However, we expect vibrations to become more important as the structure becomes less stiff (due to increased size of the longerons), heavier (in the presence of functional membranes on the strips), and less damped (in the absence of air). Such conditions would make it likely for the longerons to buckle again after the first latching, as it has been shown to happen for different thin-shell structures, resulting in a complex sequence of latching and buckling until enough energy has been dissipated. Also, the vibrations after complete latching would take much longer to dissipate than on 2-m-scale prototypes and might require active control from the spacecraft control system. Therefore, a detailed investigation of the post-deployment structural behavior is needed to quantify the amplitude of the elastic vibrations and ensure that they are controllable.

- **Assessment of the loads on the membranes**. In this thesis, the membranes have mostly been investigated in terms of their effect on the deployment dynamics of the strips, and have not been included at all in the deployment study of the space solar power structural prototype. However, as the membranes are meant to support the functional tiles in a spacecraft (including photovoltaics and antennas), it is crucial to quantify the loads that they experience during deployment to guarantee their survivability. While the computational framework developed in this research offers an ideal starting point for such analyses, additional details might be required to accurately capture the stresses

on the membrane, which are influenced by the stiffness of the interface with the longerons and battens, as well as by the prestress that can result from the manufacturing process.

- **Investigation of symmetry-breaking phenomena during deployment.** The deployment experiments on the space structure showed that the deployment was mostly symmetric, despite some variability. However, propagation of the elastic folds is often associated with symmetry-breaking phenomena, as observed for the strip deployment study. Also, non-symmetric kinematic paths can result in lower energy configurations of a structure, and therefore be energetically-favorable. A systematic study of the effects of such deviations from symmetry can shed light on the behavior of a structure in real conditions, building confidence in the reliability of thin-shell structures.

- **Extension to different architectures**. While this research focused on a specific structural architecture, the numerical models we proposed can assist the development of novel thin-shell structures and their deployment mechanism by predicting their interaction. They can also be used to predict the deployment of a structure in space, and compare different suspension system designs to find the design that best approximates that behavior during ground testing.

- **Computational cost of the simulations.** The symmetric model of a 2-m-scale space structure, without membranes on it, required about 4 days to run on a server with 8 CPUs. High-fidelity models of larger structures, without symmetry assumptions, and/or with membranes on the strips do not seem a viable solution, due to their prohibitive computational cost. On the other hand, lower fidelity models can provide a valid alternative. Multi-body dynamics has been used to model the behavior of structures based on tape springs. Model reduction techniques offer a promising solution, as they can greatly reduce the numerical costs while still achieving good solution accuracy for certain problems. Adaptive meshing can also be beneficial, as it reduces the number of degrees of freedom in the model.

BIBLIOGRAPHY

[1] Aaron Adler and Martin Mikulas (2001). "Application of a wrinkled membrane finite element approach to advanced membrane structures". In: *AIAA Space 2001 Conference and Exposition*. 2001-4646.

[2] David Alexander, Philip Henderson, and Greg Turner (2014). "Advancements in large mesh reflector technology for multi-beam antenna applications". In: *The 8th European Conference on Antennas and Propagation (EuCAP 2014)*. IEEE, pp. 410–412.

[3] Manan Arya (2016). "Packaging and deployment of large planar spacecraft structures". PhD thesis. California Institute of Technology.

[4] Manan Arya, Nicolas Lee, and Sergio Pellegrino (2016). "Ultralight structures for space solar power satellites". In: *3rd AIAA Spacecraft Structures Conference*. 2016-1950.

[5] Manan Arya, Nicolas Lee, and Sergio Pellegrino (2017). "Crease-free biaxial packaging of thick membranes with slipping folds". In: *International Journal of Solids and Structures* 108, pp. 24–39.

[6] Manan Arya, Jonathan F Sauder, Richard Hodges, and Sergio Pellegrino (2019). "Large-area deployable reflectarray antenna for CubeSats". In: *AIAA Scitech 2019 Forum*. 2019-2257.

[7] M Aufaure (1993). "A finite element of cable passing through a pulley". In: *Computers & Structures* 46.5, pp. 807–812.

[8] Chris Biddy and Tomas Svitek (2012). "LightSail-1 solar sail design and qualification". In: *Proceedings of the 41st Aerospace Mechanisms Symposium*. Jet Propulsion Lab., National Aeronautics and Space Administration Pasadena, CA, pp. 451–463.

[9] Joachim Block, Annette Bäger, Jörg Behrens, Toni Delovski, L-C Hauer, Martin Schütze, Rainer Schütze, and Tom Spröwitz (2013). "A self-deploying and self-stabilizing helical antenna for small satellites". In: *Acta Astronautica* 86, pp. 88–94.

[10] Joachim Block, Marco Straubel, and Martin Wiedemann (2011). "Ultralight deployable booms for solar sails and other large gossamer structures in space". In: *Acta astronautica* 68.7-8, pp. 984–992.

[11] CR Calladine (1988). "The theory of thin shell structures 1888–1988". In: *Proceedings of the Institution of Mechanical Engineers, Part A: Power and Process Engineering* 202.3, pp. 141–149.

[12] Erik D Demaine, Martin L Demaine, Vi Hart, Gregory N Price, and Tomohiro Tachi (2011). "(Non) existence of pleated folds: how paper folds between creases". In: *Graphs and Combinatorics*. Vol. 27. 3. Springer, pp. 377–397.

[13] Erik D Demaine, Martin L Demaine, Anna Lubiw, et al. (1999). "Polyhedral sculptures with hyperbolic paraboloids". In: *Proceedings of the 2nd Annual Conference of BRIDGES: Mathematical Connections in Art, Music, and Science (BRIDGES'99)*, pp. 91–100.

[14] Xiaowei Deng and Sergio Pellegrino (2012). "Wrinkling of orthotropic viscoelastic membranes". In: *AIAA Journal* 50.3, pp. 668–681.

[15] Florence Dewalque, Cédric Schwartz, Vincent Denoël, Jean-Louis Croisier, Bénédicte Forthomme, and Olivier Brüls (2018). "Experimental and numerical investigation of the nonlinear dynamics of compliant mechanisms for deployable structures". In: *Mechanical Systems and Signal Processing* 101, pp. 1–25.

[16] JM Fernandez, M Schenk, G Prassinos, VJ Lappas, and SO Erb (2013). "Deployment mechanisms of a gossamer satellite deorbiter". In: *15th European Space Mechanisms & Tribology Symposium, Noordwijk, The Netherlands*, pp. 25–27.

[17] Juan Fernandez, Vaios Lappas, and Andrew Daton-Lovett (2012). "The completely stripped solar sail concept". In: *53rd AIAA/ASME/ASCE/AHS/ASC Structures, Structural Dynamics and Materials Conference 20th AIAA/ASME/AHS Adaptive Structures Conference 14th AIAA*. 2012-1745.

[18] Juan M Fernandez (2017). "Advanced deployable shell-based composite booms for small satellite structural applications including solar sails". In: *4th International Symposium on Solar sailing*. Vol. 1.

[19] Juan M Fernandez, Vaios J Lappas, and Andrew J Daton-Lovett (2011). "Completely stripped solar sail concept using bi-stable reeled composite booms". In: *Acta astronautica* 69.1-2, pp. 78–85.

[20] Juan M Fernandez, Andrew Viquerat, Vaios J Lappas, and Andrew J Daton-Lovett (2014). "Bistable over the whole length (BOWL) CFRP booms for solar sails". In: *Advances in solar sailing*. Springer, pp. 609–628.

[21] Jordan Firth, Benjamin Adamcik, Elliott Hannah, David Firth, and Mark Pankow (2019). "Minimal Unpowered Strain-Energy Deployment Mechanism for Rollable Spacecraft Booms". In: *AIAA Scitech 2019 Forum*. 2019-1258.

[22] A Fischer and S Pellegrino (2000). "Interaction between gravity compensation suspension system and deployable structure". In: *Journal of Spacecraft and Rockets* 37.1, pp. 93–99.

[23] E Fraterman and HA Lupker (1993). *Evaluation of belt modelling techniques*. Tech. rep. SAE Technical Paper.

[24] JoAnna Fulton and Hanspeter Schaub (2019). "Non-symmetric behavior of high strain composite tape spring hinges for folding structures". In: *AIAA Scitech 2019 Forum*. 2019-1747.

[25] Wei W Gan and Sergio Pellegrino (2006). "Numerical approach to the kinematic analysis of deployable structures forming a closed loop". In: *Proceedings of the institution of mechanical engineers, Part C: Journal of Mechanical Engineering Science* 220.7, pp. 1045–1056.

[26] Mark Garcia (2021). *New Solar Arrays to Power NASA's International Space Station Research*. URL: https://www.nasa.gov/feature/new-solar-arrays-to-power-nasa-s-international-space-station-research (visited on 04/01/2021).

[27] Mattias Gardsback and Gunnar Tibert (2009). "Deployment control of spinning space webs". In: *Journal of guidance, control, and dynamics* 32.1, pp. 40–50.

[28] Eleftherios Gdoutos, Christophe Leclerc, Fabien Royer, Michael D Kelzenberg, Emily C Warmann, Pilar Espinet-Gonzalez, Nina Vaidya, Florian Bohn, Behrooz Abiri, Mohammed R Hashemi, et al. (2018a). "A lightweight tile structure integrating photovoltaic conversion and RF power transfer for space solar power applications". In: *2018 AIAA Spacecraft Structures Conference*. 2018-2202.

[29] Eleftherios Gdoutos, Christophe Leclerc, Fabien Royer, Michael D Kelzenberg, Emily C Warmann, Pilar Espinet-Gonzalez, Nina Vaidya, Florian Bohn, Behrooz Abiri, Mohammed R Hashemi, et al. (2018b). "A lightweight tile structure integrating photovoltaic conversion and RF power transfer for space solar power applications". In: *AIAA SciTech Forum*. 2018-2202.

[30] Gene H Golub and Charles F Van Loan (2013). *Matrix computations*. Vol. 3. JHU press.

[31] G Greschik and MM Mikulas (2002). "Design study of a square solar sail architecture". In: *Journal of Spacecraft and Rockets* 39.5, pp. 653–661.

[32] Gyula Greschik (2018). "Roll Stabilization for Wrapped Array Prototype". In: *2018 AIAA Spacecraft Structures Conference*. 2018-2207.

[33] Gyula Greschik and W Keith Belvin (2007). "High-fidelity gravity offloading system for free-free vibration testing". In: *Journal of Spacecraft and Rockets* 44.1, pp. 132–142.

[34] Olyvia Han, David Kienholz, Paul Janzen, and Scott Kidney (2010). "Gravity-Offloading System for Large-Displacement Ground Testing of Spacecraft Mechanisms". In: *Proceedings of the 40th Aerospace Mechanisms Symposium*.

[35] Mohammed Reza M Hashemi, Austin C Fikes, Matan Gal-Katziri, Behrooz Abiri, Florian Bohn, Amirreza Safaripour, Michael D Kelzenberg, Emily L Warmann, Pilar Espinet, Nina Vaidya, Eletherios E. Gdoutos, Christophe Leclerc, Fabien Royer, Sergio Pellegrino, Harry A. Atwater, and Ali Hajimiri (2019). "A flexible phased array system with low areal mass density". In: *Nature Electronics* 2.5, pp. 195–205.

[36] Paul E Hausgen, Bernie Carpenter, Neeraj Gupta, and Dana Turse (2016). "TacSat 2 experimental solar array on-orbit data and analysis". In: *2016 IEEE 43rd Photovoltaic Specialists Conference (PVSC)*. IEEE, pp. 2565–2570.

[37] Mark N Helfrick, Christopher Niezrecki, Peter Avitabile, and Timothy Schmidt (2011). "3D digital image correlation methods for full-field vibration measurement". In: *Mechanical systems and signal processing* 25.3, pp. 917–927.

[38] Bao Hoang, Steve White, Brian Spence, and Steven Kiefer (2016). "Commercialization of Deployable Space Systems' roll-out solar array (ROSA) technology for Space Systems Loral (SSL) solar arrays". In: *2016 IEEE Aerospace Conference*. IEEE, pp. 1–12.

[39] Adam Hoskin, Andrew Viquerat, and Guglielmo S Aglietti (2017). "Tip force during blossoming of coiled deployable booms". In: *International Journal of Solids and Structures* 118, pp. 58–69.

[40] Luc Houpert (2002). "Ball bearing and tapered roller bearing torque: analytical, numerical and experimental results". In: *Tribology Transactions* 45.3, pp. 345–353.

[41] Kevin Hughes, Omkar Gulavani, Tom De Vuyst, and Rade Vignjevic (2014). "Explicit dynamic formulation to demonstrate compliance against quasi-static aircraft seat certification loads (CS25. 561)–Part II: Influence of body blocks". In: *Proceedings of the Institution of Mechanical Engineers, Part G: Journal of Aerospace Engineering* 228.10, pp. 1890–1903.

[42] Kosuke Ikeya, Hiraku Sakamoto, Hiroki Nakanishi, Hiroshi Furuya, Takashi Tomura, Ryoga Ide, Ryo Iijima, Yohei Iwasaki, Keigo Ohno, Keisuke Omoto, et al. (2020). "Significance of 3U CubeSat OrigamiSat-1 for space demonstration of multifunctional deployable membrane". In: *Acta Astronautica* 173, pp. 363–377.

[43] Sungeun Jeon and Thomas Murphey (2011). "Design and analysis of a meter-class CubeSat boom with a motor-less deployment by bi-stable tape springs". In: *52nd AIAA/ASME/ASCE/AHS/ASC Structures, Structural Dynamics and Materials Conference 19th AIAA/ASME/AHS Adaptive Structures Conference 13t*. 2011-1731.

[44] Ju Won Jeong, Young Ik Yoo, Jung Ju Lee, Jae Hyuk Lim, and Kyung Won Kim (2012). "Development of a tape spring hinge with a SMA latch for a satellite solar array deployment using the independence axiom". In: *Ieri Procedia* 1, pp. 225–231.

[45] Les Johnson, Mark Whorton, Andy Heaton, Robin Pinson, Greg Laue, and Charles Adams (2011). "NanoSail-D: A solar sail demonstration mission". In: *Acta astronautica* 68.5-6, pp. 571–575.

[46] Ian T Jolliffe (1986). "Principal components in regression analysis". In: *Principal component analysis*. Springer, pp. 129–155.

[47] P Alan Jones and Brian R Spence (2011). “Spacecraft solar array technology trends”. In: *IEEE Aerospace and Electronic Systems Magazine* 26.8, pp. 17–28.

[48] Joni Jorgensen, Ehlias Louis, Jason Hinkle, Mark Silver, Bill Zuckermandel, and Scott Enger (2005). “Dynamics of an elastically deployable solar array: ground test model validation”. In: *46th AIAA/ASME/ASCE/AHS/ASC Structures, Structural Dynamics and Materials Conference*. 2005-1942.

[49] Feng Ju and Yoo Sang Choo (2005). “Dynamic analysis of tower cranes”. In: *Journal of Engineering Mechanics* 131.1, pp. 88–96.

[50] Michael D Kelzenberg, Pilar Espinet-Gonzalez, Nina Vaidya, Emily C Warmann, Ali Naqavi, Samuel P Loke, Philipp Saive, Tatiana A Roy, Tatiana G Vinogradova, Christophe Leclerc, et al. (2018). “Ultralight energy converter tile for the space solar power initiative”. In: *2018 IEEE 7th World Conference on Photovoltaic Energy Conversion (WCPEC)(A Joint Conference of 45th IEEE PVSC, 28th PVSEC & 34th EU PVSEC)*. IEEE, pp. 3357–3359.

[51] Andrew Klesh and Joel Krajewski (2015). “MarCO: CubeSats to Mars in 2016”. In: *Proceedings of the 29th Annual AIAA/USU Conference on Small Satellites*.

[52] VA Koshelev and VM Melnikov (1998). *Large space structures formed by centrifugal forces*. CRC Press.

[53] S Kukathasan and Sergio Pellegrino (2002). “Vibration of prestressed membrane structures in air”. In: *43rd AIAA/ASME/ASCE/AHS/ASC Structures, Structural Dynamics, and Materials Conference*. 2002-1368.

[54] P Kumar and S Pellegrino (2000). “Computation of kinematic paths and bifurcation points”. In: *International Journal of Solids and Structures* 37.46-47, pp. 7003–7027.

[55] Moon K Kwak, Seok Heo, and Hong B Kim (2008). “Dynamics of satellite with deployable rigid solar arrays”. In: *Multibody System Dynamics* 20.3, pp. 271–286.

[56] Christophe Leclerc, Antonio Pedivellano, and Sergio Pellegrino (2018). “Stress concentration and material failure during coiling of ultra-thin TRAC booms”. In: *2018 AIAA Spacecraft Structures Conference*. 2018-0690.

[57] Christophe Leclerc and Sergio Pellegrino (2020). “Nonlinear elastic buckling of ultra-thin coilable booms”. In: *International Journal of Solids and Structures* 203, pp. 46–56.

[58] M Leipold, CE Garner, R Freeland, A Hermann, M Noca, G Pagel, W Seboldt, G Sprague, and W Unckenbold (1999). “Odissee—a proposal for demonstration of a solar sail in earth orbit”. In: *Acta Astronautica* 45.4-9, pp. 557–566.

[59] Jack Lekan (1989). “Microgravity research in NASA ground-based facilities”. In: *27th Aerospace Sciences Meeting*. 1989-236.

[60] David Lichodziejewski, John West, Richard Reinert, Kara Slade, and Keith Belvin (2004). "Development and ground testing of a compactly stowed inflatably deployed solar sail". In: *45th AIAA/ASME/ASCE/AHS/ASC Structures, Structural Dynamics & Materials Conference*. 2004-1507.

[61] WF Lindsey (1938). "Drag of cylinders of simple shapes". In: *NACA Technical Report* 619, pp. 169–176.

[62] Tiffany Russell Lockett, Alexander Few, and Richard Wilson (2017). "Near Earth Asteroid Solar Sail Engineering Development Unit Test Program". In: *The Fourth International Symposium on Solar Sailing*, pp. 1–5.

[63] HMYC Mallikarachchi and S Pellegrino (2014). "Deployment dynamics of ultrathin composite booms with tape-spring hinges". In: *Journal of Spacecraft and Rockets* 51.2, pp. 604–613.

[64] Eric Harold Mansfield (1973). "Large-deflexion torsion and flexure of initially curved strips". In: *Proceedings of the Royal Society of London. A. Mathematical and Physical Sciences* 334.1598, pp. 279–298.

[65] David H Manzella and Kurt Hack (2014). "High-power solar electric propulsion for future nasa missions". In: *50th AIAA/ASME/SAE/ASEE Joint Propulsion Conference*. 2014-3718.

[66] Huina Mao, Pier Luigi Ganga, Michele Ghiozzi, Nickolay Ivchenko, and Gunnar Tibert (2017). "Deployment of bistable self-deployable tape spring booms using a gravity offloading system". In: *Journal of Aerospace Engineering* 30.4.

[67] Geoffrey W Marks, Michael T Reilly, and Richard L Huff (2002). "The lightweight deployable antenna for the MARSIS experiment on the Mars express spacecraft". In: *36th Aerospace Mechanisms Symp*, pp. 183–196.

[68] Ricardo A Maronna, R Douglas Martin, Victor J Yohai, et al. (2019). *Robust statistics: theory and methods (with R)*. John Wiley & Sons.

[69] Sebastian Meyer, Martin Hillebrandt, Marco Straubel, and Christian Huhne (2014). "Design of the de-orbit sail boom deployment unit". In: *13th European Conference on Spacecraft Structures, Materials & Environmental Testing*. Vol. 727, p. 179.

[70] Martin M Mikulas, Richard S Pappa, Jay Warren, and Geoff Rose (2015). "Telescoping solar array concept for achieving high packaging efficiency". In: *2nd AIAA Spacecraft Structures Conference*. 2015-1398.

[71] Richard K Miller and John M Hedgepeth (1982). "An algorithm for finite element analysis of partly wrinkled membranes". In: *AIAA Journal* 20.12, pp. 1761–1763.

[72] Richard K Miller, John M Hedgepeth, Victor I Weingarten, Prasanta Das, and Shahrzad Kahyai (1985). "Finite element analysis of partly wrinkled membranes". In: *Advances and Trends in Structures and Dynamics*. Elsevier, pp. 631–639.

[73] Mehran Mobrem and Douglas Adams (2006). "Analysis of the lenticular jointed MARSIS antenna deployment". In: *47th AIAA/ASME/ASCE/AHS/ASC Structures, Structural Dynamics, and Materials Conference 14th AIAA/ASME/AHS Adaptive Structures Conference 7th*. 2006-1683.

[74] Osamu Mori, Hirotaka Sawada, Ryu Funase, Mutsuko Morimoto, Tatsuya Endo, Takayuki Yamamoto, Yuichi Tsuda, Yasuhiro Kawakatsu, Jun'ichiro Kawaguchi, Yasuyuki Miyazaki, et al. (2010). "First solar power sail demonstration by IKAROS". In: *Transactions of the Japan Society for Aeronautical and Space Sciences, Aerospace Technology Japan* 8.ists27, To_4_25–To_4_31.

[75] Thomas W Murphey and Jeremy Banik (2011). *Triangular rollable and collapsible boom*. US Patent 7,895,795.

[76] Thomas W Murphey, Dana Turse, and Larry Adams (2017). "TRAC boom structural mechanics". In: *4th AIAA Spacecraft Structures Conference*. 2017-0171.

[77] David M Murphy, Michael I Eskenazi, Michael E McEachen, and James W Spink (2016). "UltraFlex and MegaFlex-advancements in highly scalable solar power". In: *3rd AIAA Spacecraft Structures Conference*. 2016-1947.

[78] Gina Olson, Thomas Murphey, and Grant Thomas (2011). "Free deployment dynamics of a Z-folded solar array". In: *52nd AIAA/ASME/ASCE/AHS/ASC Structures, Structural Dynamics and Materials Conference 19th AIAA/ASME/AHS Adaptive Structures Conference*. 2011-1730.

[79] Antonio Pedivellano and Sergio Pellegrino (2019). "Stability Analysis of Coiled Tape Springs". In: *AIAA Scitech 2019 Forum*. 2019-1523.

[80] Sergio Pellegrino (1993). "Structural computations with the singular value decomposition of the equilibrium matrix". In: *International Journal of Solids and Structures* 30.21, pp. 3025–3035.

[81] Sergio Pellegrino and Julian FV Vincent (2001). "How to fold a membrane". In: *Deployable structures*. Springer, pp. 59–75.

[82] F.P.J. Rimrott (1970). "Nachtrag zum Tagungsheft der GAMM-Tagung 1969. Querschnittsverformung bei Torsion offener Profile". In: *ZAMM-Journal of Applied Mathematics and Mechanics/Zeitschrift für Angewandte Mathematik und Mechanik* 50.12, pp. 775–778.

[83] Francisco Roybal, Jeremy Banik, and Thomas Murphey (2007). "Development of an elastically deployable boom for tensioned planar structures". In: *48th AIAA/ASME/ASCE/AHS/ASC Structures, Structural Dynamics, and Materials Conference*. 2007-1838.

[84] Fabien Royer, Yang Li, Alan Truong, Charles Sommer, and Sergio Pellegrino (In preparation). "Pure Bending Machine for Testing Non-Linear Structures". In:

[85] Fabien Royer and Sergio Pellegrino (2018). "Ultralight ladder-type coilable space structures". In: *AIAA SciTech Forum*. 2018-1200.

[86] Fabien Royer and Sergio Pellegrino (2020). “Buckling of Ultralight Ladder-type Coilable Space Structures”. In: *AIAA Scitech 2020 Forum*. 2020-1437.

[87] Maria Sakovsky and Sergio Pellegrino (2019). “Closed cross-section dual-matrix composite hinge for deployable structures”. In: *Composite Structures* 208, pp. 784–795.

[88] Jonathan F Sauder, Manan Arya, Nacer Chahat, Ellen Thiel, Sean Dunphy, Mengjan Shi, Gregory Agnes, and Tom Cwik (2019). “Deployment mechanisms for high packing efficiency one-meter reflectarray antenna (OMERA)”. In: *AIAA Scitech 2019 Forum*. 2019-0755.

[89] Patric Seefeldt, Peter Spietz, Tom Sproewitz, Jan Thimo Grundmann, Martin Hillebrandt, Catherin Hobbie, Michael Ruffer, Marco Straubel, Norbert Tóth, and Martin Zander (2017). “Gossamer-1: Mission concept and technology for a controlled deployment of gossamer spacecraft”. In: *Advances in Space Research* 59.1, pp. 434–456.

[90] KA Seffen and S Pellegrino (1999). “Deployment dynamics of tape springs”. In: *Proceedings of the Royal Society of London. Series A: Mathematical, Physical and Engineering Sciences* 455.1983, pp. 1003–1048.

[91] Keith A Seffen (2012). “Compliant shell mechanisms”. In: *Philosophical Transactions of the Royal Society A: Mathematical, Physical and Engineering Sciences* 370.1965, pp. 2010–2026.

[92] JL Sewell, Robert Miserentino, and Richard S Pappa (1983). “Vibration studies of a lightweight three-sided membrane suitable for space application”. In: *NASA Technical Paper 2095*.

[93] Brian R Spence, Steve White, Matt LaPointe, Steve Kiefer, Peter LaCorte, Jeremy Banik, David Chapman, and John Merrill (2018). “International space station (ISS) roll-out solar array (ROSA) spaceflight experiment mission and results”. In: *2018 IEEE 7th World Conference on Photovoltaic Energy Conversion (WCPEC)*. IEEE, pp. 3522–3529.

[94] Ted Steinberg (2008). “Reduced gravity testing and research capabilities at Queensland University of Technology’s New 2.0 Second Drop Tower”. In: *Advanced Materials Research*. Vol. 32. Trans Tech Publ, pp. 21–24.

[95] Olive R Stohlman, Juan M Fernandez, Vaios Lappas, Martin Hillebrandt, Christian Hühne, and Marco Straubel (2013). “Testing of the Deorbitsail drag sail subsystem”. In: *54th AIAA/ASME/ASCE/AHS/ASC Structures, Structural Dynamics, and Materials Conference*. 2013-1807.

[96] Olive R Stohlman and Vaios Lappas (2013). “Deorbitsail: a deployable sail for de-orbiting”. In: *54th AIAA/ASME/ASCE/AHS/ASC Structures, Structural Dynamics, and Materials Conference*. 2013-1806.

[97] Olive R Stohlman and Vaios Lappas (2014). “Development of the Deorbitsail flight model”. In: *Spacecraft Structures Conference*. 2014-1509.

[98] Marco Straubel, Patric Seefeldt, Peter Spietz, and Christian Huehne (2015). "The design and test of the Gossamer-1 boom deployment mechanisms engineering model". In: *2nd AIAA Spacecraft Structures Conference*. 2015-1837.

[99] Marco Straubel, Michael Sinapius, and Stéphane Langlois (2009). "On-Ground Rigidized, Deployable Masts for Large Gossamer Space Structures". In:

[100] Marco Straubel, Martin E Zander, and Christian Hühne (2014). "Design and sizing of the GOSSAMER boom deployment concept". In: *Advances in solar sailing*. Springer, pp. 593–608.

[101] Rao Surampudi, Tom Hamilton, Donald Rapp, Paul Stella, Nick Mardesich, Jack Mondt, Bill Nesmith, Robert L. Bunker, James Cutts, Sheila G. Bailey, Henry B. Curtis, Mike Piszczor, Ed Gaddy, Dean Marvin, and Larry Kazmerzki (2002). "Solar cell and array technology for future space missions". In: *Technical Report D-24454, National Aeronautics and Space Administration*.

[102] R Sygulski (1994). "Dynamic analysis of open membrane structures interacting with air". In: *International Journal for Numerical Methods in Engineering* 37.11, pp. 1807–1823.

[103] Daniel A Türk and Sergio Pellegrino (2019). "Parametric Design of Conforming Joints for Thin-Shell Coilable Structures". In: *AIAA SciTech Forum*. 2019-1259.

[104] John Joseph Uicker, Gordon R Pennock, Joseph Edward Shigley, and J Michael Mccarthy (2003). *Theory of machines and mechanisms*. Vol. 3. Oxford University Press New York.

[105] Lee Wilson, Eleftherios E Gdoutos, and Sergio Pellegrino (2020). "Tension-Stabilized Coiling of Isotropic Tape Springs". In: *International Journal of Solids and Structures* 188, pp. 103–117.

[106] Wesley Wong and Sergio Pellegrino (2006). "Wrinkled membranes III: numerical simulations". In: *Journal of Mechanics of Materials and Structures* 1.1, pp. 63–95.

[107] Shih-Chin Wu and Siamak Ghofranian (2005). "Anomaly simulation and resolution of International Space Station solar array deployment". In: *Modeling, Simulation, and Verification of Space-based Systems II*. Vol. 5799. International Society for Optics and Photonics, pp. 38–47.

[108] Walter Wuest (1954). "Einige anwendungen der theorie der zylinderschale". In: *ZAMM-Journal of Applied Mathematics and Mechanics/Zeitschrift für Angewandte Mathematik und Mechanik* 34.12, pp. 444–454.

[109] Dong Yang, Ruixia Yang, Shashank Priya, and Shengzhong Liu (2019). "Recent advances in flexible perovskite solar cells: fabrication and applications". In: *Angewandte Chemie International Edition* 58.14, pp. 4466–4483.

[110] T. Yasaka and S. Oda (1988). “Air effects on the structure vibration and the considerations to large spacecraft ground testing”. In: *39th Congress of the International Astronautical Federation*.

[111] Zhihua Zhao, Kangjia Fu, Meng Li, Jinyou Li, and Yong Xiao (2020). “Gravity compensation system of mesh antennas for in-orbit prediction of deployment dynamics”. In: *Acta Astronautica* 167, pp. 1–13.